Journal of Molecular Liquids 341 (2021) 116918

Contents lists available at ScienceDirect

Journal of Molecular Liquids

journal homepage: www.elsevier.com/locate/molliq

Phase equilibria and interfacial properties of selected methane + n-alkane binary mixtures

Andrés Mejía [a,*], Marcela Cartes [a], Gustavo Chaparro [a], Esther Feria [b], Felipe J. Blas [b], José Manuel Míguez [b], Jesús Algaba [c], Erich A. Müller [c]

[a] Departamento de Ingeniería Química, Universidad de Concepción, Concepción, Chile
[b] Laboratorio de Simulación Molecular y Química Computacional, CIQSO-Centro de Investigación en Química Sostenible and Departamento de Ciencias Integradas, Universidad de Huelva, 21007 Huelva, Spain
[c] Department of Chemical Engineering, Imperial College London, South Kensington Campus, London SW7 2AZ, UK

ARTICLE INFO

Article history:
Received 7 April 2021
Revised 26 June 2021
Accepted 1 July 2021
Available online 5 July 2021

Keywords:
Methane + n-alkane binary mixtures
Tensiometry
Interfacial properties

ABSTRACT

Experimental determination, theoretical modeling, and molecular simulation have been combined to describe the bulk phase equilibria (*i.e.*, pressure, liquid, and vapor saturated mass densities) and interfacial properties (*i.e.*, interfacial concentration, adsorption, and interfacial tension) for methane + n-decane, n-dodecane, n-tetradecane and n-hexadecane binary mixtures at 344.15 K and in a pressure range between 0.1 and 30 MPa. Experimental determinations are carried out using a combined apparatus that includes a high-pressure vibrating tube densimeter and a high-pressure pendant drop tensiometer. The theoretical approach is based on the van der Waals gradient theory coupled to the Statistical Associating Fluid Theory of Variable Range employing a Mie potential (SAFT-VR-Mie) equation of state, where the fluids are described as Coarse Grained (CG) atoms. Molecular dynamics simulation for the same systems based on the CG Mie potential are reported. The three approaches are able to indepen independently predict phase equilibrium and interfacial properties, showing a very good agreement amongst themselves. For the systems and conditions studied here, the vapor mass density increases; the liquid mass density and interfacial tensions decrease as the pressure increases, and with a fixed temperature and pressure, the liquid mass density and interfacial tensions increase as the n-alkane molecular chain length increases. It is observed that methane is adsorbed along the interfacial region, whereas the n-alkanes (n-decane, n-dodecane, n-tetradecane, n-hexadecane) do not exhibit surface activity. The relative Gibbs adsorption of methane increases significantly with pressure until it reaches a maximum denoting the adsorption saturation limit. It is also observed that the adsorption of methane only slightly increases with the chain length of the n-alkane.

1. Introduction

The phase and interfacial behavior of n-alkane mixtures have received continuous attention in applied thermodynamics. Their description and accurate prediction are key in the petroleum and oil refining industries, gas condensate recovery, liquefaction of natural gas, oil transportation, and recently have become relevant within the context of environmental control.[1] Particularly interesting are the asymmetric mixtures of methane with alkanes of high molecular weight that display a fascinating but complex behavior. They exhibit large departures from ideality, mainly caused by the differences in the molecular size of the components of the mixture, and also show several types of phase and interfacial behavior. Specifically, methane + n-alkane up to n-pentane mixtures are completely miscible in the liquid phase (with only vapor–liquid equilibria, VLE), and are described as Type I in the van Konynenburg and Scott classification.[2] From methane + n-hexane onwards, the phase behavior is complemented by the appearance of three-fluid phase line (*i.e.*, vapor-liquid–liquid equilibria, VLLE) near to the critical point of methane. This VLLE causes that the VLE critical line be separated into two branches: one of them initiates at the critical point of methane ascending up to the upper critical end point (UCEP) of the VLLE, and the second one from the lower critical end point (LCEP) of the VLLE with a maximum in the pressure up to the critical point of n-hexane. For the case of methane + n-heptane mixture, the VLLE is interrupted by another three-phase line: solid n-heptane + L+V (SLVE).

* Corresponding author.
E-mail address: amejia@udec.cl (A. Mejía).

https://doi.org/10.1016/j.molliq.2021.116918
0167-7322/

This interception generates a quadruple point (solid n-heptane + L_1+L_2+V, SLLVE). For higher n-alkanes, the VLLE disappears, and the mixtures display two CEPs. At each CEP, the solid phase is in equilibrium with a critical VL phase. Therefore, methane + n-alkane mixtures (n-octane or higher) will exhibit several types of equilibria, namely solid–liquid (SLE), solid–vapor (SVE), SLVE, and vapor–liquid (VLE), the latter equilibrium also showing an interesting behavior where retrograde condensation is observed.

An initial and general discussion of these phase equilibria types was given by Davenport and Rowlinson,[3] who described the general trends of selected alkanes with liquid methane. This general description was complemented by Rijkers,[4] who described from an experimental and theoretical perspective the phase equilibrium of methane + n-decane, or n-dodecane, or n-hexadecane. In the case of interfacial behavior, the interfacial tension of the methane + n-alkane mixtures up to n-decane has been measured in a broad range of temperature and pressure under VLE conditions (see Pereira et al., [5] and references therein). Other interfacial properties, such as concentration profile along the interfacial region and the Gibbs adsorption, have been calculated by using cubic equation of state (EoS) coupled to the van der Waals square gradient theory,[6,5,7,8] linear gradient theory,[5] and density functional theory (DFT) with Statistical Associating Fluid Theory (SAFT) EoS.[9] Recently, classical Molecular Dynamics (MD) simulations based on the united atoms description have also been applied to predict the interfacial behavior of these systems.[7,8] Surprisingly, simultaneous description of available experimental data, theoretical predictions and molecular simulations only cover the methane + n-alkane mixtures up to n-decane, and to the best of our knowledge, only Choudhary et al. [8] have recently explored some higher n-alkane (*i.e.*, n-dodecane and n-nonadecane).

The aim of this work is to describe simultaneously the bulk density phase equilibria and the interfacial properties for the case of methane + n-alkane mixtures [CH_4(1) + C_nH_{2n+2}(2), with n = 10 (n-decane), 12 (n-dodecane), 14 (n-tetradecane), and 16 (n-hexadecane)] at 344.15 K and the thermodynamic conditions where the mixtures only display VLE. The selected temperature and pressure range have been selected as they represent commonly encountered conditions observed in gas-oil systems related to petroleum reservoirs.

The experimental phase equilibrium on *PTx* coordinates of these systems have been measured by several authors in a broad range of temperatures and pressures. [10] Of the particular relevance is the series of manuscripts from the Delft group,[11,4,12–15] who provided not only new experimental data but also an EoS based modeling of the phase equilibrium. For the case of bulk fluid densities and interfacial tensions, the spectrum of experimental information is reduced to the methane + n-decane binary mixture.[16,17,5] Adding to the experimental determinations of bulk fluid densities and interfacial tension, theoretical approaches,[6,9,5] and molecular simulations cover the methane + n-decane mixture, [7] and recently the methane + n-dodecane mixture. [8].

The research presented here combines experiments, theory, and molecular simulation. Specifically, the experiments are based on an experimental setup that includes a high pressure pendant drop tensiometer with a high pressure densimeter and covers the pressure range from 0.1 to 20 MPa. The theoretical approach is based on the van der Waals square gradient theory[18–20] coupled to the Statistical Associating Fluid Theory of Variable Range employing a Mie potential (SAFT-VR-Mie).[21] Computer simulations are carried out by using molecular dynamics (MD) employing the force field underlying the SAFT-VR-Mie approach.[22]. A distinctive aspect of this work is that in both the theoretical modeling (SAFT-VR-Mie coupled to SGT) and in the molecular dynamics simulations, the same set of CG Mie force field parameters are used. The advantage of this approach is that the results from the theory and the simulations can be directly compared. The same strategy has been previously used by some of us for describing CO_2 + hydrocarbon mixtures, [23,24] N_2 + n-alkanes, [25] homonuclear ring fluid mixtures,[26] water + hexane mixture, [27] and Lennard-Jones mixtures,[28,29] as well as by other authors, who have been recently employing the same strategy to relate the interfacial behavior to bulk phase behavior of Lennard-Jones mixtures, [30,31] and to quantify the effect of the polar interactions on bulk and interfacial properties.[32].

2. Experimental Section

2.1. Pure fluids

Methane was purchased from AirLiquid with a certified purity greater than 99.995.%, whereas n-alkanes (*i.e.*, n-decane, n-dodecane, n-tetradecane and n-hexadecane) were purchased from Merck and used as received. Table 1 summarizes some purity indicators of the pure n-alkanes such as the purity reported by the manufactures and measured by gas chromatography (GC), the mass densities (ρ), and the interfacial tensions (γ) of the pure fluids at 344.15 K and 101.3 kPa. This table also includes the reference experimental values reported on the NIST-TDE database.[33].

2.2. Density measurements

The mass density of the pure fluids is measured at 344.15 K and 101.3 kPa using a DMA 5000 M densimeter (Anton Paar, Austria). For the case of mixtures (CH_4 + n-alkane) at 344.15 K and pressures over 101.3 kPa, the liquid and vapor densities are measured by using a DMA HP densimeter (Anton Paar, Austria), which is connected to the tensiometer chamber. In both cases (pure fluids and fluid mixtures), the mass density determination is based on measuring the period of oscillation of a vibrating U-shaped tube filled with the fluid sample.[34] These devices are calibrated by using two reference fluids. For the case of DMA 5000 M densimeter, ultrapure water and atmospheric air were used at 298.15 K and 101.3 kPa. For the case of DMA HP densimeter, N_2 and n-decane were used at 344.15 K and over the pressure range from 0.1 MPa to 30 MPa.

During the operation, the temperature of the apparatus is maintained constant to within ± 0.01 K. Pressure is measured by means a Swagelok type S pressure transducer connected to the densimeter and maintained constant to within ± 0.001 kPa by using a high-pressure syringe pump (Teledyne Isco Pump. Model 100DM, USA). The mass density is measured with an instrument standard uncertainty of 0.4 kg/m^3, and a combined expanded uncertainty (considering a 0.95 level of confidence, k = 2) of U(r) = 1.1 kg/m^3.

The experimental procedure to measure the fluid densities is as follows. The tensiometer cell is initially heated to 344.15 K and slightly pressurized with CH_4. The n-alkane (n-decane, n-dodecane, n-tetradecane, or n-hexadecane) is pumped through a stainless-steel tube to fill approximately 30% of its volume by visual observation, and then the pressure is increased to the desired experimental value. In the chamber, the gas will be saturated with the n-alkane, and some gas diffuses into the n-alkane. Once the equilibrium is reached, the saturated CH_4 is transported to the high-pressure densimeter through a heated stainless steel tube to measure the mass density of CH_4 saturated with n-alkane (ρ_V). The density measurements are repeated 10 times for each condition and averaged accordingly. The same procedure is carried out to measure the mass density of the n-alkane saturated with CH_4 (ρ_L) but in this case, the chamber is filled up to approximately 85% of its volume by visual observation.

Table 1
Gas chromatography (GC) purities (mass fraction, w), liquid mass densities (ρ) and interfacial tensions (γ) of pure n-alkanes at 344.15 K and 101.3 kPa measured in this work (Exp.)* and taken from the average of the data reported on the NIST-TDE database.[33] (Ref.)

Substance	source	w/ supplier	Purification	w/ GC	ρ (kg/m^3)		γ (mN/m)	
					Exp.	Ref.	Exp.	Ref.
n-decane	Merck	> 0.99	none	0.999	691.21	690.50	19.01	19.14
n-dodecane	Merck	> 0.99	none	0.999	712.10	712.30	20.72	20.79
n-tetradecane	Merck	> 0.99	none	0.999	727.10	727.40	22.07	22.08
n-hexadecane	Merck	> 0.99	none	0.999	738.26	737.96	23.02	23.23

*The standard uncertainties (0.68 level of confidence) are: $u(T) = 0.1$ K. Instrument standard uncertainty are $\rho = 0.4$ kg/m^3 and $\gamma = 0.05$ mN/m. The combined expanded uncertainties (considering a 0.95 level of confidence, $k = 2$) are $U(\rho) = 1.1$ kg/m^3 and $U(\gamma) = 0.1$ mN/m.

2.3. Tensiometry measurements

The interfacial tension between a liquid mixture drop surrounded by a gas mixture at 344.15 K and over the pressure range from 0.1 to 20.0 MPa is measured using an IFT-10 high-pressure pendant drop tensiometer (Temco Inc., USA). This device is equipped with a cool light beam source and a video camera, which is connected to a personal computer through a frame grabber card. In order to avoid external vibrations, both the tensiometer and the camera are mounted on a vibration-free table. Specific technical details of this tensiometer device and its parts have been extensively described in previous works.[35,23,36–40].

The experimental procedure is as follows. The tensiometer cell is initially heated to 344.15 K and slightly pressurized with CH_4. The n-alkane (n-decane, n-dodecane, n-tetradecane, and n-hexadecane) is pumped through a stainless-steel tube to fill one-third of the chamber in order to saturate the gas that fills the cell and allow some gas to diffuse into the n-alkane. The tensiometer cell is pressurized to the desired experimental pressure, and once the equilibrium is reached, a liquid drop of the n-alkane is generated at the tip of a stainless steel needle (1.4 mm i.d. and 2.45 mm o.d.) into the tensiometer chamber. Once the drop is formed, it is necessary to wait, approximately 10–15 min, to saturat the liquid drop, and for the cell to reach a stable condition of pressure and temperature. After this equilibration step, the drop dimensions are recorded (for at least during 2 h) in order to check the stability of its geometry (*i.e.*, shape and volume of the drop). Once the shape and volume of the drop are deemed constant, the equatorial diameter of the drop, d_e (the largest one), and the horizontal diameter of the drop, d_s, which is located at a distance d_e from the apex of the drop, are recorded.

Based on the experimental measurements of ρ_L, ρ_V, d_e, d_s, the interfacial tension, γ, is calculated from the Laplace equation:

$$\gamma = (\rho_L - \rho_V) g\, d_e^2\, \Im(d_e, d_s) \tag{1}$$

where g is the local gravitational constant ($g = 9.81\,\mathrm{m/s^2}$), and $\Im(d_e, d_s)$ represents a function related to the silhouette of the drop, whose values are determined from numerical tables.[41] In this device, the pressure and the temperature are maintained constant within ± 0.001 kPa, and ± 0.1 K, respectively. Additional details relating to the pendant drop technique can be found in references. [42,43]

The numerical results of γ from Eq. (1) are affected by the value of pressure, density difference and the experimental reproducibility of γ. In order to quantify these effects on the reported value of γ, the uncertainties of γ are calculated from the expanded or combined relative uncertainty of $\gamma, u_c(\gamma)$:[44]

$$u_c^2(\gamma) = \left[\frac{1}{\gamma}\left(\frac{\partial \gamma}{\partial P}\right)_T \delta P\right]^2 + \left[\frac{\delta \Delta\rho}{\Delta\rho}\right]^2 + \left[\frac{\sigma(\gamma)}{\gamma}\right]^2 \tag{2}$$

In the latter expression, δP and $\delta \triangle \rho$ are the corresponding standard uncertainties in pressure and density, respectively. $\sigma(\gamma)$ is the standard deviation of γ, which together with the maximum experimental value of partial derivatives of γ in P permits to estimate the value of u_c. For the binary mixtures investigated here, the average of u_c was found to be 0.78%. Therefore, the expanded relative uncertainty of γ at 95% confidence was 1.5% or equivalently to 0.1 mN/m.

Finally, the measured data of density and interfacial tension can be also used to approximately estimate the magnitude of the Gibbs adsorption isotherm of CH_4 (1) relative to the n-alkane (2), Γ_{12}:[45]

$$\Gamma_{12} \approx -\frac{\rho_1}{M_{w_1}}\left(\frac{\partial \gamma}{\partial P}\right)_T \tag{3}$$

Here M_{w_1} and ρ_1 are the molecular weight and molar density of the pure CH_4, respectively. ρ_1 is evaluated at T and P, whereas the slope $(\partial\gamma/\partial P)_T$ is obtained from the experimental $\gamma - P$.

3. Theory

Theoretical predictions of bulk phase equilibria (*i.e.*, temperature, pressure, mole fraction and bulk liquid and vapor densities) and interfacial properties (*i.e.*, interfacial concentration profiles, surface activity, relative Gibbs adsorption and interfacial tension) are obtained by considering that the pure fluids and the binary fluid mixtures can be described as super united atoms, a coarse grained (CG) representation of molecules formed of segments interacting through the Mie potential, [46]

$$\phi^{Mie}(r_{ij}) = C\varepsilon\left[\left(\frac{\sigma}{r_{ij}}\right)^{\lambda} - \left(\frac{\sigma}{r_{ij}}\right)^{6}\right] \tag{4}$$

where λ is the repulsive parameter which dictates the range and softness of the intermolecular potential. r_{ij} is the center-to-center distance of the interacting segments, ε is the energy scale corresponding to the potential well depth, σ is the length scale, corresponding loosely with an effective segment diameter, and C is a constant defined as:

$$C = \frac{\lambda}{\lambda - 6}\left(\frac{\lambda}{6}\right)^{\frac{6}{\lambda - 6}} \tag{5}$$

Within this CG approach, CH_4 is represented by one single sphere and n-alkanes are modeled as a chain of tangent spheres where bond distances are kept constant at a value of σ and no further intramolecular interactions are employed. Table 2 summarizes the numerical values of the Mie potential for the pure fluids used here. These values were obtained by invoking the corresponding state principle described in previous works.[47,48]

In this work, the bulk phase or homogeneous region is described by the Statistical Associating Fluid Theory of Variable Range employing for molecules formed of segments interacting through the Mie potential (SAFT-VR-Mie). In this version of SAFT, the Helmholtz energy density for a non-associating chain fluid, a_0, is given by:[21]

Table 2
Molecular parameters of the Mie potential for the pure fluids

Substance	m_s	ε/k_B (K)	σ (Å)	λ
CH_4	1	170.754	3.752	16.391
$C_{10}H_{22}$	3	415.190	4.584	20.920
$C_{12}H_{26}$	4	378.560	4.351	18.410
$C_{14}H_{30}$	5	363.060	4.183	17.660
$C_{16}H_{34}$	5	418.130	4.432	21.200

$$a_0 = \left(a^{ig} + a^{mono} + a^{chain}\right)\rho\frac{N_{av}}{\beta} \tag{6}$$

where ρ is the molar density of the mixture, N_{av} is the Avogadro constant, $\beta = 1/k_BT, T$ is the absolute temperature, and k_B is the Boltzmann constant. The contributions of the total Helmholtz energy are the ideal gas contribution, a^{ig}, the monomer (unbounded) contribution for a chain composed of m_s tangential segments, a^{mono}, and the formation of chain molecules, a^{chain}. For a complete overview of this model, the reader is referred to the original work[21]. Additionally, a summary of the main expressions can be found in Ref. [49]

Within the SAFT-VR-Mie EoS, pure non-associating fluids are characterized by the three Mie parameters $(\lambda, \varepsilon, \sigma)$ plus m_s. The numerical values of these parameters are summarized in Table 2.

According to the original work,[21] the SAFT-VR-Mie EoS is extended to mixtures by using the following combination rules for the unlike parameters for size, σ_{ij}, attractive interaction energy, ε_{ij}, and Mie exponents, λ_{ij}:

$$\sigma_{ij} = (\sigma_i + \sigma_j)/2;$$
$$\varepsilon_{ij} = \sqrt{\varepsilon_i\varepsilon_j}\frac{\sqrt{\sigma_i^3\sigma_j^3}}{\sigma_{ij}^3}(1 - k_{ij});$$
$$(\lambda_{ij} - 3) = \sqrt{(\lambda_{ii} - 3)(\lambda_{jj} - 3)} \tag{7}$$

where k_{ij} is a binary interaction parameter, which is regressed from experimental data of phase equilibria. In this work, this parameter has been obtained by minimizing the error between the predicted and experimental bubble point data [50] using available experimental *PTx* data. Table 3 collects the numerical values of k_{ij}, the cross parameters, the Absolute Average Deviation on pressure (AADP) and the reference data used for fitting. In the Supplementary Information, the *PTx* diagrams are included together with the experimental data used for this fitting.

In order to predict the isothermal bulk phase equilibrium properties (*i.e.*, ρ^L, ρ^V and P^0) from the SAFT-VR-Mie EoS, the following phase equilibrium conditions are applied:

$$\Omega = -P^0 \tag{8}$$

$$\left(\frac{\partial\Omega}{\partial\rho_1}\right)^L_{T^0,V^0,\rho_2^0} = \left(\frac{\partial\Omega}{\partial\rho_1}\right)^V_{T^0,V^0,\rho_2^0} \tag{9}$$

$$\left(\frac{\partial\Omega}{\partial\rho_2}\right)^L_{T^0,V^0,\rho_1^0} = \left(\frac{\partial\Omega}{\partial\rho_2}\right)^V_{T^0,V^0,\rho_1^0} \tag{10}$$

In the latter equations, the superscript 0 represents equilibrium conditions and *L* and *V* refer to liquid and vapor, respectively. ρ_i is the molar density of component *i*, which is related to the molar fraction, x_i, and the molar density of the mixture, ρ, through $\rho_i = x_i\rho$, and Ω is the grand thermodynamical potential, which is defined as:

$$\Omega = a_0 - \rho_1\left(\frac{\partial a_0}{\partial\rho_1}\right)^0 - \rho_2\left(\frac{\partial a_0}{\partial\rho_2}\right)^0 = a_0 - \rho_1\mu_1^0 - \rho_2\mu_2^0 \tag{11}$$

where μ_i is the chemical potential of component *i*.

In summary, Eqs. (6)–(11) are used to predict the pressure and bulk phase equilibrium densities, which are the boundaries of the interfacial or inhomogeneous region. Specific details related to the numerical strategies to solve the phase equilibrium are described by some of us in a recent work.[49].

In this work, the interfacial properties are calculated from the van der Waals square gradient theory (SGT).[18–20] In SGT, the inhomogeneous Helmholtz energy density, *a*, is described by the sum of two contributions: the first part takes into account the Helmholtz energy density for the homogeneous fluid at a local density, a_0, while the second part represents the inhomogeneous contribution of Helmholtz energy by a product of square local-density gradients and a set of characteristic constants, called influence parameters, c_{ij}. For the case of a binary mixture in a planar interface along the *z* coordinate, and considering a geometric mixing rule for the cross-influence parameters (*i.e.*, $c_{12} = c_{21} = \sqrt{c_{11}c_{22}}$), *a* is given by the following expression:

$$a = a_0 + \frac{1}{2}\left[c_{11}\left(\frac{d\rho_1}{dz}\right)^2 + 2\sqrt{c_{11}c_{22}}\left(\frac{d\rho_1}{dz}\right)\left(\frac{d\rho_2}{dz}\right) + c_{22}\left(\frac{d\rho_2}{dz}\right)^2\right] \tag{12}$$

Within the theoretical framework of the SGT, the density distribution, $\rho_i(z)$, is obtained from Eq. (12) when *a* reaches a stationary minimum value. This condition leads to the following algebraic expression:[19,20,18]

$$\sqrt{c_{22}}\left(\mu_1(\rho_1,\rho_2) - \mu_1^0(\rho_1^0,\rho_2^0)\right) = \sqrt{c_{11}}\left(\mu_2(\rho_1,\rho_2) - \mu_2^0(\rho_1^0,\rho_2^0)\right) \tag{13}$$

In this work, μ_i are described by the SAFT-VR-Mie and the influence parameters for the pure components, c_{11} and c_{22} are calculated, independently of temperature and density, using the same molecular parameters used on SAFT-VR-Mie (see Table 2) and and the expression:[54]

$$\sqrt{\frac{c_{ii}}{N_{av}^2\varepsilon_{ii}\sigma_{ii}^5}} = m_{s,i}(0.12008 + 2.21979\alpha_i) \tag{14}$$

Table 3
Molecular parameters for cross interactions

Mixture	k_{ij}	ε_{ij}/k_B (K)	σ_{ij} (Å)	λ_{ij}	%AADP*
CH_4+$C_{10}H_{22}$	−0.03263	270.854	4.168	18.491	0.76 [a]
CH_4+$C_{12}H_{26}$	−0.02199	257.711	4.052	17.365	1.21 [b]
CH_4+$C_{14}H_{30}$	−0.02874	255.011	3.968	17.012	4.00 [c]
CH_4+$C_{16}H_{34}$	−0.05264	278.363	4.092	18.611	7.31 [d]

* $\%AADP = 100(1/N_d)\sum_{i=1}^{N_d}\left|P_i^{exp} - P_i^{cal}\right|/P_{i_i}^{exp}$, where N_d is the number of experimental points used. Experimental data have been taken from: [a] Beaudoin and Kohn [51], Reamer et al. [16], and Rijkers et al. [12]; [b] Rijkers et al. [13], Srivastan et al. [52]; [c] de Leeuw et al. [14], Nourozieh et al. [53]; [d] Glaser et al. [11], Rijkers et al. [15].

where α_i is the van der Waals constant, in this case

$$\alpha_i = C_i\left[\left(\frac{1}{3}\right) - \left(\frac{1}{\lambda_i - 3}\right)\right] \tag{15}$$

By solving Eq. (13), $\rho_1(\rho_2)$ is obtained. Other interfacial properties, such interfacial concentration profiles along the spatial coordinate, the relative Gibbs adsorption, and interfacial tensions, can be calculated from the following expressions:[20,55,19]

$$\left(\frac{d\rho_2}{dz}\right)^2 = 2\left(\Omega + P^0\right)\left[1 + 2\left(\frac{d\rho_1}{d\rho_2}\right) + \left(\frac{d\rho_1}{d\rho_2}\right)^2\right]^{-1}; \quad \left(\frac{d\rho_1}{dz}\right) = \left(\frac{d\rho_1}{d\rho_2}\right)\left(\frac{d\rho_2}{dz}\right)$$

$$\Gamma_{12} = -\left(\rho_1^L - \rho_1^V\right)\int_{-\infty}^{+\infty}\left\{\frac{\rho_2(z) - \rho_2^L}{\rho_2^L - \rho_2^V} - \frac{\rho_1(z) - \rho_1^L}{\rho_1^L - \rho_1^V}\right\}dz \tag{17}$$

$$\gamma = \sqrt{2} \times \int_{\rho_2^{V,0}}^{\rho_2^{L,0}}\left(\left(\Omega + P^0\right)\left[c_2 + 2\sqrt{c_1 c_2}\left(\frac{d\rho_1}{d\rho_2}\right) + c_1\left(\frac{d\rho_1}{d\rho_2}\right)^2\right]\right)^{1/2} d\rho_2 \tag{18}$$

The numerical details involved in the phase equilibrium, and interfacial properties calculations along with an open free software code to perform them have been recently described by some of us.[49]

4. Molecular Dynamics Simulations

MD simulations of bulk phase and interfacial properties of CH_4 + n-alkane (*i.e.*, $C_{10}H_{22}$, $C_{12}H_{26}$, $C_{14}H_{30}$ and $C_{16}H_{34}$) mixtures at 344.15 K are performed in the canonical ensemble (*NVT*). In this ensemble, *N* molecules at a fixed temperature *T* are placed in a parallelepiped simulation cell of a constant volume $V = L_x \times L_y \times L_z$. In this work, the *N* molecules that conform the mixture ($N = N_1 + N_2$) are described as freely-jointed tangent spheres that interact with each other according to an effective pairwise Mie potential.[46] The novelty of the MD simulations performed here is that force field Mie parameters are directly taken from the SAFT-VR-Mie EoS (see Tables 2 and 3), where CH_4 is represented by one single sphere, $C_{10}H_{22}$ as three tangent spheres, $C_{12}H_{26}$ is modeled as four tangent spheres, whereas $C_{14}H_{30}$ and $C_{16}H_{26}$ are is modeled as five tangent spheres. For a complete discussion of SAFT CG-Mie methodology and its top-down parameterization, the reader is directed to the review by Müller and Jackson [22].

In this work, we follow the procedure described by Müller et al. [56] to define the distribution of N_1 and N_2. This procedure is based on the phase equilibrium predictions using SAFT-VR-Mie EoS (see Section 3). All MD simulations are carried out using the same total number of Mie segments, $N_s = (m_1x_1 + m_2x_2)N$, for all the mixtures and at all thermodynamic conditions, $N_s = 8000$. Here m_1 and m_2 are the number of monomeric units and x_1 and x_2 are the mole fractions of components 1 and 2, respectively. This is done to ensure that all the systems are formed from the same number of monomers or interacting sites irrespective of the particular chain lengths in the different mixtures. We choose $L_x = L_y = 12\sigma = 55.02$ Å, being σ the the largest monomeric diameter used in this work (n-decane). Note that we have chosen *x*- and *y*-axis as the directions containing the interface and the *z*-axis direction perpendicular to the VL interface. Since we are dealing with mixtures, not only ρ_L, the liquid density, and ρ_V, the vapor density, vary with pressure, but also the composition of the mixture in both phases, x_1 and y_1. Due to this, L_z is chosen appropriately to ensure phase separation at the corresponding thermodynamic conditions for all mixtures.

For a given mixture and pressure, we take ρ_L, ρ_V, x_1, and y_1 as obtained from the SAFT-VR-Mie predictions and use this information as starting values to prepare homogeneous liquid and vapor systems with the appropriate compositions in two parallelepiped simulation boxes. L_x and L_y are chosen as explained previously and L_z is fixed to reproduce the theoretical values of ρ_L and ρ_V. Depending on the mixture and pressure, L_z varies from $\sim 57\sigma \sim 261$ Å, at low pressures, to $\sim 23\sigma \sim 105$ Å, at high pressures. The two simulations boxes are then linked up forming a vapor-liquid–vapor system, which constitutes the initial simulation box used to study the coexisting and interfacial properties of the mixture at the desired pressure. The number of molecules of each species, the total length of the simulation box along the *z*-axis (L_z), and the equilibrium pressure obtained at the end of the *NVT* simulations of all the mixtures are summarized in the Supplementary Information. We use periodic boundary conditions in all three dimensions and a cutoff radius $r_c = 6\sigma = 27.504$ Å, where $\sigma = 4.584$ Å, the largest value of the size parameter of the Mie intermolecular potential used.

We use the GROMACS (VERSION 4.6.1)[57]simulation suite to perform *NVT* MD simulations. We use the Verlet leapfrog algorithm with a time step of 0.001 ps, and the Nosé-Hoover thermostat, with a relaxation constant of $\tau = 1.0$ ps. The vapor–liquid interfacial system is equilibrated for at least 10 ns. Additional 50 ns are also employed to calculate averages (production stage). Errors for equilibrium pressure and interfacial tension are estimated dividing the production period into *M* (independent) blocks. The statistical error is estimated from the standard deviation of the average $\overline{\sigma}/\sqrt{M}$. Here $\overline{\sigma}$ is the variance of the block averages and $M = 10$ in this work.

In order to characterize the bulk phase equilibria and interfacial properties, the concentration profiles $\rho_i(z)$ are calculated by dividing the system in 200 slabs along the *z* direction. The molecular density profiles, $\rho_i(z)$, are obtained by assigning the position of each bead center, z_i, to the corresponding slab and constructing the molecular density from mass balance considerations. From the profiles, we have obtained the bulk liquid and vapor densities and the total density averaging $\rho_1(z), \rho_2(z)$ and $\rho(z) = \rho_1(z) + \rho_2(z)$ over the appropriate regions sufficiently removed from the interfacial region. The statistical uncertainties of these values are estimated from the standard deviation of the mean values. From the $\rho_i(z)$ profiles, the surface activity (or absolute adsorption) of species along the interfacial region is also evaluated, and the relative Gibbs adsorption isotherm of a species *i* relative to a species *j* (Γ_{ij}) (see Eq. (17)) can be obtained from the MD approach. The equilibrium pressure, *P*, and interfacial tension, γ, are obtained using the Irving-Kirkwood method, where the pressure tensor diagonal elements are calculated employing the virial expression. The vapor pressure corresponds to the normal component of the pressure tensor, $P = P_{zz}$, while the interfacial tension is obtained using the pressure route:

$$\gamma = \frac{L_z}{2}\left[\langle P_{zz}\rangle - \frac{\langle P_{xx}\rangle + \langle P_{yy}\rangle}{2}\right] \tag{19}$$

In the equation above, $\langle\cdots\rangle$ represents ensemble average of the pressure tensor, and the leading factor (1/2) comes from having two interfaces present in the system. The details related to the technical implementation of the previous expressions and their evaluation have been discussed extensively in the literature (see Allen and Tildesley [58], Müller et al. [56] and references therein).

5. Results and Discussion

In this work, experimental determinations, theoretical predictions, and molecular simulations are combined to explore and simultaneously describe the phase equilibria and the interfacial

Table 4
Phase equilibria bulk mass density measurements for $CH_4(1)+C_nH_{2n+2}(2)$ mixtures at 344.15 K and different pressures.*

$CH_4(1)+C_{10}H_{22}(2)$			$CH_4(1)+C_{12}H_{26}(2)$		
P (MPa)	ρ_L (kg/m^3)	ρ_V (kg/m^3)	P (MPa)	ρ_L (kg/m^3)	ρ_V (kg/m^3)
0.10	705.249	1.091	0.10	724.638	0.849
0.30	704.498	2.708	0.32	725.040	2.180
5.00	684.184	31.965	1.99	718.996	12.070
10.00	661.958	64.209	3.99	712.254	24.170
15.00	639.581	98.494	6.10	705.530	37.660
19.86	617.754	133.601	8.04	699.513	50.350
			10.05	693.255	63.640
			12.06	686.783	76.710
			14.07	679.906	90.350
			16.06	672.508	103.650
			18.03	664.424	116.860
			20.02	655.305	130.090
$CH_4(1)+C_{14}H_{30}(2)$			$CH_4(1)+C_{16}H_{34}(2)$		
P (MPa)	ρ_L (kg/m^3)	ρ_V (kg/m^3)	P (MPa)	ρ_L (kg/m^3)	ρ_V (kg/m^3)
0.10	740.324	1.876	0.10	752.266	0.565
0.34	740.905	2.316	0.36	752.073	2.883
1.98	737.221	11.724	2.02	750.434	12.039
4.09	733.282	24.714	4.04	747.617	24.598
6.08	729.692	37.209	6.09	744.027	37.410
8.05	725.749	50.035	8.01	740.176	49.697
10.04	721.079	63.096	10.02	735.829	62.851
12.06	715.544	76.439	12.03	731.349	76.129
14.16	709.079	90.450	14.07	726.865	89.557
16.02	703.059	102.570	16.04	722.786	102.358
18.06	696.687	115.764	18.04	719.086	115.110
20.12	691.300	140.713	20.01	716.061	127.385

*The standard uncertainties are $u(P) = 0.03$ kPa and $u(T) = 0.1$ K. Instrument standard uncertainty is $\rho = 0.4$ kg/m^3. The combined expanded uncertainty (considering a 0.95 level of confidence, $k = 2$) is $U(\rho) = 1.1$ kg/m^3.

properties for four asymmetric binary mixtures, namely CH_4 + ($C_{10}H_{22}$, $C_{12}H_{26}$, $C_{14}H_{30}$ and $C_{16}H_{34}$) at the isothermal condition of 344.15 K and over a broad pressure range, where VLE is the only phase equilibrium type. The theoretical modeling and molecular simulation use the parameter described in Tables 2 and 3, which were obtained from corresponding state principia,[47,48] and *PTx* experimental data from other data sources. In that sense, the results from the theoretical approach and MD simulations can be seen as an unbiased prediction and a test of the transferability of the thermodynamic models. The main results for this trilogy approach are described below, where some comparison to previous results are included.

5.1. Bulk Phase equilibrium

As described in Section 3, the bulk phase equilibrium is the boundary of the interfacial region. In this section, the equilibria bulk mass densities, as functions of pressure, are described for the four methane based binary mixtures using our three-pronged approach. The results are compared to the available experimental data, previous theoretical results and MD simulations. Table 4 summarizes the new experimental measurements, whereas Table 5 collects our MD results for the phase equilibria bulk mass densities in the VLE region at the isothermal condition of 344.15 K for the CH_4 + n-alkanes ($C_{10}H_{22}$, $C_{12}H_{26}$, $C_{14}H_{30}$ and $C_{16}H_{34}$) mixtures.

Table 5
Phase equilibria results from molecular dynamics for $CH_4(1)+C_nH_{2n+2}(2)$ mixtures at 344.15 K and different pressures. The error estimation is explained in the text. 1.2(3) refers to 1.2 ± 0.03

$CH_4(1)+C_{10}H_{22}(2)$			$CH_4(1)+C_{12}H_{26}(2)$		
P (MPa)	ρ_L (kg/m^3)	ρ_V (kg/m^3)	P (MPa)	ρ_L (kg/m^3)	ρ_V (kg/m^3)
2.298(6)	685.7(6)	13.41(4)	2.266(8)	714.5(5)	13.02(7)
4.612(9)	672(1)	27.25(6)	4.69(1)	703(1)	27.09(9)
7.14(2)	660.0(8)	42.8(1)	7.01(1)	691.9(2)	41.2(1)
9.42(2)	645.7(9)	57.4(1)	9.53(2)	681(2)	57.0(2)
14.17(2)	619(2)	88.6(2)	14.23(4)	660(1)	86.42(9)
19.05(3)	594(2)	122.4(3)	18.94(4)	635(2)	115.6(2)
23.48(4)	558(2)	154.6(7)	23.66(5)	613(2)	145.4(5)
25.59(6)	547(3)	171.3(8)	25.67(5)	597(2)	159.9(4)
27.66(1)	523(2)	191.9(9)	28.08(5)	581(2)	175.0(9)
$CH_4(1)+C_{14}H_{30}(2)$			$CH_4(1)+C_{16}H_{34}(2)$		
P (MPa)	ρ_L (kg/m^3)	ρ_V (kg/m^3)	P (MPa)	ρ_L (kg/m^3)	ρ_V (kg/m^3)
2.341(6)	750.7(9)	13.25(4)	2.51(1)	751.9(7)	14.4(2)
4.97(1)	741(1)	27.27(5)	4.975(8)	743(1)	29.0(2)
7.00(2)	728.6(9)	41.12(5)	7.49(2)	734(8)	42.92(6)
9.41(2)	718.2(7)	55.78(7)	9.94(2)	727.3(8)	58.8(1)
14.26(2)	697.2(9)	85.8(1)	14.99(2)	713.1(6)	89.4(1)
19.12(3)	674(2)	115.2(2)	20.10(2)	699.2(8)	119.4(1)
23.82(3)	657(2)	142.7(3)	24.93(3)	686.0(8)	144.4(3)
26.00(5)	640(2)	154.3(3)	27.40(2)	680(1)	156.8(2)
26.08(4)	643(2)	155.4(4)	29.94(3)	673(2)	170.1(4)

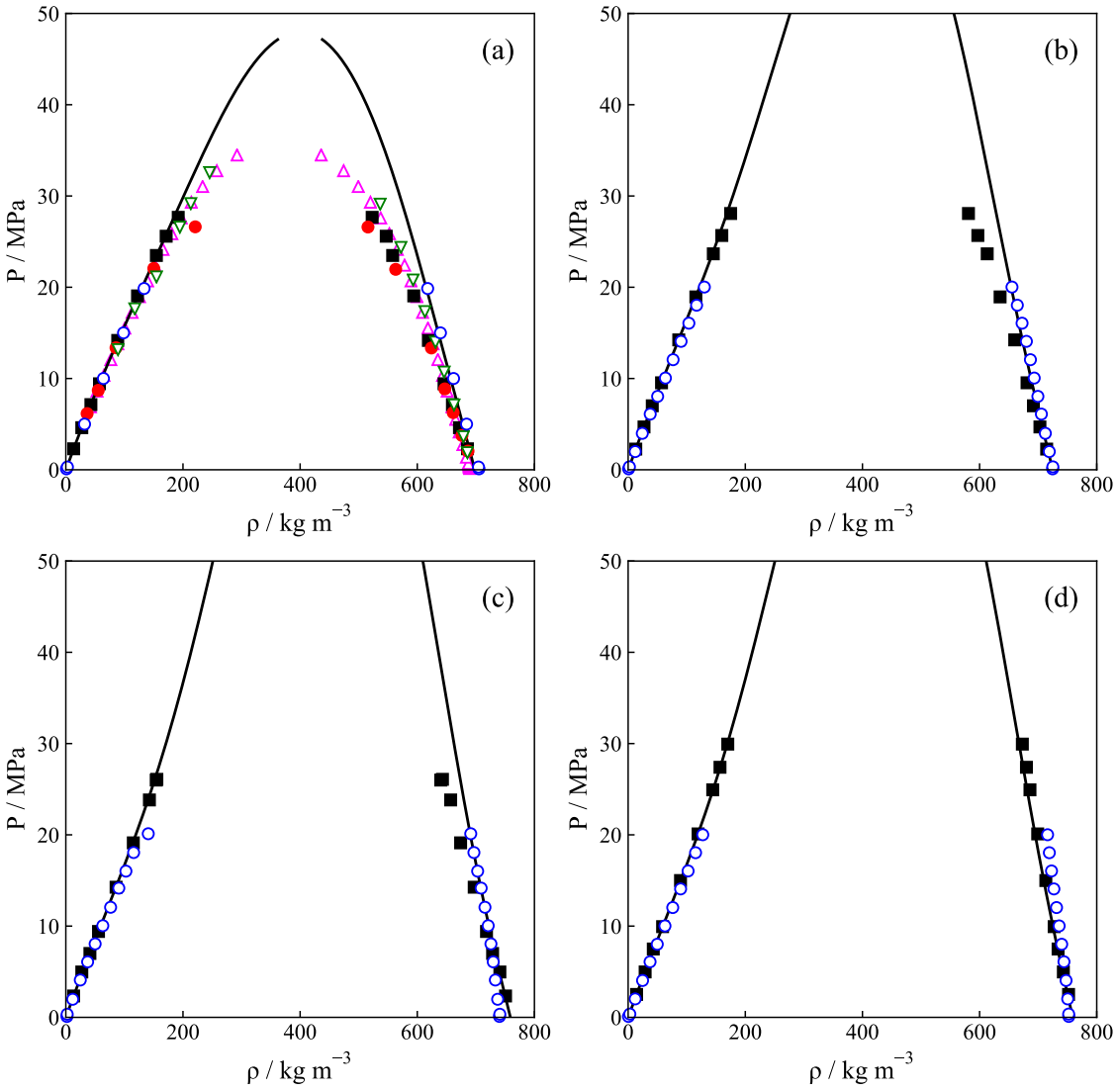

Fig. 1. Pressure–mass density ($P-\rho$) diagram for $CH_4(1)+C_nH_{2n+2}(2)$ mixtures at 344.15 K. (a) $CH_4+C_{10}H_{22}$; (b) $CH_4+C_{12}H_{26}$; (c) $CH_4+C_{14}H_{30}$; (d) $CH_4+C_{16}H_{34}$. –, SAFT-VR-Mie EoS with binary interaction parameter, k_{12}, given in Table 3. Experimental data: ○ (blue) this work; △, (pink) Reamer et al. [16]; ▽, (green) Pereira et al. [5]; MD simulations: ■, this work; •,(red) Choudhary et al. [7].

Table 6
Absolute Average Deviation (%AAD) in liquid (ρ^L) and vapor (ρ^V) mass saturated densities for $CH_4(1)+C_nH_{2n+2}(2)$ mixtures at 344.15 K in the whole range of pressures considered.

	$CH_4(1)+C_{10}H_{22}(2)$		$CH_4(1)+C_{12}H_{26}(2)$	
Method	ρ^L	ρ^V	ρ^L	ρ^V
SAFT-VR-Mie + SGT	0.78	5.39	0.58	5.50
MD	2.95	5.82	2.02	5.02
	$CH_4(1)+C_{14}H_{30}(2)$		$CH_4(1)+C_{16}H_{34}(2)$	
Method	ρ^L	ρ^V	ρ^L	ρ^V
SAFT-VR-Mie + SGT	0.73	7.44	0.34	7.38
MD	1.97	11.30	1.26	6.01

In order to compare the reported experimental data, the theoretical predictions, and the MD results, Fig. 1 shows the pressure–mass density ($P-\rho$) diagrams for each binary mixture. This figure includes the liquid and vapor mass saturated densities as a function of pressure measured in this work (*cf.* Table 4), the SAFT-VR-Mie EoS predictions, MD results (*cf.* Table 5) as well as the experimental data previously reported by Pereira et al. [5] and Reamer et al. [16] for methane + n-decane, and MD results for methane + n-decane from Choudhary et al. [7].

Fig. 1 (a) ($CH_4+C_{10}H_{22}$) compares visually the experimental data with previous results from the literature. No apparent systematic error is seen, as our results fall between those of Ref. Pereira et al. [5], Choudhary et al. [7] and Reamer et al. [16]. Fig. 1 also present a direct comparison between the three methodologies (*i.e.*, experimental determination, theoretical modeling and MD simulation). According to the results, the vapor mass density increases, whereas the liquid mass density decreases as the pressure increases or the molecular chain decreases. It is also observed that

Table 7
Absolute Average Deviation (%AAD) in liquid (ρ^L) and vapor (ρ^V) mass saturated densities for $CH_4(1)$+$C_{10}H_{22}(2)$ mixture at 344.15 K. References indicate the works in the literature used to compare our measurements, theoretical predictions and computer simulation values.

Method	ρ^L	ρ^V
Densimetry	2.06 [5]	2.72 [5]
	2.77 [16]	0.86 [16]
SAFT-VR-Mie + SGT	2.41 [5]	8.25 [5]
	1.43 [16]	2.76 [16]
MD	1.25 [7]	4.91 [7]

the density difference ($\rho^L - \rho^V$) increases as the molecular chain length increases. This general behavior agrees with the expected results and is validated from the three used approaches.

Table 6 summarizes the Absolute Average Deviation (AAD) for theoretical predictions and MD simulations. From Fig. 1 and Table 6, an excellent agreement is observed between both methodologies. The results of MD and theoretical calculations are purposely not fitted to the experimental results but are based on the previously available information of the methane-alkane systems. The predictive and transferable nature of the models is an aspect we want to highlight in this contribution. However, it is noted that the SAFT-VR-Mie results considerably deviates near the mixture's critical point. This deviation is a known deficiency of molecular-based EoS whose parameters do not consider the critical point, but it can be solved by incorporating crossover treatments or by using an EoS parametrized at the critical point as it was demonstrated by Pereira et al. [5] and Choudhary et al. [7,8]using an optimized Peng-Robinson EoS. [59].

In order to compare the results reported here (*i.e.*, experimental determination, theoretical predictions and MD results), the values of the bulk density of vapor and liquid phases are compared to available information at the same conditions. Table 7 summarizes the corresponding AAD for the case of methane + n-decane mixture. The bulk densities have been previously measured by Reamer et al. [16] at 344.26 K and more recently by Pereira et al. [5] at 343.15 K, and reported from MD by Choudhary et al. [7].

From the Table 7 is possible to observe that the reported experimental density of liquid and vapor bulk phases agree to previous densimetry values, the theoretical approach reproduces the experimental values within the expected deviations, and the reported MD agree with other MD simulations. However, we point out feat this work employs a CG force field that has an apparent lower fidelity than the UA force field employed in by Choudhary et al. [7] which requires significantly more computational resources.

5.2. Interfacial Tensions

In this work, the three-pronged approach has been used to describe the variation of the interfacial tension with the pressure at the same isothermal condition as the bulk fluid densities. Tables 8 and 9 collect the tensiometry data and MD results, respectively.

Fig. 2 displays the interfacial tension-pressure ($\gamma - P$) diagram for CH_4 + n-alkanes ($C_{10}H_{22}$, $C_{12}H_{26}$, $C_{14}H_{30}$ and $C_{16}H_{34}$) mixtures at 344.15 K. This figure includes interfacial tensions measured in this work (*cf.* Table 8), SAFT-VR-Mie EoS coupled to SGT calculations, MD results (*cf.* Table 9), as well as the available information (*i.e.*, tensiometry data for methane + n-decane, [17,5] and MD results for methane + n-decane [7]).

Table 8
Interfacial tension measurements for $CH_4(1)$+$C_nH_{2n+2}(2)$ mixtures at 344.15 K∗ and different pressures.

$CH_4(1)$+$C_{10}H_{22}(2)$		$CH_4(1)$+$C_{12}H_{26}(2)$		$CH_4(1)$+$C_{14}H_{30}(2)$		$CH_4(1)$+$C_{16}H_{34}(2)$	
P (MPa)	γ (mN/m)	P (MPa)	γ (mN/m)	P (MPa)	γ (mN/m)	P (MPa)	γ (mN/m)
0.10	18.96	0.10	20.70	0.10	22.03	0.10	23.02
0.30	18.40	0.32	19.63	0.34	21.71	0.36	22.66
5.00	13.03	1.99	18.03	1.98	19.20	2.02	20.78
10.00	9.29	3.99	15.95	4.09	16.70	4.04	18.51
15.00	5.51	6.10	13.87	6.08	13.80	6.09	16.24
19.86	3.69	8.04	12.31	8.05	11.36	8.01	14.18
		10.05	10.89	10.04	9.74	10.02	12.13
		12.06	9.48	12.06	8.51	12.03	10.21
		14.07	8.08	14.16	7.41	14.07	8.42
		16.06	6.81	16.02	6.53	16.04	6.89
		18.03	5.72	18.06	5.62	18.04	5.54
		20.02	4.78	20.12	4.76	20.01	4.46

∗ The standard uncertainties are $u(P) = 0.03$ kPa and $u(T) = 0.1$ K. Instrument standard uncertainty is $\gamma = 0.05$ mN/m. The combined expanded uncertainty (considering a 0.95 level of confidence, $k = 2$) is $U(\gamma) = 0.1$ mN/m.

Table 9
Interfacial tension from molecular dynamics for $CH_4(1)$+$C_nH_{2n+2}(2)$ mixtures at 344.15 K and different pressures. The error estimation is explained in the text. 1.2(3) refers to 1.2 ± 0.03.

$CH_4(1)$+$C_{10}H_{22}(2)$		$CH_4(1)$+$C_{12}H_{26}(2)$		$CH_4(1)$+$C_{14}H_{30}(2)$		$CH_4(1)$+$C_{16}H_{34}(2)$	
P (MPa)	γ (mN/m)	P (MPa)	γ (mN/m)	P (MPa)	γ (mN/m)	P (MPa)	γ (mN/m)
2.298(6)	17.4(2)	2.266(8)	19.2(2)	2.341(6)	20.8(2)	2.51(1)	22.0(1)
4.612(9)	14.7(1)	4.69(1)	16.6(2)	4.97(1)	18.4(2)	4.975(8)	20.0(3)
7.14(2)	12.7(2)	7.01(1)	14.4(2)	7.00(2)	15.6(2)	7.49(2)	16.7(2)
9.42(2)	10.8(2)	9.53(2)	12.1(2)	9.41(2)	13.9(1)	9.94(2)	15.1(2)
14.17(2)	7.6(1)	14.23(4)	8.7(1)	14.26(2)	10.2(1)	14.99(2)	11.4(3)
19.05(3)	4.9(1)	18.94(4)	6.4(1)	19.12(3)	7.4(2)	20.10(2)	8.8(2)
23.48(4)	2.9(1)	23.66(5)	4.6(1)	23.82(3)	5.5(1)	24.93(3)	7.0(2)
25.59(6)	2.1(2)	25.67(5)	3.44(9)	26.00(5)	4.7(1)	27.40(2)	6.0(1)
27.66(1)	1.5(1)	28.08(5)	2.8(1)	26.08(4)	4.8(1)	29.94(3)	5.48(9)

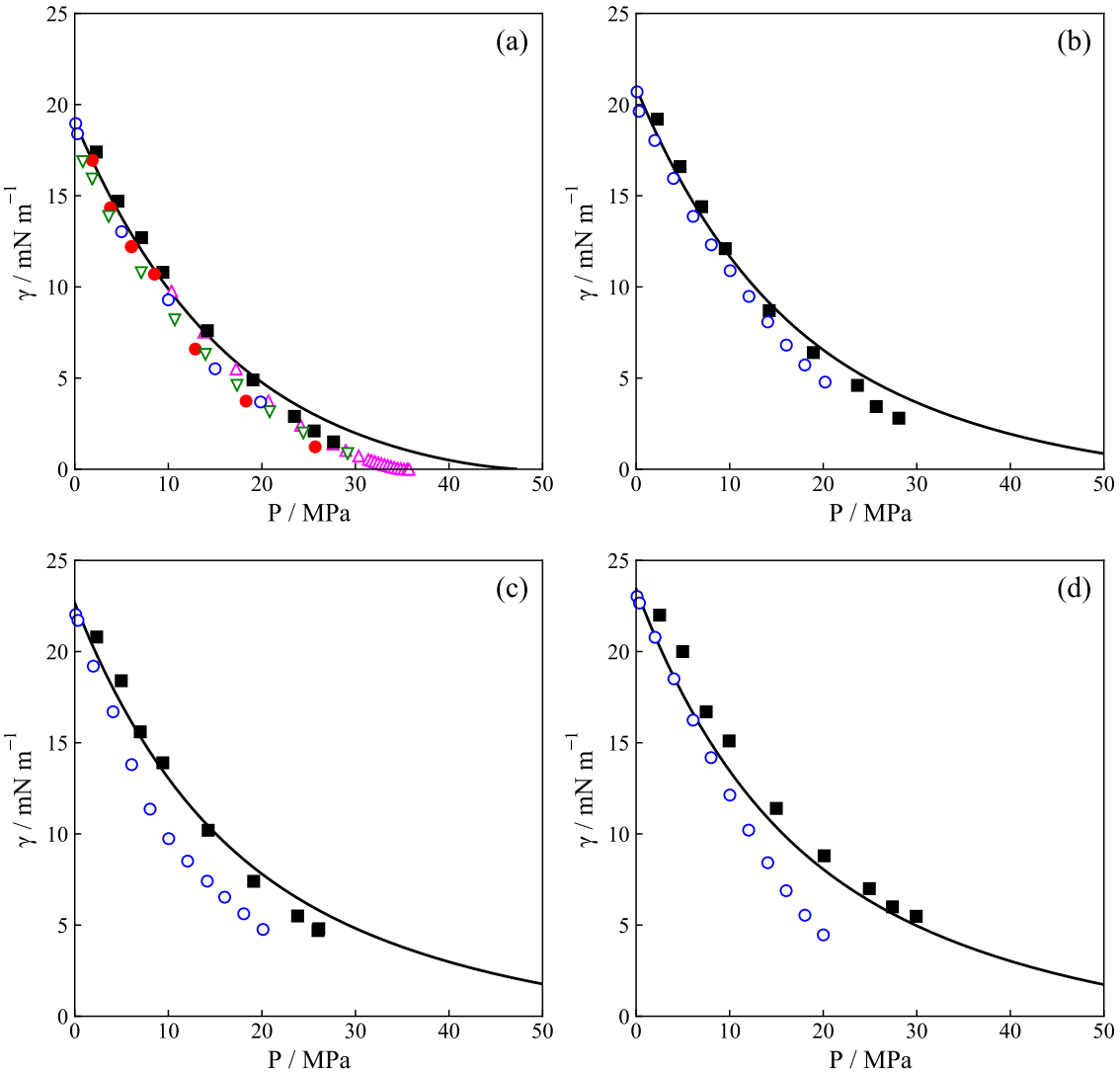

Fig. 2. Interfacial–Pressure ($\gamma - P$) diagram for $CH_4(1)+C_nH_{2n+2}(2)$ mixtures at 344.15 K. (a) $CH_4+C_{10}H_{22}$; (b) $CH_4+C_{12}H_{26}$; (c) $CH_4+C_{14}H_{30}$; (d) $CH_4+C_{16}H_{34}$. –, SAFT-VR-Mie EoS combined with SGT with binary interaction parameter, k_{12}, given in Table 3. Experimental data: ○, (blue) this work; △,(pink) Stegemeier et al. [17]; ▽, (green) Pereira et al. [5]; MD simulations: ■, this work; •, (red) Choudhary et al. [7].

From Fig. 2, it is possible to observe that the interfacial tension, γ, decreases as the pressure increases and its value tends to zero as the pressure tends to its critical value. Additionally, at a fixed isobaric condition, the interfacial tension increases as the molecular chain increases, as it is expected. Comparing the reported results, a good agreement is observed between the three approaches presented herein from 0.1 to 10 MPa, but the agreement worsens at high pressures due to the inability of the models to describe the fluid behavior near the critical region. This fact has been noted for densities, which directly impact the interfacial tension results.

Additionally, the reported results show that as the molecular chain length increases, the deviation with respect to experimental data increases. This is presumably a consequence of the fact that as molecular chain length increases, additional restrictions, such as intramolecular interactions (bond stretching and angle bending), which are not included, become incresingly relevant. In this work, we opted for a fully predictive and complete transferable approach between the theoretical modeling and molecular simulation, but further refinements can be incorporated by including these restrictions, as was demonstrated by one of us. [60] The corresponding statistical deviations are summarized in Table 10, where the deviations are reported from 0.1 to 10 MPa (%ADD-γ_{hr}) and over the full pressure range (%AAD-γ).

The results reported in Tables 8 and 9, and statistics reported in Table 10 are in very good agreement with the available tensiometry for the methane + n-decane mixture from experimental determinations, [61,16,51,4,12,52,5] theoretical predictions from SGT, [6,5,7] and from DFT combined with SAFT,[9] as well as from molecular simulations of Choudhary et al. [7,8] A summary of this comparison is collected in Table 11, which compares the corresponding %AAD-γ_{hr} and %AAD-γ.

5.3. Interfacial profiles: the $z - \rho_i$ projections

In addition to the bulk phase densities and interfacial tensions, theoretical modeling, and MD simulation provide a route to explore interfacial properties such as the concentration profiles in the direction normal to the interface (the $z - \rho_i$ projections), from which surface activity or absolute adsorption of species in

Table 10
Absolute Average Deviation (%AAD) in interfacial tension (γ) for $CH_4(1)+C_nH_{2n+2}(2)$ mixtures at 344.15 K and different range of pressure as indicated in the text.

	$CH_4(1)+C_{10}H_{22}(2)$		$CH_4(1)+C_{12}H_{26}(2)$	
Method	%AAD-γ_{hr}	%AAD-γ	%AAD-γ_{hr}	%AAD-γ
SAFT-VR-Mie + SGT	3.43	14.12	4.67	12.04
MD	3.99	13.17	8.56	15.98
	$CH_4(1)+C_{14}H_{30}(2)$		$CH_4(1)+C_{16}H_{34}(2)$	
Method	%AAD-γ_{hr}	%AAD-γ	%AAD-γ_{hr}	%AAD-γ
SAFT-VR-Mie + SGT	15.95	32.73	5.67	31.41
MD	26.44	41.63	15.97	32.29

Table 11
Absolute Average Deviation (%ADD) in the interfacial tension (γ) for $CH_4(1)+C_{10}H_{22}(2)$ mixture at 344.15 K and different range of pressure as indicated in the text.

Method	%AAD-γ_{hr}	%AAD-γ
Tensiometry	–––	3.77 [5]
	–––	6.55 [17]
SAFT-VR-Mie + SGT	10.15 [5]	35.49 [5]
	0.89 [17]	48.33 [17]
	8.38 [7]	22.49 [7]

the interfacial region can be evaluated. Specifically, Fig. 3 showcases the $z-\rho_i$ projections for three different pressures (or equivalently liquid molar fractions) as obtained from the SGT and the CG MD simulations.

In this latter figure, only one vapor–liquid interface is displayed, as the system is symmetric. In the density profiles, a positive surface activity (or absolute adsorption) is seen for CH_4 (*i.e.*, $d\rho_1/dz = 0; d^2\rho_1/dz^2 < 0$ in the interfacial region), whereas C_nH_{2n+2} does not exhibit surface activity (or absolute adsorption). From this figure, it is noted that the CH_4 surface activity increases as its liquid

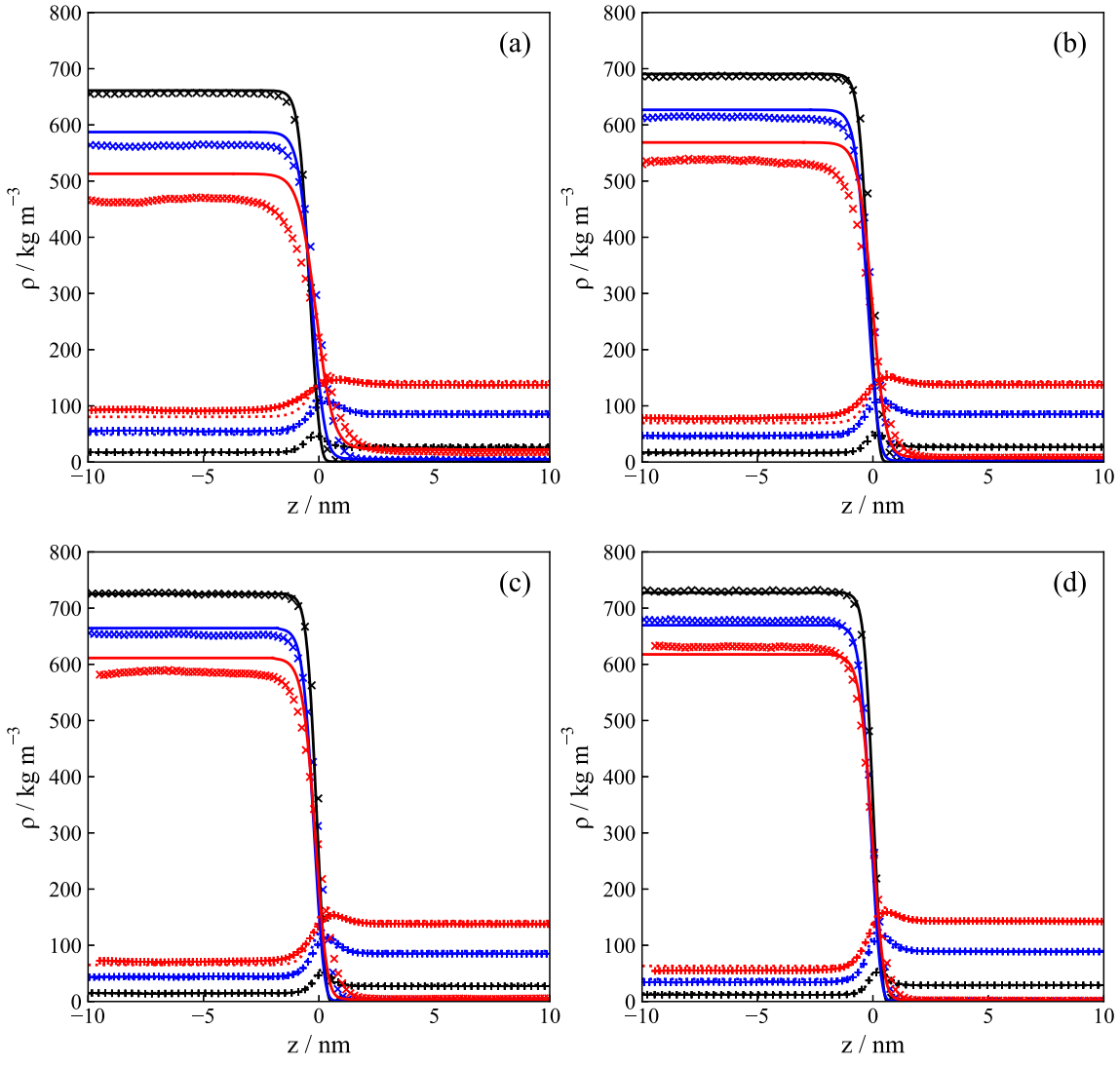

Fig. 3. Density profiles of the (a) CH_4+$C_{10}H_{22}$, (b) CH_4+$C_{12}H_{26}$, (c) CH_4+$C_{14}H_{30}$ and (d) CH_4+$C_{16}H_{34}$ mixtures at 344.15 K and 5 (black), 15 (blue) and 25 MPa (red). Continuous and dotted curves correspond to predictions as obtained from the SAFT-VR-Mie combined with SGT with binary interaction parameter k_{12} given in Table 3 for components 2 and 1, respectively. MD computer simulation results are represented by "+" and n-alkane by "×" for CH_4 and n-alkanes, respectively.

mole fraction or equilibrium pressure increases. Comparing the surface activity of CH_4, it is possible to observe that a fixed pressure, the maximum value increases as the molecular chain length increases.

The SGT predictions are confirmed by the MD simulations, and agree with observations reported by Pereira et al. [6,9,5,7]. The MD results in Fig. 3 exhibit a slight sub-prediction of the profiles, which is caused, in part, by the inaccuracies in the determination of the bulk phases, especially at the highest pressures considered.

Considering the definition of enrichment of component *i* at the interface, E_i, introduced by Becker et al. [62] (*i.e*, $E_i = \max(\rho_i(z))/\max(\rho_i^v, \rho_i^l)$), it is observed that E_{CH_4} decreases as the pressure increases but its approximately constant with the increment of the molecular chain of the larger hydrocarbon. Finally, comparing the surface activity (absolute adsorption) of CH_4 in CH_4+C_nH_{2n+2} mixtures to CO_2 in CO_2+C_nH_{2n+2} mixtures at same isothermal and isobaric conditions, [23,37], it is possible to conclude that CO_2 displays higher surface activity than CH_4. In fact, it is observed that $E_{CO_2} \approx 2 \times E_{CH_4}$.

5.4. Relative Gibbs adsorption isotherm

The surface activity of CH_4 observed in $CH_4(1)$ + $C_nH_{2n+2}(2)$ mixtures can be quantified by means of the relative Gibbs adsorption isotherm, Γ_{12}, of $CH_4(1)$ with respect to $C_nH_{2n+2}(2)$ (see Eqs. (3) and (17)). Fig. 4 displays the variation of Γ_{12} as a function of pressure obtained in this work by using the three approaches. This figure also includes experimental results reported by Pereira et al. [5] and MD results from Choudhary et al., [7].

From these results, it is possible to observe that although Γ_{12} increases as the pressure increases, it reaches a maximum value. This maximum in Γ_{12} reflects an adsorption saturation limit. The Γ_{12} behavior predicted by SGT is confirmed by MD results as well as the approximate approach obtained from experimental data and the theoretical and MD results of Pereira et al. [5], Choudhary et al. [7]. Γ_{12} is similar for all CH_4 + n-alkane mixtures, as is expected from the results reported in Section 5.3. However, it is noted that the Gibbs relative adsorption displays the same behavior for all mixtures until it reaches the maximum value. Past this point, the

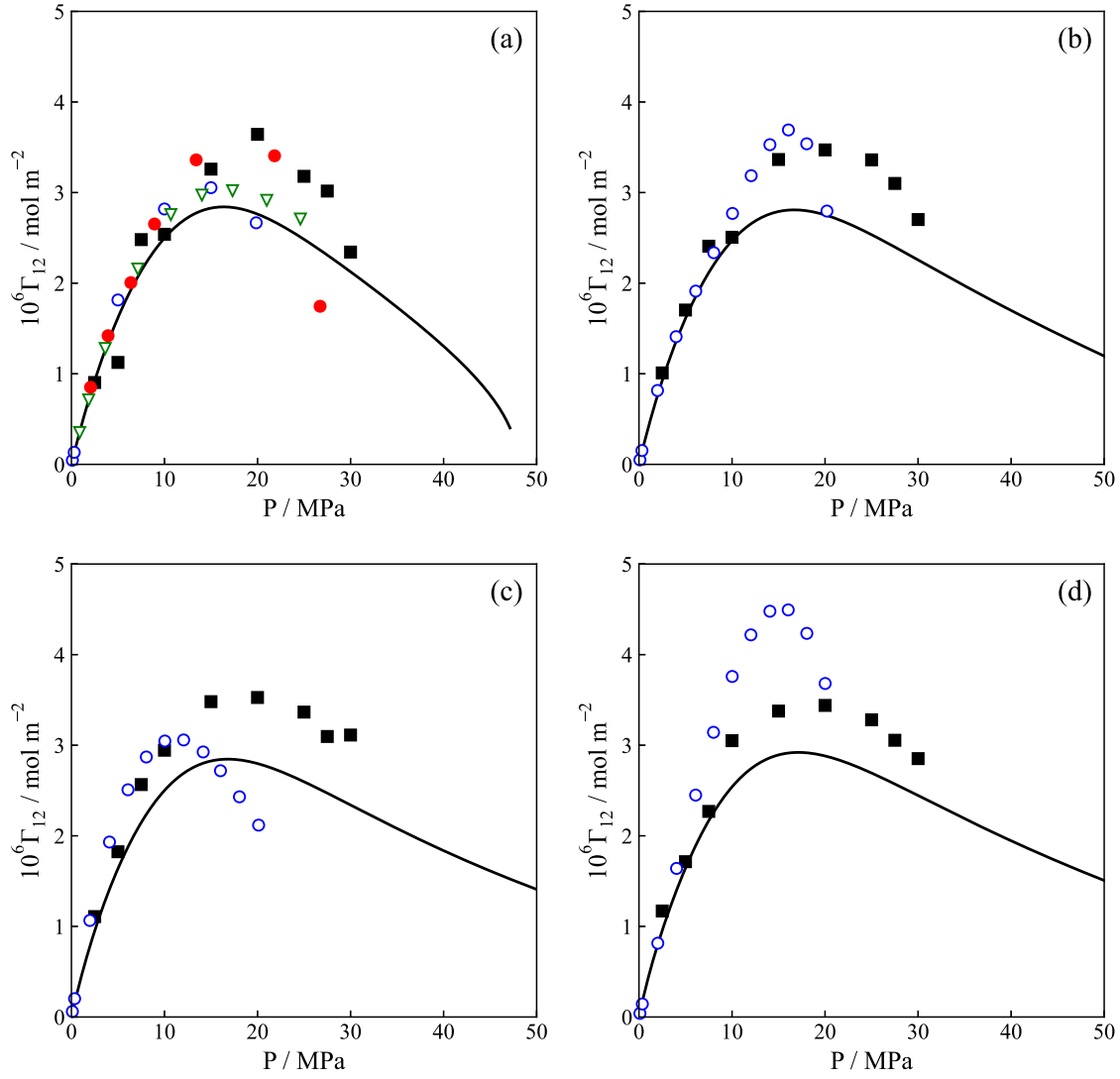

Fig. 4. Relative Gibbs adsorption isotherm, Γ_{12}, for $CH_4(1) + C_nH_{2n+2}(2)$ mixtures at 344.15 K as a function of pressure, *P*. (a) CH_4+$C_{10}H_{22}$; (b) CH_4+$C_{12}H_{26}$; (c) CH_4+$C_{14}H_{30}$; (d) CH_4+$C_{16}H_{34}$. –, SAFT-VR-Mie EoS combined with SGT with binary interaction parameter, k_{12}, given in Table 3 and Eq. 17; ◯, Eq. 3 and the tensiometry data; ■, MD (Eq. 17); ▽, Pereira et al. [5]; •, Choudhary et al. [7].

Gibbs relative adsorption decreases sharply as the molecular chain length decreases.

6. Conclusions

In this work, the bulk phase equilibria (*i.e.*, pressure, liquid and vapor mass densities) and interfacial properties (*i.e.*, interfacial concentration, adsorption and interfacial tension) for methane + n-alkane (*i.e.*, n-decane, n-dodecane, n-tetradecane, n-hexadecane) binary mixtures have been described by using experimental determinations, predictive theoretical modeling and MD simulation at the isothermal condition of 344.15 K and over a broad pressure range, observing a good agreement between the three approaches. The results show that the vapor mass density increases, whereas the liquid mass density and interfacial tension decrease as either the pressure or the length of molecular chian increase This general behavior is expected and is exhibited across all three approaches. Interfacial profiles show a positive surface activity (or absolute adsorption) of methane on the interfacial region increasing as the pressure (or liquid mole fraction of methane) increases, whereas longer n-alkanes do not exhibit surface activity. This behavior is reproduced by the theoretical results and molecular simulations and shows up in the relative Gibbs adsorption isotherm of methane on the n-alkane. These latter results show that the methane relative adsorption increases as the pressure increases and then reaches a maximum value. This maximum value reflects an adsorption saturation limit of methane. It is noted that the simulations and the equation of state should provide, by design, the same resulting volumetric properties over a wide range of parameters capable of representing both simple and very asymmetric mixtures. However, the results shown here and other recently reported in the literature (see for instances Aasen et al. [63] and Zheng et al. [64]) suggest that the critical region of mixtures is not accurately captured by the equation of state in a pressure - explicit representation. While this is a common feature of classical analytical equation of state, SAFT-VR-Mie includes a third order perturbation correction that allows the accurate depiction of the critical region for the monomer term. Notwithstanding, the treatment of mixtures might have to be revised.

Declaration of Competing Interest

The authors declare that they have no known competing financial interests or personal relationships that could have appeared to influence the work reported in this paper.

Acknowledgments

This work was financed by FONDECYT, Santiago, Chile (Project 1190107). E.A.M. acknowledges the support from the U.K. EPSRC through research grants to the Molecular Systems Engineering group (Grant Nos. EP/E016340, EP/J014958). The authors also acknowledge the Centro de Supercomputación de Galicia (CESGA, Santiago de Compostela, Spain) for providing access to computing facilities, Spanish Ministerio de Economía, Industria y Competitividad (Grant No. FIS2017–89361-C3-1-P), Junta de Andalucía (Grant No. P20-00363), both co-financed by EU FEDER funds, and Universidad de Huelva.

Appendix A. Supplementary material

Supplementary data associated with this article can be found, in the online version, at https://doi.org/10.1016/j.molliq.2021.116918.

References

[1] J.G. Speight, The Chemistry and Technology of Petroleum, CRC Press, 2014.
[2] P. van Konynenburg, R. Scott, Philos. Trans. R. Soc. London, Ser. A 298 (1980) 495.
[3] A.J. Davenport, J.S. Rowlinson, Trans. Faraday Soc. 59 (1963) 78.
[4] M.P.W.M. Rijkers, Retrograde condensation of lean natural gas Ph.D. thesis, Delft University of Technology, 1991.
[5] L.M.C. Pereira, A. Chapoy, R. Burgass, B. Tohidi, J. Chem. Thermodyn. 97 (2016) 55.
[6] C. Miqueu, B. Mendiboure, C. Graciaa, J. Lachaise, Fluid Phase Equilib. 218 (2004) 189.
[7] N. Choudhary, A.K.N. Nair, M.F.A.C. Ruslan, S. Sun, Sci. Rep. 9 (2019) 19784.
[8] N. Choudhary, M.F.A.C. Ruslan, A.K.N. Nair, S. Sun, Ind. Eng. Chem. 60 (2021) 729.
[9] F. Llovell, A. Galindo, F.J. Blas, G. Jackson, J. Chem. Phys. 133 (2010) 024704.
[10] G. DECHEMA Gesellschaft fur Chemische Technik und Biotechnologie e.V., Frankfurt am Main, Dechema gesellschaft fur chemische technik und biotechnologie e.v., frankfurt am main, germany, http://i-systems. dechema. de/detherm/mixture.php/ (2021).
[11] M. Glaser, C.J. Peters, H.J. van der Kooi, R.N. Lichtenthaler, J. Chem. Thermodyn. 17 (1985) 803.
[12] M.P.W.M. Rijkers, M. Malais, C.J. Peters, J. de Swaan Arons, Fluid Phase Equilib. 71 (1992) 143.
[13] M.P.W.M. Rijkers, V.B. Maduro, C.J. Peters, J. de Swaan Arons, Fluid Phase Equilib. 72 (1992) 309.
[14] V.V. de Leeuw, T.W. de Loos, H.A. Kooijman, J. de Swaan Arons, Fluid Phase Equilib. 73 (1992) 285.
[15] M.P.W.M. Rijkers, C.J. Peters, J. de Swaan Arons, Fluid Phase Equilib. 85 (1993) 335.
[16] H.H. Reamer, R.H. Olds, B.H. Sage, W.N. Lacey, Ind. Eng. Chem. 34 (1942) 1526.
[17] G.L. Stegemeier, B.F. Pennington, E.B. Brauer, E.W. Hough, SPE J. 000 (1962) 257.
[18] J.D. van der Waals, Zeit. Phys. Chem. 13 (1893) 657.
[19] H.T. Davis, L.E. Scriven, Adv. Chem. Phys. 49 (1982) 357.
[20] J.S. Rowlinson, B. Widom, Molecular Theory of Capillarity, Oxford University Press, 1998.
[21] T. Lafitte, A. Apostolakou, C. Avendaño, A. Galindo, C.S. Adjiman, E.A. Müller, G. Jackson, J. Chem. Phys. 139 (2013) 154504.
[22] E.A. Müller, G. Jackson, Annu. Rev. Chem. Biomol. Eng. 5 (2014) 405.
[23] A. Mejía, M. Cartes, H. Segura, E.A. Müller, J. Chem. Eng. Data 59 (2014) 2928.
[24] H. Cárdenas, A. Mejía, Mol. Phys. 114 (2016) 2627.
[25] J.M. Garrido, M. Cartes, H. Segura, A. Mejía, J. Supercrit. Fluids 129 (2017) 83.
[26] E.A. Müller, A. Mejía, Langmuir 33 (2017) 11518.
[27] G. Alonso, G. Chaparro, M. Cartes, E.A. Müller, A. Mejía, Molecules 25 (2020) 1499.
[28] A. Mejía, J. Pàmies, D. Duque, H. Segura, L.F. Vega, J. Chem. Phys. 123 (2005) 034505.
[29] A. Mejía, L.F. Vega, J. Chem. Phys. 124 (2006) 2445051.
[30] S. Stephan, K. Langenbach, H. Hasse, J. Chem. Phys. 150 (2019) 174704.
[31] S. Stephan, H. Hasse, Phys. Chem. Chem. Phys 22 (2020) 12544.
[32] I.I.I. Alkhatib, L.F. Vega, J. Chem. Phys. 154 (2021) 164503.
[33] V. Diky, R.D. Chirico, M. Frenkel, A. Bazyleva, J.W. Magee, E. Paulechka, A. Kazakov, E.W. Lemmon, C.D. Muzny, A.Y. Smolyanitsky, S. Townsend, K. Kroenlein, Thermo Data Engine (TDE) version 10.1 (Pure compounds, Binary mixtures, Ternary mixtures and Chemical reactions), in: NIST Standard Reference Database 103b. Thermodynamics Research Center (TRC) (Applied Chemicals and Material Division. Standard Reference Data Program, National Institute of Standards and Technology (NIST), 2016.
[34] A. Goodwin, K.N. Marsh, W.A. Wakeham, Measurement of the Thermodynamic Properties of Single Phases, Elsevier, 2003.
[35] M. Cartes, G. Chaparro, A. Mejía, J. Chem. Eng. Data 65 (2020) 3344.
[36] J.M. Garrido, L. Cifuentes, M. Cartes, H. Segura, A. Mejía, J. Supercrit. Fluids 89 (2014) 78.
[37] C. Cumicheo, M. Cartes, H. Segura, E.A. Müller, A. Mejía, Fluid Phase Equilib. 380 (2014) 82.
[38] C. Cumicheo, M. Cartes, E.A. Müller, A. Mejía, Fuel 228 (2018) 92.
[39] J. Algaba, J.M. Garrido, J.M. Míguez, A. Mejía, I. Moreno-Ventas Bravo, F.J. Blas, J. Phys. Chem. C 122 (2018) 16142.
[40] J.M. Garrido, M. Cartes, A. Mejía, J. Algaba, J.M. Míguez, I. Moreno-Ventas Bravo, M.M. Piñeiro, F.J. Blas, J. Supercrit. Fluids 128 (2017) 359.
[41] J.M. Andreas, E.A. Hauser, W.B. Tucker, J. Chem. Phys. 42 (1938) 1001.
[42] A.I. Rusanov, V.A. Prokhorov, Interfacial Tensiometry, Elsevier, 1996.
[43] M.J.B. Evans, in Measurement of the Thermodynamic Properties of Multiple Phases, edited by R.D. Weir and T.W. de Loos (Elsevier, 2006).
[44] B. Taylor and C.E. Kuyatt, NIST (1994).
[45] W.L. Masterton, J. Blanchi, J. Slowinski, E.J., J. Chem. Phys. 67 (1962) 615.
[46] G. Mie, Ann. Phys. 316 (1903) 657.
[47] A. Mejía, C. Herdes, E.A. Müller, Ind. Eng. Chem. Res. 53 (2014) 4131.
[48] A. Mejía Ervik, E.A. Müller, J. Chem. Inf. Model 56 (2016) 1609.
[49] A. Mejía, E.A. Müller, G. Chaparro, J. Chem. Inf. Model 61 (2021) 1244.
[50] M.L. Michelsen and J.M. Mollerup, Thermodynamic Models: Fundamentals and Computational Aspects (Tie-Line Publications, 2007).
[51] J.M. Beaudoin, J.P. Kohn, J. Chem. Eng. Data 12 (1967) 189.
[52] S. Srivastan, N.A. Darwish, K.A.M. Gasem, R.L. Robinson Jr., J. Chem. Eng. Data 37 (1992) 516.

[53] H. Nourozieh, M. Kariznovi, J. Abedi, Fluid Phase Equilib. 318 (2012) 96.
[54] J.M. Garrido, M.M. Piñeiro, F.J. Blas, E.A. Müller, A. Mejía, AIChE J. 62 (2016) 1781.
[55] M.M. Telo da Gama, R. Evans, Mol. Phys. 48 (1983) 229.
[56] E.A. Müller,. Ervik, and A. Mejía, Living J. Comp. Mol. Sci. 2, 21385 (2021).
[57] D. van der Spoel, E. Lindahl, B. Hess, G. Groenhof, A.E. Mark, H.J. Berendsen, J. Comput. Chem. 26 (2005) 1701.
[58] M.P. Allen, D.J. Tildesley, Computer Simulation of Liquids, 2nd ed., Oxford University Press, 2017.
[59] J.N. Jaubert, F. Mutelet, Fluid Phase Equilib. 224 (2004) 285.
[60] S. Rahman, O. Lobanova, G. Jiménez-Serratos, C. Braga, V. Raptis, E.A. Müller, G. Jackson, C. Avendaño, A. Galindo, J. Phys. Chem. B 122 (2018) 9161.
[61] B.H. Sage, H.M. Lavender, W.N. Lacey, Ind. Eng. Chem. 32 (1940) 743.
[62] S. Becker, S. Werth, M. Horsch, K. Langenbach, H. Hasse, Fluid Phase Equilib. 427 (2016) 476.
[63] A. Aasen, M. Hammer, E.A. Müller, Ø. Wilhelmsen, J. Chem. Phys. 152 (2020) 074507.
[64] L. Zheng, F. Bresme, J.P. Martin Trusler, E.A. Müller, J. Chem. Eng. Data 65 (2020) 1159.

PCCP

ROYAL SOCIETY OF CHEMISTRY

PAPER

View Article Online
View Journal

Cite this: DOI: 10.1039/c9cp06397h

Vapour–liquid phase equilibria and interfacial properties of fatty acid methyl esters from molecular dynamics simulations

Esther Feria,[a] Jesús Algaba,[a] José Manuel Míguez,[a] Andrés Mejía,[b] Paula Gómez-Álvarez[a] and Felipe J. Blas *[a]

We have determined the phase equilibria and interfacial properties of a methyl ester homologous series (from methyl acetate to methyl heptanoate) using direct simulations of the vapour–liquid interfaces. The methyl esters are modelled using the united atom approach in combination with transferable parameters for phase equilibria (TraPPE) force fields for alkanes, alkenes, carbon dioxide, ethers, and carboxylic acids in a transferable way. This allows us to take into account explicitly both dispersive and coulombic interactions, as well as the repulsive Pauli-exclusion interactions. Simulations are performed in the *NVT* or canonical ensemble using molecular dynamics. Vapour–liquid surface tension is determined using the virial route, *i.e.*, evaluating the normal and tangential components of the pressure tensor along the simulation box. We have also calculated density profiles, coexistence densities, vapour pressures, surface entropies and enthalpies, and interfacial thickness as functions of temperature, as well as the normal boiling temperatures and the critical temperatures, densities, and pressures for each member of the series. Special attention is paid to the comparison between experimental data taken from the literature and our results obtained using molecular dynamics simulations. We also analyze the effect of increasing the molecular weight of the methyl esters (at fixed temperature) on all the properties considered, with special emphasis on phase equilibria envelopes and surface tension. The TraPPE force fields transferred from other molecules and chemical families are able to predict very accurately the experimental vapour–liquid phase envelopes of methyl esters. We also compare the results obtained from simulations of the surface tension, with experimental data taken from the literature. To our knowledge, this is the first time that vapour–liquid phase equilibria and interfacial properties, and particularly surface tension, of this methyl ester homologous series are obtained using computer simulation.

Received 26th November 2019,
Accepted 8th February 2020

DOI: 10.1039/c9cp06397h

rsc.li/pccp

1 Introduction

Current environmental regulations and energy directives recommend and promote an increase, of at least 10%, the use of renewable fuels for transport by 2020, and also to dramatically reduce the transportation emission levels by 2030.[1] These initiatives have been motivated to reduce greenhouse gas emissions, where transportation contributes 34% of the total emissions. One of the most ground-breaking alternatives to accomplish these targets is to replace (partially or totally) fossil-fuels with biofuels (fuels produced from natural renewable sources), where one of the most recently emerging biofuels is biodiesel. Biodiesels are considered to be the third (or fourth) generation of biofuels[2] as they are renewable, biodegradable, non-toxic, produce less carbon dioxide than fossil fuels, and also they can replace petroleum diesel and be used either in their neat form or blended with fossil diesel inside of compression ignition engines without any extensive engine modification. In general terms, biodiesel can be obtained from a group of mono-alkyl esters[3] that, depending on the alcohol (methanol or ethanol) used for the transesterification process, become fatty acid methyl esters (FAMEs) or fatty acid ethyl esters (FAEEs), respectively. From a technical viewpoint, the use of FAMEs as a fuel is more developed than FAEEs[4,5] for efficient use.

Despite the novel use of FAMEs as diesel fuel, systematic research concerning the characterization of interfacial properties (*e.g.*, the interfacial concentration of species, the interfacial thickness, the superficial enthalpy and entropy, and surface or interfacial tension) of pure FAMEs and mixtures containing FAMEs is very limited. For the case of pure short chain FAMEs

[a] *Laboratorio de Simulación Molecular y Química Computacional, CIQSO-Centro de Investigación en Química Sostenible and Departamento de Ciencias Integradas, Universidad de Huelva, 21007 Huelva, Spain. E-mail: felipe@uhu.es*
[b] *Departamento de Ingeniería Química, Universidad de Concepción, POB 160-C Concepción, Chile*

(*i.e.*, from methyl acetate to methyl heptanoate), the available experimental data for interfacial tensions reported in DECHEMA[6] and Landolt–Börnstein[7–9] databases and also the DIRPP[10] and NIST data,[11] only cover a narrow temperature range (273 K to 360 K). Theoretical models, such as the square gradient theory,[12] need the experimental data of interfacial tensions to fit their parameters and use them as a models to predict the other interfacial properties. In the case of mixtures, the scenario is even worse, especially for the case of mixtures of hydrocarbons or aromatics with FAMEs, where interfacial properties are unexplored and only very sparse data can be found. The only exception is the case of water and FAMEs mixtures, where both experimental determinations and theoretical modelling have been carried out.[13] Therefore, considering the environmental regulations and energy directives, it is necessary to carry out systematic exploration of the interfacial behavior of the compounds involved in biodiesel production. These properties are the key requirement for their future use as a fuel, as well as for environmental issues, such as the removal of contaminants from water and for groundwater remediation.[14,15] Consequently, this work has focused on the determination of some selected interfacial properties for the case of pure short-chain FAMEs from methyl acetate to methyl heptanoate.

Due to the lack of predictive theories, molecular dynamics (MD) simulations can be used as a predictive tool to explore both bulk properties (*i.e.*, coexistence density curve, T–ρ, and vapour pressure or Clapeyron curve, P–T) and interfacial properties (*e.g.*, interfacial concentration of species, the interfacial thickness, the superficial enthalpy and entropy, and surface or interfacial tension) from low temperature to near the critical point.

In the last few decades, computer simulation has become an essential tool for modelling and predicting thermodynamic properties, including phase equilibria and interfacial properties, of complex systems of fundamental and applied interest. In particular, during the last twenty years, remarkable progress has been made in the development of new force fields for describing complex molecules from a molecular perspective. Perhaps, the most relevant example of this kind of force field is the transferable parameters for phase equilibria (TraPPE) approach of Siepmann and coworkers, that allows the determination, with high accuracy, thermodynamic and structural properties of complex molecules. The key idea behind the TraPPE models is transferability, *i.e.*, to predict the behaviour of a given molecule or set of molecules only from the knowledge of molecular parameters for particular chemical groups taken from other systems and unchanged, regardless of the atomic makeup of the rest of the molecule. This strategy allows us to truly predict the thermodynamic and other structural and dynamical properties, without the need of adjustments to experimental data of the system under study.

In this work, we use the united-atoms (UA) version of the TraPPE approach (TraPPE-UA) to predict the phase behaviour and interfacial properties of FAMEs. As mentioned in the previous paragraph, it should be possible to obtain new molecular parameter values according to the TraPPE-UA force fields by fitting them to experimental vapour–liquid phase equilibria. However, following Kamath *et al.*,[16] it is also possible to use the parameter values from the TraPPE-UA database for chemical groups that describe different molecules, including alkane and alkenes, carbon dioxide, ethers, and carboxylic acids, and transfer them to predict the phase equilibria and interfacial properties of the first members of the methyl esters chemical family. The main goal of this work is to use the transferable molecular parameters of the TraPPE-UA force field to predict the phase equilibria and interfacial properties of the first members of linear methyl esters using MD simulations. In particular, we use the direct coexistence technique in the *NVT* or canonical ensemble. The results obtained from the MD simulations are compared with experimental data taken from the literature[11] to critically assess the models' ability. To our knowledge, this is the first time that the vapour–liquid interfacial properties, and particularly the surface tension, of the first members of the methyl esters chemical family are determined using computer simulations.

The organization of this paper starts with the description of the molecular models in Section 2. In the next section, Section 3, simulation details are provided and explained briefly. In Section 4, the main interfacial property results are presented and discussed. Finally, the main conclusions are summarized in the last section.

2 Molecular models

As we have mentioned, methyl esters have been modelled following the united-atom approach. In all cases, the force fields use the Lennard-Jones (LJ) and Coulomb potentials to describe the non-bonded interactions,

$$U(r_{ij}) = 4\varepsilon_{ij}\left[\left(\frac{\sigma_{ij}}{r_{ij}}\right)^{12} - \left(\frac{\sigma_{ij}}{r_{ij}}\right)^{6}\right] + \frac{q_i q_j}{4\pi\varepsilon_0 r_{ij}} \qquad (1)$$

where r_{ij} is the distance between interacting sites i and j, σ_{ij} and ε_{ij} are the diameter and well depth associated with the LJ intermolecular potential, q_i and q_j are the partial charges on interacting sites i and j, and ε_0 the permittivity of vacuum. All the LJ parameters for unlike interactions are obtained using the Lorentz–Berthelot combining rules.

According to the TraPPE-UA philosophy, molecular parameters are taken from existing parameterizations and combined to form the molecules of interest, as has been explained in the previous section. Molecular parameters for non-bonded interactions for the carbonyl chemical group (C═O) are taken from molecular parameters of two different molecules: the parameters of the carbonyl oxygen are taken from the oxygen parameters of the carbon dioxide model proposed by Potoff and Siepmann;[17] and the parameters of the carbonyl carbon are taken from the carbon parameters of the carboxylic acid models proposed by Kamath *et al.*[18] The molecular parameters involved in the methoxy chemical group (or terminal methyl group bonded to the ether oxygen, –O–CH_3), *i.e.*, the ether oxygen and the methyl group CH_3 (sp^2), are taken from the work of Stubbs *et al.*[19]

Table 1 Well depth, ε, size, σ, and partial charge, q, parameters for the TraPPE-UA force field corresponding to non-bonded interactions of methyl-esters (from methyl acetate to methyl heptanoate). The letters in parentheses indicate the atom a particular site is bonded to. All values are taken from the work of Siepmann and co-workers[17–20]

Atom	ε/k_B (K)	σ (Å)	q (e)
CH_3–(O)	98.0	3.75	0.25
–O–	55.0	2.80	−0.40
C═(O)	41.0	3.90	0.55
O═(C)	79.0	3.05	−0.45
CH_3–(C)	98.0	3.75	0.05
CH_2–(C)	46.0	3.95	0.05
CH_3–(CH_x)	98.0	3.75	0.00
CH_2–(CH_x)	46.0	3.95	0.00

The molecular parameters of methyl (CH_3– not bonded to the oxygen ether) and methylene (–CH_2– not bonded to the carbon –C– atom) groups are taken from the TraPPE-UA parameter values of alkanes proposed by Martin and Siepmann.[20] It is interesting to mention that Maerzke *et al.*[21] considered TraPPE force fields for acrylates and methacrylates that share some of the same UA as the FAMEs studied in this work. However, these substances contain conjugated double bonds. In our work, we consider methyl esters that do not contain this kind of bond, and therefore use the TraPPE molecular parameters of Kamath *et al.*[18] and Stubbs *et al.*[19] All the molecular parameters used in this work to describe the non-bonded interactions, including the partial charge values for electrostatic interactions of all the chemical groups, are summarized in Table 1.

As in the case of the LJ parameters and partial charges, bond lengths, bending, and torsional force field parameters characterizing the bonded interactions are obtained from the TraPPE-UA values of different chemical groups. Tables 2–4 show all the parameter values used in this work. Note that according to the usual TraPPE-UA force field approach, the bond lengths between different chemical groups are fixed.

3 Simulation details

All MD simulations are carried out in conditions at which the vapour–liquid interface is present, following the standard methodology[22,23] for all models studied. In particular, simulations are performed in the *NVT* canonical ensemble using GROMACS (version 4.6.1)[24] at a fixed temperature T, in a parallelepipedic simulation cell of constant volume $V = L_x \times L_y \times L_z$, where L_x, L_y, and L_z are the dimensions of the simulation box. We use periodic boundary conditions in all three directions.

Table 2 Bond length values for the TraPPE-UA force field corresponding to methyl-esters (from methyl acetate to methyl heptanoate). All values are taken from the TraPPE approach

Bond	Bond length (Å)
C═O	1.200
C–O	1.344
CH_3–O	1.410
CH_x–C	1.520
CH_2–CH_x	1.540

Table 3 Bending potential parameters for the TraPPE-UA force field corresponding to methyl-esters (from methyl acetate to methyl heptanoate). All values are taken from the TraPPE approach

Bending	θ (deg)	k_0/k_B (K rad^{-2})
CH_3–O–C	115	62 500
O–C═O	125	62 500
O–C–CH_3	110	70 596
O═C–CH_3	125	62 500
O═C–CH_2	125	62 500
C–CH_2–CH_2	114	62 500
CH_2–CH_2–CH_2	114	62 500
CH_2–CH_2–CH_3	114	62 500

Table 4 Torsional potential parameters for the TraPPE-UA force field corresponding to methyl-esters (from methyl acetate to methyl heptanoate). All values are taken from the TraPPE approach

Torsion	c_0/k_B (K)	c_1/k_B (K)	c_2/k_B (K)	c_3/k_B (K)
CH_3–O–C═O	11594.6	3374.2	−4118	−613.6
CH_3–O–C–CH_3	6551.3	1566.1	−4196	789.2
CH_3–O–C–CH_2	6551.3	1566.1	−4196	789.2
O–C–CH_2–CH_2	839.87	−2133.17	106.68	3097.72
O–C–CH_2–CH_3	839.87	−2133.17	106.68	3097.72
O═C–CH_2–CH_2	1121.13	142.79	−115.68	−1172.92
O═C–CH_2–CH_3	1121.13	142.79	−115.68	−1172.92
C–CH_2–CH_2–CH_2	1009.97	−2018.93	136.38	3165.28
C–CH_2–CH_2–CH_3	1009.97	−2018.93	136.38	3165.28
CH_2–CH_2–CH_2–CH_2	1009.97	−2018.93	136.38	3165.28
CH_2–CH_2–CH_2–CH_3	1009.97	−2018.93	136.38	3165.28

A homogeneous liquid system is first equilibrated in a parallelepiped simulation box. The dimensions of the box are $L_x = L_y = 3.9$ nm for the case of methyl acetate and $L_x = L_y = 3.95$ nm for the rest of methyl esters. For the lengths of the simulation boxes along the z-axis we have used the following sizes: $L_z = 11$ nm (methyl acetate), $L_z = 13$ nm (methyl propionate), $L_z = 16$ nm (methyl butyrate), $L_z = 19$ nm (methyl valerate), $L_z = 20$ nm (methyl hexanoate), and $L_z = 23$ nm (methyl heptanoate). We consider $N = 1100$ molecules for all the methyl esters studied in this work. After equilibration of these bulk-liquid systems, the box is expanded along the z-direction leaving the liquid phase slab at the center. The final overall dimensions of the vapour–liquid–vapour configuration box are therefore $L_x = L_y = 3.9$ nm and $L_z = 33$ nm for the case of methyl acetate, and $L_x = L_y = 3.95$ nm and $L_z = 39$, 48, 57, 60, and 69 nm for the methyl propionate, methyl butyrate, methyl valerate, methyl hexanoate, and methyl heptanoate, respectively.

In order to reduce the truncation and system size effects involved in the phase equilibrium and interfacial properties calculations, the cut-off radius (r_c) has been taken to be equal to a value of 5σ ($r_c = 1.95$ nm for methyl acetate and 1.975 nm for the rest of the methyl esters). It has been shown by several authors[25–27] that such a value provides a reasonable description for the interfacial properties. Long-range interactions are determined using the three-dimensional Ewald technique with a convergence parameter of 0.1 Å^{-1} and a maximum value for the reciprocal lattice equal to 31.

We have used the Verlet leapfrog[28] algorithm with a time step of 0.001 ps. It is important to note in this case that the time step value chosen has been necessary to sample correctly the torsional potentials of the ester models. A Nosé–Hoover thermostat[29] with large time constant equal to 1.0 ps has been used. Simulations of the homogeneous liquid systems are equilibrated during 5 ns. After this, the vapour–liquid–vapour systems are also equilibrated during 5 ns. After the systems reach equilibrium, the properties of the coexisting vapour and liquid phases are obtained as appropriate averages during 20 ns. In order to estimate errors on the variables computed, the sub-blocks average method was applied.[30] In such approach, the production period is divided into M independent blocks. The statistical error is then deduced from the standard deviation of the average $\bar{\sigma}/\sqrt{M}$, where $\bar{\sigma}$ is the variance of the block averages and M has been fixed in this work to $M = 10$.

The equilibrium vapour pressure, P, and interfacial tension, γ, are obtained from the diagonal components of the pressure tensor. The vapour pressure corresponds to the normal component, $P \equiv P_{zz}$, of the pressure tensor, while the interfacial tension is obtained using the mechanical route:[31–34]

$$\gamma = \frac{L_z}{2}\left[P_{zz}(z) - \frac{P_{xx}(z) + P_{yy}(z)}{2}\right] \quad (2)$$

In eqn (2), the additional factor 1/2 comes from having two interfaces in the system, and L_z is the size of the simulation box in the z direction, defined along the longitudinal dimension across the interface.

The experimental determination of the critical state of FAMEs is extremely difficult due to their thermal instability. One alternative route to obtain the critical coordinates, *i.e.*, critical pressure, P_c, temperature, T_c, and density, ρ_c, is to use the vapour–liquid equilibrium MD results together the scaling law[35,36] given by:

$$\rho_L - \rho_V = A(T - T_c)^{\beta} \quad (3)$$

and the corresponding law of rectilinear diameters

$$\frac{\rho_L + \rho_V}{2} = \rho_c + B(T - T_c) \quad (4)$$

β is the corresponding critical exponent,[32] with a universal value of $\beta = 0.325$, and A, B, T_c and ρ_c are four unknown constants obtained by fitting to the simulation results. ρ_L and ρ_V are the liquid and vapour coexistence densities at the corresponding temperature T, respectively. Critical temperature, T_c, and density, ρ_c, can be easily obtained from eqn (3) and (4).

An independent way to calculate T_c is to apply an alternative scaling law using interfacial information from the system.[37,38] Following this route, γ is related to T_c by the following expression:

$$\gamma = \gamma_0(1 - T/T_c)^{\mu} \quad (5)$$

where γ_0 is the so-called ''zero-temperature'' surface tension and μ is the corresponding critical exponent. Here, we fix μ to the universal value $\mu = 1.258$ as obtained from renormalization-group theory.[32] Once again, the unknown constants, γ_0 and T_c are found by fitting the interfacial tension data with temperature.

The critical pressure can be estimated from an extrapolation of the Clausius–Clapeyron relation to the critical temperature obtained from eqn (3) or (5):

$$\ln P = C_1 + \frac{C_2}{T} \quad (6)$$

where C_1, and C_2 are correlation parameters. The value of P_c is obtained using eqn (6) at $T = T_c$. The critical temperature value, T_c, used in the previous equation is obtained from eqn (3).

The surface entropy (Δs^{γ}) and surface enthalpy (Δh^{γ}) change of surface formation can be also determined using the temperature dependence of the surface tension from the following derivative expressions:[32,39]

$$\Delta s^{\gamma} = -\left(\frac{\partial \gamma}{\partial T}\right)_P \quad (7)$$

$$\Delta h^{\gamma} = \gamma + T\Delta s^{\gamma} \quad (8)$$

Finally, an interesting property that can be obtained from the calculation of density profiles is the interfacial width along the vapour–liquid equilibrium. Implicitly this property is defined by fitting the curves from the original mean field van der Waals theory,[32] described by

$$\rho(z) = \frac{\rho_L + \rho_V}{2} - \frac{\rho_L - \rho_V}{2}\tanh\left[\frac{\alpha(z - z_0)}{d}\right] \quad (9)$$

where the constant $\alpha = 2\tanh^{-1}(0.8)$ is chosen so that d is the 10–90 interfacial thickness and z_0 the position of the Gibbs dividing surface. If coexistence densities are calculated first (see the next section for further details), d and z_0 could be treated as adjustable parameters in eqn (9). Since two interfaces are simulated simultaneously during each simulation, it is possible to compare the interfacial thickness values obtained from both interfaces. In this work, the values determined are always found to be the same within statistical uncertainty, indicating that the inhomogeneous systems are properly equilibrated at all temperatures.

4 Results and discussion

In this section we present the main results from the simulations of the six methyl esters using the TraPPE-UA molecular models described in the previous sections. We focus on the interfacial properties, such as density profiles, interfacial thickness, surface entropy and enthalpy, and surface tension. We also examine the temperature dependence of these properties, and compare our results for the different models with experimental data taken from the literature.[11]

We analyze the thermodynamic and interfacial behavior of all the FAMEs at different temperatures using the same methodology as in our previous work.[40–46] Density profiles are calculated by dividing the system into 200 slabs along the z-direction. The molecular density profiles, $\rho_i(z)$, are obtained

by assigning the position of each united atom center, z_i, to the corresponding slab and constructing the molecular density from mass balance considerations. The bulk vapour and liquid densities in each system are calculated by averaging $\rho_i(z)$ over appropriate regions sufficiently removed from the interfacial region. In addition to that, the final bulk vapour density value, at each temperature and chain length, is obtained after averaging the density profiles on both sides of the liquid film.

We show in Fig. 1 the density profiles $\rho(z)$ for the six methyl esters considered in this work, from methyl acetate up to methyl heptanoate, at different temperatures as modelled using the TraPPE-UA models. For the sake of clarity, we only present half of the profiles corresponding to one of the interfaces. Also for convenience, all density profiles have been shifted to place z_0 at the origin.

As can be seen, liquid density decreases and vapour density increases as the temperature is increased in all cases, as expected. The slope of each density profile, in absolute values, along the interfacial region becomes smaller as the temperature approaches the critical point for each system. According to the near-critical scaling laws,[32] the interfacial thickness must diverge as the temperature approaches the critical temperature. The results presented in Fig. 1 corroborate this behaviour.

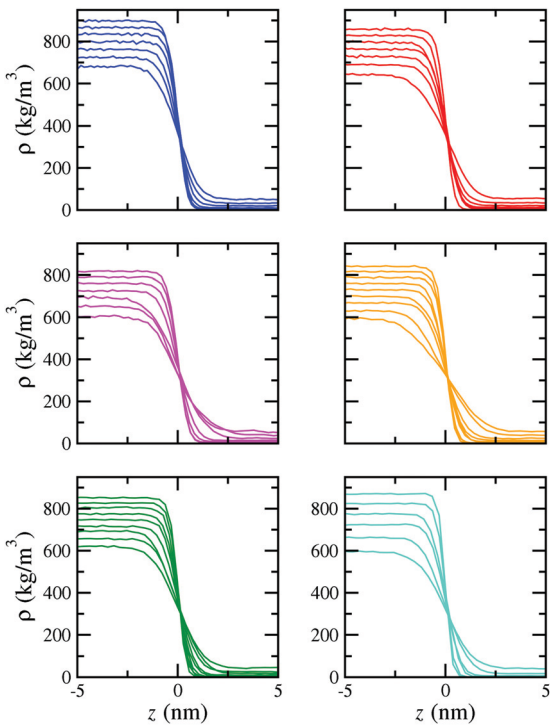

Fig. 1 Simulated equilibrium density profiles across the vapour–liquid interface of methyl esters as obtained from MD *NVT* simulations using the TraPPE-UA models for methyl acetate (blue curves), methyl propionate (red curves), methyl butyrate (magenta curves), methyl pentanoate (orange curves), methyl hexanoate (green curves), and methyl heptanoate (turquoise curves) at different temperatures. From the bottom to the top (in the liquid region): 300, 325, 350, 375, 400, 425, 450, 475, 500, 525, and 550 K.

From the density profiles depicted in Fig. 1, it is possible to obtain the vapour–liquid phase envelopes of the different FAMEs studied in this work. Results corresponding to the vapour and liquid coexistence densities, at different temperatures, are presented in Table 5. Fig. 2 shows the phase diagrams of all the systems considered as obtained from MD computer simulations. Experimental data taken from the literature[11] is also included for comparison. In general, computer simulations are able to predict very accurately the vapour and liquid

Table 5 Liquid density ρ_L, vapour density ρ_V, vapour pressure P, compressibility factor Z, and surface tension γ at different temperatures, as obtained from MD *NVT* simulations for methyl esters (from methyl acetate to methyl heptanoate). The errors are estimated as explained in the text

T (K)	ρ_L (kg m^{-3})	ρ_V (kg m^{-3})	P (MPa)	Z	γ (mN m^{-1})
Methyl acetate					
300	897(3)	1.2(1)	0.041(3)	1.06 (1)	—
325	867(3)	3.3(2)	0.114(7)	0.946(2)	22.3(3)
350	835(3)	6.5(3)	0.231(8)	0.90(1)	18.4(2)
375	800(4)	10.7(5)	0.42(1)	0.93(2)	15.4(3)
400	763(3)	20.0(6)	0.78(1)	0.86(1)	12.0(4)
425	722(8)	32.0(7)	1.26(2)	0.821(7)	9.0(5)
450	679(4)	51(1)	1.92(1)	0.75(1)	6.4(2)
Methyl propionate					
325	858(2)	1.8(2)	0.06(3)	1.07(4)	21.7(3)
350	828(2)	3.6(2)	0.111(4)	0.94(2)	19.2(2)
375	797(3)	7.2(0.4)	0.233(9)	0.91(2)	15.7(6)
400	765(3)	12.8(5)	0.45(1)	0.93(2)	12.2(3)
425	729(3)	21.1(6)	0.726(9)	0.86(1)	9.9(3)
450	687(4)	34.7(7)	1.16(1)	0.788(8)	8.1(3)
475	643(3)	54(1)	1.78(3)	0.733(3)	5.1(3)
Methyl butyrate					
350	818(4)	2.0(3)	0.063(5)	1.10(8)	19.0(3)
375	790(2)	4.8(3)	0.140(6)	0.95(2)	16.1(4)
400	759(3)	8.9(5)	0.267(5)	0.92(3)	13.4(4)
425	726(3)	15.3(5)	0.472(8)	0.89(1)	10.6(3)
450	694(4)	26(1)	0.77(1)	0.81(1)	8.0(2)
475	653(3)	39.3(1)	1.14(2)	0.751(8)	6.2(2)
500	608(5)	54(2)	1.64(2)	0.75(8)	4.1(4)
Methyl valerate					
375	789(3)	2.5(3)	0.066(5)	0.98(4)	16.7(4)
400	761(3)	5.1(4)	0.134(6)	0.92(3)	14.3(4)
425	731(2)	9.4(3)	0.27(1)	0.928(9)	12.1(3)
450	701(2)	15.1(6)	0.42(1)	0.858(9)	10.0(3)
475	670(2)	24.0(5)	0.70(1)	0.860(6)	8.1(5)
500	630(3)	37.8(1)	1.06(2)	0.782(8)	5.8(5)
525	589(4)	56.9(2)	1.52(3)	0.710(5)	4.0(4)
Methyl hexanoate					
375	802(3)	1.7(2)	0.037(4)	0.92(3)	17.7(5)
400	775(2)	2.9(2)	0.073(5)	0.984(4)	15.4(5)
425	748(2)	5.9(3)	0.152(6)	0.95(1)	13.5(4)
450	719(4)	9.7(5)	0.26(1)	0.935(9)	11.3(3)
475	690(4)	17.6(5)	0.47(1)	0.873(2)	9.8(3)
500	657(3)	26.5(8)	0.68(1)	0.80(1)	7.3(3)
525	621(2)	43(1)	1.07(2)	0.742(7)	5.1(4)
Methyl heptanoate					
300	870(2)	0.02(1)	—	—	25.1(8)
350	824(2)	0.36(4)	—	—	21.1(8)
400	775(2)	2.2(2)	0.046(5)	0.993(4)	16.1(6)
450	722(2)	6.1(4)	0.15(1)	1.06(1)	11.8(4)
500	663(2)	17.4(6)	0.43(1)	0.944(9)	9.0(3)
550	597(3)	41(1)	1.03(2)	0.869(8)	4.0(5)

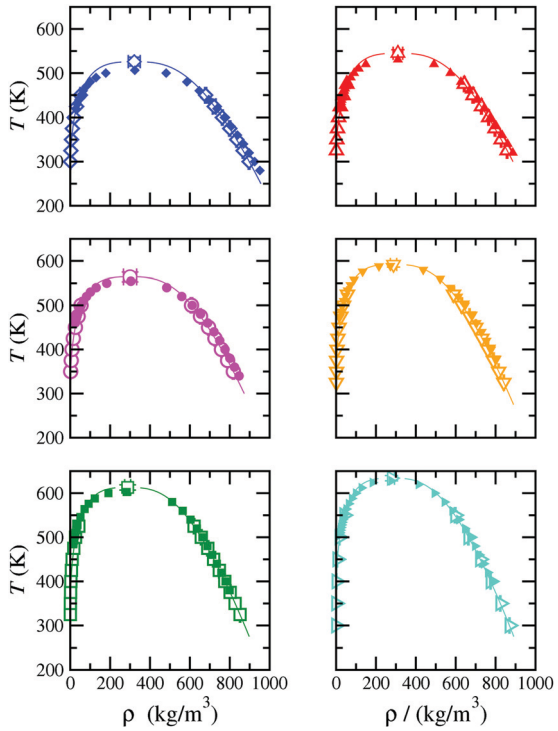

Fig. 2 Vapour–liquid coexistence densities of methyl esters. The open symbols correspond to the coexistence densities obtained from MD *NVT* simulations, and the filled symbols to the experimental data taken from the literature[11] for methyl acetate (blue diamonds), methyl propionate (red triangles up), methyl butyrate (magenta circles), methyl pentanoate (orange triangles down), methyl hexanoate (green squares), and methyl heptanoate (turquoise triangles right). The continuous curves correspond to the fits of the simulation data presented in this work using eqn (3) and (4). Symbols at the highest temperatures for each coexistence curve represent the critical points estimated from eqn (3) and (4) (filled symbols) and the experimental critical points taken from the literature[11] (open symbols).

densities in the whole range of temperatures considered, from near the triple-point to the critical temperature. Very small differences between simulation and experimental data for the liquid branch of the phase envelope can be seen at low temperatures in the case of methyl acetate, methyl propionate, and methyl butyrate.

In addition to the vapour and liquid coexistence densities, we have also determined the coordinates of the critical points of all the FAMEs from the MD simulation results using the scaling laws given by eqn (3) and (4). In particular, we follow the methodology explained in the previous section. As in the case of the vapour and liquid coexistence densities, we compare our results obtained from the analysis described above with experimental data taken from the literature.[11] The critical temperatures and densities of all the FAMEs obtained from MD simulations are presented in Table 6. Comparison between simulation and experimental critical coordinates can also be observed in Fig. 2. Agreement between simulation and experiment is excellent in all cases. Computer simulation results overestimate the experimental values by less than 3% (2.7% is the case of methyl hexanoate and 0.7% in the case of methyl butyrate). Differences between the experiments and simulations could be due to finite-size scaling effects that occur during simulations when the system is close to the critical state. These effects can be taken into account explicitly using advanced simulation techniques, such as the Finite-Size Scaling procedure of Binder.[47] However, this kind of analysis is out of the scope of this work. Critical densities of the homologous chemical family are also accurately predicted by the TraPPE-UA models of FAMEs. Deviation between simulation and experiment for ρ_c values is always below 2%, except in the case of methyl valerate (5.9%). In all cases, critical densities are slightly overestimated as expected.

We have also determined the normal boiling temperature of each methyl ester. This has been done using eqn (6) with an evaluating pressure set at P = 101 325 Pa. The predictions from the simulations are shown in Table 6. Comparison between values taken from the literature and the predictions obtained from the simulations show good agreement between both results. As can be seen, in most cases the deviation is $\approx$2.2–3.8%, except in the case of methyl hexanoate, in which deviation is 4.69%, approximately.

Vapour pressure of FAMEs is also calculated from MD simulation. Since we are simulating planar vapour–liquid interfaces, the system is inhomogeneous. Consequently, the pressure is no longer a scalar magnitude but a tensorial quantity. In this case, the normal component of the pressure tensor (acting perpendicularly to the planar interface) is equal to the vapour pressure of the system. The results obtained from computer simulations are shown in Table 5. We have also presented the vapour pressure, as functions of temperature, of all the FAMEs studied in this work in Fig. 3. The predictions obtained from computer simulations provide, in general, a good description of the vapour pressure curves, particularly for methyl acetate, methyl propionate, and methyl heptanoate. As can be seen in Fig. 3, in the case of methyl butyrate, methyl valerate, and methyl hexanoate, MD simulation results overestimate the vapour pressure at mid and high temperatures. We have also represented the vapour pressure data in a Clausius–Clapeyron plot (Fig. 4). TraPPE-UA models are able to predict very accurately the vapour pressure of all the FAMEs, from methyl acetate up to methyl heptanoate, at low temperatures.

One of the main goals of this work is to predict the interfacial properties of FAMEs. Fig. 5 displays the variation of the interfacial thickness, d, as a function of temperature obtained using eqn (9) for each FAME. From this figure it is possible to observe that d increases with increasing temperature. This means that the interfacial region becomes wider as the temperature is increased. At low temperatures, the density profiles show sharp interfaces, which can be identified with low values of interfacial thickness. An increase of the temperature results in a wider interfacial region as the system approaches the critical point, and consequently, the interfacial thickness increases. As $T \rightarrow T_c$, the interfacial thickness diverges as the liquid and vapour phases become identical.

The surface entropy, Δs^{γ}, that can be obtained from the temperature derivative of the surface tension according to

Table 6 Experimental (T_c^{exp}, ρ_c^{exp}, P_c^{exp}, and T_b^{exp}) and predicted ($T_c^{\dagger}$, $T_c^{\S}$, $\rho_c^{\dagger}$, $P_c^{\dagger}$, and T_b) critical temperatures, densities, and pressures and normal boiling temperatures of methyl esters (from methyl acetate to methyl heptanoate). Critical temperatures, $T_c^{\dagger}$ and $T_c^{\S}$, are obtained from the analysis of the MD *NVT* coexistence densities using eqn (3) and (4), and the analysis of the MD *NVT* tension data using eqn (5), respectively. Critical densities, $\rho_c^{\dagger}$, are also obtained from the analysis of the MD *NVT* coexistence densities using eqn (4). Critical pressures, $P_c^{\dagger}$, are obtained using eqn (6) evaluating the temperature $T_c^{\dagger}$ as obtained from eqn (3). Normal boiling temperatures are obtained using eqn (6) at pressure P = 101 325 Pa

Substance	T_c^{exp} (K)	$T_c^{\dagger}$ (K)	$T_c^{\S}$ (K)	ρ_c^{exp} (kg m^{-3})	$\rho_c^{\dagger}$ (kg m^{-3})	P_c^{exp} (MPa)	$P_c^{\dagger}$ (MPa)	T_b^{exp} (K)	T_b (K)
Methyl acetate	510.0	523.9	525.14	324.0	321.0	4.692	6.127	322.63	330.09
Methyl propionate	531.5	543.1	550.38	310.0	310.0	3.986	4.302	340.10	352.44
Methyl butyrate	554.5	558.8	571.65	304.0	300.0	3.464	3.538	359.35	373.60
Methyl valerate	566.9	558.0	589.80	272.0	288.0	3.090	3.564	388.09	400.65
Methyl hexanoate	602.6	618.4	597.46	283.0	288.0	2.797	3.487	407.72	427.81
Methyl heptanoate	628.0	644.1	635.28	278.0	278.0	2.543	3.630	435.71	446.15

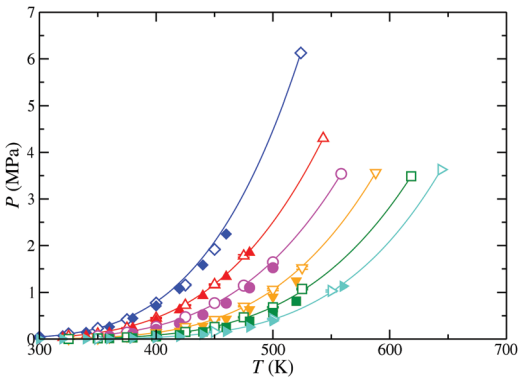

Fig. 3 Vapour pressure of methyl esters (from methyl acetate to methyl heptanoate). The meaning of the symbols is the same as in Fig. 2. The continuous curves correspond to the fits of the simulation data presented in this work to eqn (6). Filled symbols at the highest temperature for each vapour pressure curve represent the critical points obtained from eqn (6) using the critical temperature values obtained from eqn (3).

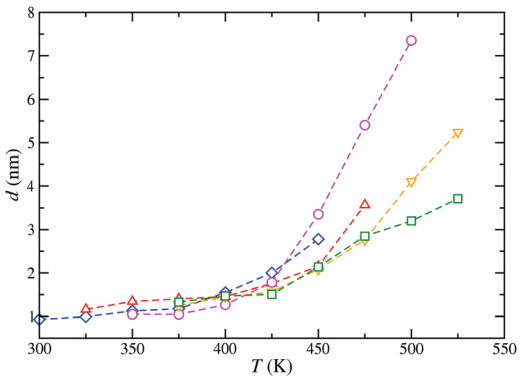

Fig. 5 10–90 interfacial thickness d as a function of the temperature for methyl esters (from methyl acetate to methyl heptanoate). The symbols correspond to the values obtained from density profiles obtained from MD *NVT* simulations and the dashed curves are included as a guide to the eye. The meaning of the symbols is the same as in Fig. 2.

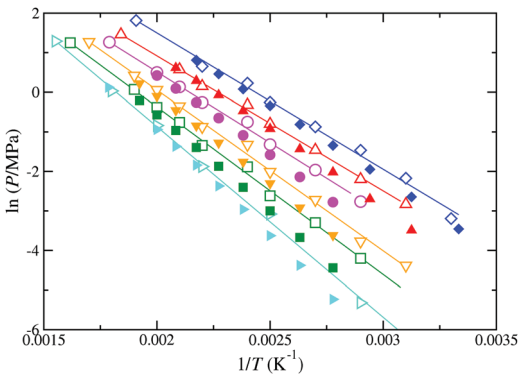

Fig. 4 Clausius–Clapeyron representation of the vapour pressure of methyl esters (from methyl acetate to methyl heptanoate). The meaning of the symbols is the same as in Fig. 2.

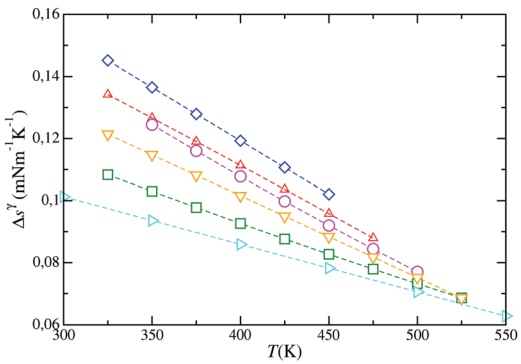

Fig. 6 Surface entropy of methyl esters (from methyl acetate to methyl heptanoate) as obtained from the combination of the MD *NVT* simulation results and eqn (7). The meaning of the symbols is the same as in Fig. 2.

eqn (7), is a useful magnitude in studies involving surfaces in which temperature, and also surface tension, is non-uniform, leading to the well-known Bénard–Marangoni convection phenomena.[48] Fig. 6 shows the surface entropy change of surface formation for FAMEs as a function of temperature. Δs^{γ} is obtained from MD computer simulations of the interfacial tension in combination with eqn (7). Δs^{γ} varies linearly with T for all the methyl esters considered here, and slightly decreases with increasing temperature. This behaviour is related to the slight curvature of the surface tension as a function of temperature (see below). In addition to this, for a fixed temperature, Δs^{γ} exhibits its largest values for short methyl esters and gets smaller as the molecular weight of the FAME increases. This indicates that curvature of surface tension, as a function of temperature, is larger for short methyl esters than

for long FAMEs. Interestingly, as the temperature increases, differences between Δs^{γ} for FAMEs becomes smaller, showing that curvature of surface tension, at high temperature, is similar for all methyl esters. This is a clear indication of the universal behaviour of $\gamma = \gamma(T)$ for different members of the homologous series as the system approaches the critical region.

It is possible to obtain the surface enthalpy, Δh^{γ}, as a function of temperature, for the FAMEs studied in this work. Similar to the case of the surface entropy, Δh^{γ} can be determined from MD simulation data of the interfacial tension using eqn (8). According to this, surface enthalpy is computed directly from surface tension values and the numerical derivative of $\gamma(T)$ with respect to the temperature. Fig. 7 shows Δh^{γ}, as a function of temperature, of the methyl esters. As can be seen, this property decreases with temperature, as expected. A nearly linear behaviour is observed for the shortest FAMEs. However, the Δh^{γ}–T plots show a certain curvature as the molecular weight is increased. At fixed temperature, the surface enthalpy decreases as the lengths of the methyl esters are increased. Although this is true at low and mid temperatures, this trend seems to change at high T.

Finally, we consider the vapour–liquid interfacial tension of methyl esters, from methyl acetate up to methyl heptanoate. Fig. 8 shows the surface tension, as a function of temperature, as obtained from MD simulations using the virial or mechanical route. According to this, the surface tension is calculated using eqn (2), *i.e.*, as the difference between the normal and tangential macroscopic components of the pressure tensor. We have also included experimental data taken from the literature[11] in order to compare the predictions from the TraPPE-UA molecular models. The simulation results obtained in this work show excellent agreement with experimental data in the temperature range at which experimental data is available ($T \lesssim 360$ K). Simulation results obtained from the use of TraPPE-UA models for methyl esters seems to slightly overestimate the surface tension at low temperatures for methyl acetate, methyl propionate, and methyl butyrate. For longer molecules, agreement between simulation and experimental data is excellent.

As in the case of the vapour–liquid phase envelopes, we have also fit the simulation data using the well-known Guggenheim's scaling law for the surface tension as a function of temperature according to eqn (5).[37,38] This allows us to obtain the critical temperature of each methyl ester and compare these values with the experimental critical values. Table 6 includes the values found in this work. It is interesting to compare the critical values obtained from eqn (3)–(5). As can be seen, critical temperatures determined using surface tension values and vapour and liquid coexistence densities are different. *A priori*, one expects that both values should be the same. However, one should take into account the following points: (1) strictly speaking, the scaling laws given by eqn (3) and (5) are only valid in the asymptotic limit $T \to T_c$; in this work, as is usual in the literature,[40,41,43,49,50] we have used data corresponding to states located at T far away from the T_c (data corresponding to temperatures around 30–40% below the critical temperature up to near the critical point); (2) the estimation of the critical coordinates depends critically on the size of the system; here we use only 1100 molecules, which in our opinion, is not enough to avoid the finite-size effects of the systems under study;[51] (3) the location of the critical coordinates depends also critically on the cutoff distance used during the simulation, and if tail corrections are applied or not. This is especially important if we are using two different kinds of properties (density and surface tension values) to obtain the critical temperature since they are affected by the truncation of the intermolecular potential in a different way, as probably happens in this work. (4) Finally, the goal of the this work is not to obtain accurate values of critical temperatures and densities of methyl esters but to check if the

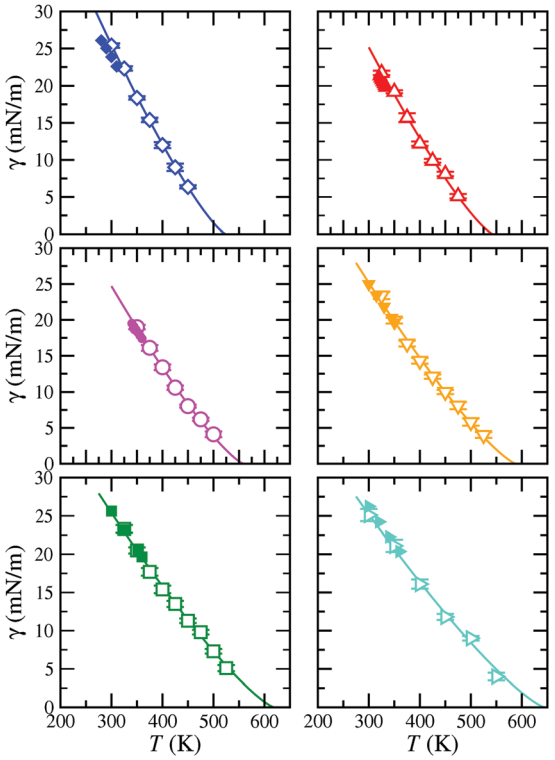

Fig. 8 Vapour–liquid surface tension as a function of temperature for methyl esters (from methyl acetate to methyl heptanoate). The meaning of the symbols is the same as in Fig. 2. The continuous curves correspond to the fits of the simulation data presented in this work to eqn (5).

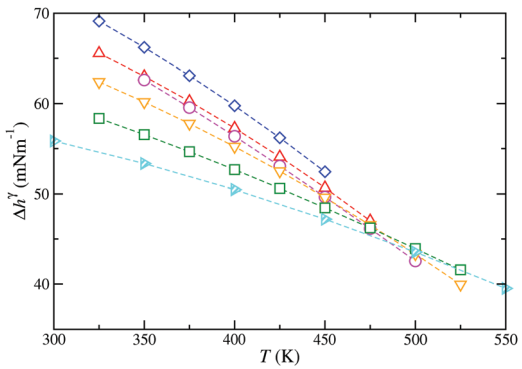

Fig. 7 Surface enthalpy of methyl esters (from methyl acetate to methyl heptanoate) as obtained from the combination of the MD *NVT* simulation results and eqn (8). The meaning of the symbols is the same as in Fig. 2.

TraPPE force field is able to predict, in a transferable manner, the phase equilibria and interfacial properties of methyl esters. We think a procedure similar to that followed by Dinpajooh *et al.*,[51] finite-size scaling[52] or mixed-field theory using the Binder cumulant parameter[53] methodologies, is the correct approach to be followed if accurate estimations of critical points are needed. Unfortunately, this is out of the scope of this work.

It is interesting to mention that the experimental data taken from the literature[11] is only available at low temperatures, from 300 up to 360 K, approximately. The reason for which there is no experimental data at higher temperatures is that methyl esters become unstable at high temperatures, generating micro bubbles in the tensiometer and densimeter, making it impossible to measure this property accurately. Fortunately, this is not the case for computer simulations. Our study allows us to obtain the surface tension of all the methyl esters analyzed in this work up to 450–550 K, depending on the critical temperature of each substance. It is important to recall that the simulated surface tension values in this work are, to the best of our knowledge, reported for the first time. This is particularly important in this case since there is no experimental data at temperatures above 360 K for any of the FAMEs studied, as just commented. The excellent agreement found, not only for surface tension at low temperatures, but also for vapour–liquid coexistence densities and vapour pressures in wide ranges of temperature, makes the TraPPE-UA models proposed and used in this work excellent candidates for predicting the phase equilibria and interfacial properties of FAMEs. The simulation data presented in this work could be used, not only for theoretical modelling of these compounds, but also for the design and use of new chemical processes involving FAMEs as future and alternative diesel fuels, as well as for environmental issues, including the removal of contaminants from water, and for groundwater remediation.

5 Conclusion

We have studied the phase equilibria and interfacial properties of a methyl esters homologous series (from methyl acetate to methyl heptanoate) using the TraPPE force fields for different molecules and chemical families in a transferable way. In particular, we use the direct coexistence technique, in combination with MD *NVT* simulations, to study inhomogeneous systems of pure esters containing two vapour–liquid interfaces.

We examine the vapour–liquid surface tension using the virial route, *i.e.*, calculating the normal and tangential components of the pressure tensor. We have also determined density profiles, coexistence densities, vapour pressures, surface entropies and enthalpies, interfacial thickness, and critical temperature, density, and pressure as functions of temperature for all the methyl esters considered. Predictions from the MD simulation for vapour–liquid coexistence densities and vapour pressures are compared with experimental data taken from the literature. These three properties are predicted remarkably well by the TraPPE models. This is particularly important since the molecular parameters of the TraPPE force fields are taken in a transferable way from other molecules and chemical families without adjustment.

We also predict the behaviour of interfacial thickness, surface entropy, and surface enthalpy, as functions of temperature, and consider the effect of increasing the molecular weight of the homologous family. Particularly interesting are the results for the surface tension of methyl esters. The TraPPE models and the molecular parameters transferred from other molecules and chemical families are able to predict very accurately the surface tension of all the methyl esters studied in this work at low temperatures. Although experimental data is only available at temperatures below 360 K, computer simulation allows us to provide surface tension up to the pure critical points of each substance. This is an important result since this is the first time the vapour–liquid surface tension of methyl esters is determined in the literature at these conditions. In fact, this is the first computer simulation work devoted to the prediction of the vapour–liquid equilibria and interfacial properties of the homologous series.

Conflicts of interest

There are no conflicts to declare.

Acknowledgements

The authors acknowledge the Centro de Supercomputación de Galicia (CESGA, Santiago de Compostela, Spain) for providing access to computing facilities, and Ministerio de Economía, Industria y Competitividad through the Grant with reference FIS2017-89361-C3-1-P co-financed by EU FEDER funds. A. M. acknowledges funding from Fondecyt (Chile) through Grant 1190107. Further financial support from Junta de Andalucía and Universidad de Huelva is also acknowledged. J. A. F. acknowledges Contrato Predoctoral de Investigación from XIX Plan Propio de Investigación de la Universidad de Huelva and an FPU Grant (Ref. FPU15/03754) from the Ministerio de Educación, Cultura y Deporte. J. A., J. M. M., P. G.-A., and F. J. B. thankfully acknowledge the computer resources at Magerit and the technical support provided by the Spanish Supercomputing Network (RES) (Project QCM-2018-2-0042).

References

1 https://ec.europa.eu/energy/en/topics/renewable-energy/renewable-energy-directive, (retrieved November, 2019).
2 M. F. Demirbar, *Appl. Energy*, 2009, **86**, S151–S161.
3 L. C. B. A. Bessa, M. C. Ferreira, C. R. A. Abreu, E. A. C. Batista and A. J. A. Meirelles, *Fluid Phase Equilib.*, 2016, **425**, 98–107.
4 N. D. D. Carareto, M. C. Costa, A. J. A. Meirelles and J. Pauly, *Fluid Phase Equilib.*, 2014, **382**, 158–163.
5 N. D. D. Carareto, C. Y. C. S. Kimura, E. C. Oliveira, M. C. Costa and A. J. A. Meirelles, *Fuel*, 2012, **96**, 319–326.

6 DECHEMA Gesellschaft Für Chemische Technik Und Biotechnologie E.V., Frankfurt Am Main, Germany, https://i-systems.dechema.de/detherm/, (retrieved November, 2019).
7 C. Wohlfarth and B. Wohlfarth, in *New Series Group IV Physical Chemistry*, ed. M. Lechner, Springer Verlag, Berlin, Heidelberg, 1997, vol. 16.
8 C. Wohlfarth and B. Wohlfarth, in *New Series Group IV Physical Chemistry*, ed. M. Lechner, Springer Verlag, Berlin, Heidelberg, 2008, vol. 24.
9 C. Wohlfarth and B. Wohlfarth, in *New Series Group IV Physical Chemistry*, ed. M. Lechner, Springer Verlag, Berlin, Heidelberg, 2016, vol. 28.
10 T. E. Daubert and R. P. Danner, *Physical and Thermodynamic Properties of Pure Chemicals. Data Compilation*, Taylor and Francis, Bristol, 1989.
11 E. W. Lemmon, M. O. McLinden, D. G. Friend, C. Wohlfarth and B. Wohlfarth, in *NIST Chemistry WebBook, NIST Standard Reference Database Number 69*, ed. P. J. Linstrom and W. G. Mallard, National Institute of Standards and Technology, Gaithersburg MD, 2019.
12 H. T. Davies and L. E. Scriven, *Adv. Chem. Phys.*, 1982, **49**, 357.
13 I. del Pozo, M. Cartes, F. Llovell and A. Mejía, *J. Chem. Thermodyn.*, 2018, **121**, 121–128.
14 T. J. Bruno, T. M. Loestead, J. R. Riggs, E. L. Jorgenson and M. L. Huber, *Energy Fuels*, 2011, **25**, 2493–2507.
15 J. E. Landmeyer, P. M. Bradley, D. A. Trego, K. G. Hale and J. E. Haas, *Groundwater*, 2010, **48**, 30–41.
16 G. Kamath, J. Robinson and J. J. Potoff, *Fluid Phase Equilib.*, 2006, **240**, 46–55.
17 J. J. Potoff and J. I. Siepmann, *AIChE J.*, 2001, **47**, 1676–1682.
18 G. Kamath, F. Cao and J. J. Potoff, *J. Phys. Chem. B*, 2004, **108**, 14130–14136.
19 J. Stubbs, J. J. Potoff and J. I. Siepmann, *J. Phys. Chem. B*, 2004, **108**, 17596–17605.
20 G. M. Martin and J. I. Siepmann, *J. Phys. Chem. B*, 2001, **102**, 2569–2577.
21 K. A. Maerzke, N. E. Schultz, R. B. Ross and J. I. Siepmann, *J. Phys. Chem. B*, 2009, **113**, 6415–6425.
22 D. Frenkel and B. Smit, *Understanding Molecular Simulations*, Academic, San Diego, 2nd edn, 2002.
23 M. P. Allen and D. J. Tildesley, *Computer Simulation of Liquids*, Oxford University Press Claredon, Oxford, 2nd edn, 2017.
24 D. van der Spoel, E. Lindahl, B. Hess, G. Groenhof, A. E. Mark and H. J. Berendsen, *J. Comput. Chem.*, 2005, **26**, 1701–1718.
25 G. Galliero, M. M. Piñeiro, B. Mendiboure, C. Miqueu, T. Lafitte and D. Bessieres, *J. Chem. Phys.*, 2009, **130**, 104704.
26 G. Galliero, *J. Chem. Phys.*, 2010, **133**, 074705.
27 J. M. Míguez, M. M. Piñeiro and F. J. Blas, *J. Chem. Phys.*, 2013, **138**, 034707.
28 M. A. Cuendet and W. F. V. Gunsteren, *J. Chem. Phys.*, 2007, **127**, 184102.
29 S. Nosé, *Mol. Phys.*, 1984, **52**, 255–268.
30 H. J. C. Berendsen, J. P. M. Postma, W. F. V. Gunsteren, A. D. Nola and J. R. Haak, *J. Chem. Phys.*, 1984, **81**, 3684.
31 H. Hulshof, *Ann. Phys.*, 1901, **4**, 165–186.
32 J. S. Rowlinson and B. Widom, *Molecular Theory of Capillarity*, Claredon Press, 1982.
33 E. D. Miguel, F. J. Blas and E. M. D. Río, *Mol. Phys.*, 2006, **104**, 2919–2927.
34 E. D. Miguel and G. Jackson, *J. Chem. Phys.*, 2006, **125**, 164109.
35 J. S. Rowlinson and F. L. Swinton, *Liquids and Liquid Mixtures*, Butterworth, London, 1982.
36 H. W. Xiang, *The Corresponding-States Principle and Its Practice Thermodynamic. Transport and Surface Properties of Fluids*, Elsevier, Amsterdam, 2005.
37 E. A. Guggenheim, *J. Chem. Phys.*, 1945, **13**, 253–261.
38 B. Widom, *J. Chem. Phys.*, 1965, **43**, 3892.
39 M. Modell and J. D. Tester, *Thermodynamics and its applications*, iPrentice-Hall, New York, 3rd edn, 1998.
40 F. J. Blas, L. G. MacDowell, E. D. Miguel and G. Jackson, *J. Chem. Phys.*, 2008, **129**, 144703.
41 L. G. MacDowell and F. J. Blas, *J. Chem. Phys.*, 2009, **131**, 074705.
42 J. G. Sampayo, F. J. Blas, E. D. Miguel, E. A. Müller and G. Jackson, *J. Chem. Eng. Data*, 2010, **55**, 4306.
43 F. J. Blas, A. I. Moreno-Ventas Bravo, J. M. Míguez, M. M. Piñeiro and L. G. MacDowell, *J. Chem. Phys.*, 2012, **137**, 084706.
44 J. M. Garrido, M. Cartes, A. Mejía, J. Algaba, J. M. Míguez, F. J. Blas, A. I. Moreno-Ventas Bravo and M. M. Piñeiro, *J. Supercrit. Fluids*, 2017, **128**, 359–369.
45 J. Algaba, J. M. Garrido, J. M. Míguez, A. Mejía, A. I. M.-V. Bravo and F. J. Blas, *J. Phys. Chem. C*, 2018, **122**, 16142–16153.
46 J. Algaba, M. Cartes, A. Mejía, J. M. Míguez and F. J. Blas, *J. Phys. Chem. C*, 2019, **123**, 20960–20970.
47 K. Binder, *Z. Phys. B: Condens. Matter*, 1981, **43**, 119.
48 E. Salomon and M. Mareschal, *J. Phys.: Condens. Matter*, 1991, **3**, 3645.
49 F. J. Blas, A. I. Moreno-Ventas Bravo, J. A. Fernández, F. J. Martínez-Ruiz and L. G. MacDowell, *J. Chem. Phys.*, 2014, **140**, 114705.
50 F. J. Martínez-Ruiz, F. J. Blas, B. Mendiboure and A. I. Moreno-Ventas Bravo, *J. Chem. Phys.*, 2014, **141**, 184701.
51 M. Dinpajooh, P. Bai, D. A. Allan and J. I. Siepmann, *J. Chem. Phys.*, 2015, **143**, 114113.
52 J. J. Potoff and T. Z. Panagiotopoulos, *J. Chem. Phys.*, 1998, **109**, 10914–10920.
53 J. Pérez-Pellitero, P. Ungerer, G. Orkoulas and A. D. Mackie, *J. Chem. Phys.*, 2006, **125**, 054515.

PCCP

ROYAL SOCIETY OF CHEMISTRY

PAPER

Cite this: *Phys. Chem. Chem. Phys.*, 2022, **24**, 5371

Molecular dynamics of liquid–liquid equilibrium and interfacial properties of aqueous solutions of methyl esters

Esther Feria,[a] Jesús Algaba,[b] José Manuel Míguez,[a] Andrés Mejía[c] and Felipe J. Blas *[a]

Received 22nd November 2021,
Accepted 3rd February 2022

DOI: 10.1039/d1cp05346a

rsc.li/pccp

In this work, the liquid–liquid phase equilibria and interfacial properties of methyl ester + water binary mixtures are determined at atmospheric pressure and from 278 to 358 K combining the direct coexistence technique and molecular dynamics simulations. Methyl esters are modelled using new parametrizations based on the united atom TraPPE model force field proposed recently by us [E. Feria, J. Algaba, J. M. Míguez, A. Mejía, P. Gómez-Álvarez and F. J. Blas, *Phys. Chem. Chem. Phys.*, 2019, **22**, 4974–4983] that are able to predict the vapour–liquid interfacial properties of pure methyl esters with high accuracy. In the case of water, we consider the well-known TIP4P/2005 model, the most popular rigid and non-polarizable model to describe the interfacial properties of pure water. The simulations are performed using the direct coexistence technique in the isothermal–isobaric or NP_zAT ensemble in combination with molecular dynamics. We obtain density profiles, temperature–densities and temperature–composition projections of the phase diagrams, and interfacial tensions. The liquid–liquid interfacial tension is calculated from the normal and tangential components of the pressure tensor according to the mechanical virial route. We pay attention particularly to the ability of the molecular models in predicting the experimental behavior of the systems. Simulation results are able to account for the liquid–liquid phase equilibria of these binary mixtures, in good agreement with the experimental data taken from the literature. Unfortunately, experimental values for interfacial tensions are substantially overestimated by predictions from computer simulations in all cases. To our knowledge, this is the first time that the liquid–liquid phase equilibrium and interfacial properties of methyl ester + water mixtures have been predicted from computer simulations.

1 Introduction

Biodiesel is considered a clean, renewable, and eco-friendly alternative to reduce the use and production of diesel from fossil fuel sources. The main advantages are that biodiesel can be used as a liquid fuel in diesel engines without any extensive modification, and it can be used in pure form or blended with petroleum diesel in any percentage, where the most common blend is 20% biodiesel and 80% petroleum diesel. Biodiesel can be produced by reacting an alcohol (or bioalcohol) with a group of mono-alkyl esters, which are obtained from vegetable oil, animal fat, or recycled cooking grease. Depending on the alcohol (methanol or ethanol) used in the transesterification reaction route, it is possible to obtain Fatty Acid Methyl Esters (FAMEs) or Fatty Acid Ethyl Esters (FAEEs), respectively.[1,2,3] Both FAMEs and FAEEs are good substitutes for petroleum-based diesel, moreover, FAEEs are more ecosystemic and renewable than FAMEs as ethanol can also be obtained from a renewable source (*e.g.* food crops, waste vegetables, algae, fruits, root vegetables, wood waste, cellulose, forest waste, *etc.*).[1,2,4]

Unfortunately, the production of biodiesel based on FAEEs has not yet been sufficiently developed for efficient use.[5] On the other hand, the production and technical use of FAMEs are mature techniques but the evaluation of its environmental impact is limited as the thermophysical properties needed to describe the phase and interfacial behavior of FAMEs in contact with water are undetermined, especially in the case of interfacial properties. Interfacial properties, such as interfacial tension, surface activity, and wettability of these aqueous mixtures at liquid–liquid (LL) equilibrium, are key properties

[a] *Laboratorio de Simulación Molecular y Química Computacional, CIQSO-Centro de Investigación en Química Sostenible and Departamento de Ciencias Integradas, Universidad de Huelva, Huelva 21007, Spain. E-mail: felipe@uhu.es*
[b] *Department of Chemical Engineering, Imperial College London, South Kensington Campus, London SW7 2AZ, UK*
[c] *Laboratorio de Cohesión, Departamento de Ingeniería Química, Universidad de Concepcion, POB 160-C, Correo 3, Chile*

not only to evaluate the environmental impact of FAMEs on water but also to design technical strategies to remove it from water and for groundwater remediation.[6]

Focused on measurable properties related to interfacial properties, the only available contributions are the works of Gros and Feuge[7] and del Pozo *et al.*[8] In the first case, the authors reported the interfacial tension for binary mixtures of methyl valerate and methyl heptanoate with water. However, these reported data have been measured only at 348.15 K and the device used (Noüy tensiometer) is not the most appropriate and accurate tensiometer for LL systems. In the second case, systematic determination of both liquid densities and interfacial tensions as a function of temperature is reported for aqueous binary mixtures from methyl formate to methyl heptanoate, where a more adequate and precise tensiometer was used (*i.e.*, a spinning drop tensiometer). From the tensiometry results, it is interesting to observe the parabolic behavior of the interfacial tension with the temperature and the dependence of the interfacial tension with the molecular chain length. In order to explain the interfacial behavior in terms of these latter variables (*i.e.*, temperature, and molecular chain length), del Pozo *et al.*[8] used a simplified version of the van der Waals square gradient theory[9] coupled to the Non-Random-Two Liquid model (NRTL) activity coefficient model proposed by Renon and Prausnitz.[10] The used model provides a route to correlate the experimental information but not bring a molecular description of the interfacial concentration of species at the interfacial region, which is the fundamental piece to explain the parabolic behavior of the interfacial tension.

Unfortunately, little information on the type of phase behaviour exhibited by these mixtures and on the existence of critical points is available from the experimental data. To the best of our knowledge, the only mixture for which experimental information about the existence of a critical point exists is the methyl acetate + water binary system. According to the review of Maczyński and collaborators,[11] this mixture exhibits an upper critical solution temperature (UCST) at ambient pressure and 381.2 K, for a molar fraction of methyl acetate $x_1 = 0.212$. However, there is no information about which particular type of phase behaviour is exhibited nor is there experimental information for the rest of the members of the homologous series. Preliminary calculations have been performed using the well-known SAFT-VR Mie formalism and determined that these mixtures exhibit vapour–liquid, liquid–liquid, and vapour–liquid–liquid phase equilibria.[12] In addition to this, the methyl acetate + water binary mixture exhibits type II phase behaviour according to the classification Scott and Konynenburg.[13,14]

In order to fill the gap between the experimental results and a molecular level explanation of the thermal and molecular chain length impact on the behavior of the interfacial tension, this work is focused on the molecular dynamics simulation of the selected binary mixtures of FAMEs (*i.e.*, from methyl acetate to methyl heptanoate) with water in LL equilibrium. The main advantage of this approach is to obtain a molecular picture of FAMEs and water at the interfacial region and to relate this behavior to the surface activity of the interfacial concentration of species and the corresponding interfacial tension.

The main goal of this work is to predict the LL phase equilibria and the anomalous interfacial tension in aqueous solutions of the first members of the methyl esters chemical family (from methyl acetate to methyl heptanoate) described by using the new transferable molecular parameters[15] of the TraPPE-UA force field, proposed in the last year. To our knowledge, this is the first time that the LL interfacial properties, and particularly the interfacial tension, of the methyl ester + water systems are studied from computer simulations.

Note that the use of a group contribution approach allows the direct generalization of the models to other compounds and mixtures of the same chemical family. This transferable approach provides an important predictive character of the models, which is very useful when experimental data are not available. However, a different approach is also possible, especially in the cases in which predictions from a group contribution fail for certain chemical groups in small molecules of a given homologous series, such as alkanes and alcohols.[16,17] For these cases, it is possible to use specific shape and/or interaction parameter values for some groups. However, one of the goals of the current work is to check if the use of transferable parameters taken directly from the TraPPE database is able to provide an appropriate description of the vapor–liquid phase equilibria and interfacial properties of aqueous solutions of methyl esters.

The organization of this paper starts with the description in Sections 2 and 3 of the force fields used to describe FAMEs and water and the simulation details. In the next section, the main results of interfacial properties are presented and discussed. Finally, the main conclusions are summarized in the last section.

2 Molecular models

Methyl esters have been recently modeled as linear flexible molecules using the TraPPE-UA approach by Feria *et al.*[15] to predict their liquid–vapor phase behavior and interfacial properties, from methyl acetate to methyl heptanoate. According to this, molecular parameters are taken from existing parametrizations for other molecules, including alkanes and alkenes, carbon dioxide, ethers, and carboxylic acids, to predict the behaviour of the methyl ester homologous series.[18] Particularly, the parameters of the carbonyl oxygen (=O) are those used for the oxygen in the carbon dioxide model proposed by Potoff and Siepmann,[19] and the carbonyl carbon (C=) is modeled using the carboxylic acid models proposed by Kamath *et al.*[20] The molecular parameters involved in the methoxy group (–O–CH_3, CH_3–C and CH_2–C) are taken from the work of Stubbs *et al.*[21] Finally, the parameters of methyl (CH_3–CH_x) and methylene (–CH_2–CH_x) chemical groups are those of linear alkanes proposed by Martin and Siepmann.[16] Table 1 includes the well depth, size, and partial charge parameters for the TraPPE-UA force fields used in this work corresponding to non-bonded interactions of all the chemical groups.

There exist a considerably large number of molecular models for water, including the well-known SPC/E,[24] TIP4P,[25] and TIP5P[26] families. The TIP4P models (TIP4P,[25] TIP4P/EW[27]

Table 1 Lennard-Jones well depth, ε, size, σ, and partial charge q, parameters for the TIP4P/2005 and TraPPE-UA force fields corresponding to non-bonded interactions of water and methyl esters. The letters in parenthesis indicate the atom a particular site is bonded to. Parameter values for water are taken from the work of Abascal *et al.*[22] and those for methyl esters from the work of Siepmann and co-workers.[16,19–21] See also the TraPPE webpage[23] and our previous work[15]

Atom	ε/k_B (K)	σ(Å)	$q(e)$
H_2O (TIP4P/2005)			
O	93.20	3.1589	0.0
H	0.0	0.0	0.5564
M	0.0	0.0	−1.1128
Methyl esters (TraPPE-UA)			
CH_3–(O)	98.0	3.75	0.25
–O–	55.0	2.80	−0.40
C═(O)	41.0	3.90	0.55
O═(C)	79.0	3.05	−0.45
CH_3–(C)	98.0	3.75	0.05
CH_2–(C)	46.0	3.95	0.05
CH_3–(CH_x)	98.0	3.75	0.00
CH_2–(CH_x)	46.0	3.95	0.00

and TIP4P/2005[22]) consist of four interacting sites placed on the oxygen atom (O), on each of the hydrogen atoms (H), and along the H–O–H bisector (the so-called M site). In this case, we have selected the well-known rigid and non-polarizable TIP4P/2005 version.[22] This model is able to provide accurate estimates of thermodynamic properties, phase equilibria, and interfacial properties of pure water compared with similar models.[28,29] In addition to that, the model is remarkably proficient in the estimation of LL phase equilibria and interfacial properties of binary and ternary mixtures containing water, including CH_4 + H_2O,[30] CO_2 + H_2O[31] and CH_4 + CO_2 + H_2O[32] systems. Molecular parameters for the TIP4P/2005 model for water are also included in Table 1.

The nonbonded intermolecular and intramolecular interactions between chemical groups separated by more than three bonds are accounted for by Lennard-Jones (LJ) and Coulomb potentials,

$$U(r_{ij}) = 4\varepsilon_{ij}\left[\left(\frac{\sigma_{ij}}{r_{ij}}\right)^{12} - \left(\frac{\sigma_{ij}}{r_{ij}}\right)^{6}\right] + \frac{q_i q_j}{4\pi\varepsilon_0 r_{ij}} \quad (1)$$

where r_{ij} is the distance between interacting sites i and j, σ_{ij} and ε_{ij} are the diameter and well depth associated with the LJ intermolecular potential, respectively, q_i and q_j are the partial charges on these sites, and ε_0 is the permittivity of the vacuum. The molecular parameters used in this work to describe the nonbonded interactions of water and methyl esters, including partial charges values for electrostatic interactions, are listed in Table 1. All the LJ parameters for unlike interactions are obtained using the well-known Lorentz–Berthelot combining rules.

The values of the fixed bond lengths for water and methyl esters, presented in Table 2, are taken from the original works of Abascal and Vega[22] and from the TraPPE webpage,[23] respectively. The bending and torsional force field parameters corresponding to the bonded interactions for the methyl esters are obtained from the TraPPE-UA force fields.[23] The bond bending potential is controlled through a harmonic function,

$$U_{bend}(\theta) = \frac{1}{2}\kappa_\theta(\theta - \theta_0)^2 \quad (2)$$

where θ, θ_0 and κ_θ are the measured bending angle, the equilibrium bending angle, and the force constant, respectively. Table 3 contains a list of the θ_0 and κ_θ values used in this work. According to the philosophy of the TraPPE-UA force field approach, the dihedral rotations around the bonds connecting four chemical groups account for the standard cosine series of the dihedral angle,

$$U_{tor}(\phi) = c_0 + c_1[1 + \cos(\phi)] + c_2[1 + \cos(2\phi)] + c_3[1 + \cos(3\phi)] \quad (3)$$

where the Fourier coefficients c_i, for $i = 0\cdots3$ are listed in Table 4.

Table 2 Bond length values of the TIP4P/2005 and the TraPPE-UA force fields corresponding to water and methyl esters. All values are taken from the work of Abascal *et al.*[22] and the TraPPE webpage,[23] respectively

Bond	Bond length (Å)
H_2O (TIP4P/2005)	
O–H	0.9572
O–M	0.1546
Methyl esters (TraPPE-UA)	
C═O	1.200
C–O	1.344
CH_3–O	1.410
CH_x–C	1.520
CH_2–CH_x	1.540

3 Simulation details

We combine molecular dynamics (MD) computer simulations and the direct coexistence methodology to obtain the phase equilibria and interfacial properties of aqueous solutions of several methyl esters. Computer simulations are performed at atmospheric pressure and temperatures varying from 278 to 358 K for each aqueous mixture. In particular, we simulate the LL interfaces using the isothermal–isobaric or $NP_zA T$ ensemble to ensure that temperature and pressure are constants. According to this, the interfacial area $A = L_x \times L_y$ is kept constant and only L_z is varied along the simulation. Here, L_x, L_y, and L_z are the dimensions of the simulation box along the x-, y-,

Table 3 Bending potential parameters for the TraPPE-UA force field corresponding to methyl esters. All values are taken from the TraPPE webpage[23]

Bending	θ (deg)	k_θ/k_B (K rad^{-2})
CH_3–O–C	115	62 500
O–C═O	125	62 500
O–C–CH_3	110	70 596
O═C–CH_3	125	62 500
O═C–CH_2	125	62 500
C–CH_2–CH_2	114	62 500
CH_2–CH_2–CH_2	114	62 500
CH_2–CH_2–CH_3	114	62 500

Table 4 Torsional potential parameters for the TraPPE-UA force field corresponding to methyl esters. All values are taken from the TraPPE webpage[23]

Torsion	c_0/k_B (K)	c_1/k_B (K)	c_2/k_B (K)	c_3/k_B (K)
CH_3–O–C═O	11594.6	3374.2	−4118	−613.6
CH_3–O–C–CH_3	6551.3	1566.1	−4196	789.2
CH_3–O–C–CH_2	6551.3	1566.1	−4196	789.2
O–C–CH_2–CH_2	839.87	−2133.17	106.68	3097.72
O–C–CH_2–CH_3	839.87	−2133.17	106.68	3097.72
O═C–CH_2–CH_2	1121.13	142.79	−115.68	−1172.92
O═C–CH_2–CH_3	1121.13	142.79	−115.68	−1172.92
C–CH_2–CH_2–CH_2	1009.97	−2018.93	136.38	3165.28
C–CH_2–CH_2–CH_3	1009.97	−2018.93	136.38	3165.28
CH_2–CH_2–CH_2–CH_2	1009.97	−2018.93	136.38	3165.28
CH_2–CH_2–CH_2–CH_3	1009.97	−2018.93	136.38	3165.28

and z-axis, respectively. For convenience, the z-axis is chosen perpendicular to the planar LL interface, *i.e.*, parallel to the direction along which the system exhibits the inhomogeneity. We use periodic boundary conditions in all three directions.

The simulation boxes used to study the LL interfaces considered in this work have been prepared as follows. For each mixture and temperature, we first equilibrate two independent simulation boxes using the isothermal–isobaric ($NP_z\mathscr{A}T$) ensemble at atmospheric pressure and the corresponding temperature. Particularly, we equilibrate independently two bulk pure liquid phases, one containing N_o = 1000 methyl ester (organic) molecules and another containing N_w = 2200 water molecules. This is done since all the aqueous solutions of methyl esters exhibit a very high degree of immiscibility.[33–35] The dimensions L_x and L_y of all the simulation boxes used in this work are kept constant with $L_x = L_y$ = 4.0 nm. Initial lengths of the simulation boxes along the z-axis vary depending on the mixture considered. For the case of aqueous solutions of methyl acetate and methyl propionate, L_z varies from 20.8 to 21.8 nm, and from 24.3 to 26.1 nm, when temperature varies from 278 to 358 K, respectively. For the rest of the mixtures, L_z = 29.0, 32.2, 36.0, and 39.9 nm for the methyl butyrate +, methyl valerate +, methyl hexanoate +, and methyl heptanoate + water mixtures, respectively. Once both simulation boxes have been equilibrated separately, an inhomogeneous biphasic simulation box is constructed assembling along the z direction the simulation box corresponding to the water-rich phase and two replicas of the organic-rich phase at both ends. Then, this biphasic simulation box is allowed to evolve at constant temperature and pressure until the two parallel explicit interfaces are fully equilibrated. The length and number of molecules used ensures that the two independent planar interfaces existing during simulations do not interact with each other and that the three liquid bulk slabs (organic-rich, water-rich, and organic-rich liquid phases) are thick enough to ensure that the equilibrium properties of each phase can be calculated correctly.

All MD simulations have been carried out using the GROMACS software package (version 4.6.1).[36] We use the Verlet leapfrog algorithm[37] with a time step of 0.001 ps. This time step value is chosen to ensure that the torsional potentials of the ester models are correctly calculated. Temperature and pressure are kept constant using a Nosé–Hoover[38,39] thermostat and a Parrinello–Rahman[40] barostat with a relaxation time of 2 ps, respectively. In order to reduce the truncation and system size effects involved in the phase equilibrium and interfacial properties calculations, the cut-off radius is set equal to r_c = 1.95 nm for the methyl acetate + water mixture and 1.975 nm for the rest of the aqueous solutions. These elections correspond in all cases to a reduced cut-off radius with respect to the largest segment size of 5σ. It has been shown by several authors[41–43] that such a value provides a reasonable description for the interfacial properties. Note also that this cut-off radius is compatible with the dimensions L_x and L_y of all the simulation boxes used in this work, $L_x = L_y$ = 4 nm. This corresponds to a value $L_x = L_y = 10.13\sigma$. According to Chen,[44] González–Melchor *et al.*[45] and Janeček,[46] the simulation results do not show a dependence of the interfacial tension on the surface area for systems with $L_x = L_y > 10\sigma$, as in this work. The long-range interactions due to coulombic forces are determined using the three-dimensional Ewald technique. Particularly, the real part of the coulombic potential is also truncated at r_c = 1.95–1975 nm. The Fourier term of the Ewald sums is evaluated using the particle mesh Ewald (PME) method.[47] The width of the mesh is 1 Å; with a relative tolerance of 10^{-5} Å. Simulations of the homogeneous liquid systems are equilibrated during 10 ns. After this, the inhomogeneous systems are also equilibrated during 10 ns. After the systems reach equilibrium, the properties of the LL coexisting phases are obtained as appropriate averages during 50 ns. In order to estimate errors on the variables computed, the sub-blocks average method has been applied.[48] In this approach, the production period is divided into M independent blocks. The statistical errors are then estimated from the standard deviation of the average $\bar{\sigma}/\sqrt{M}$, where $\bar{\sigma}$ is the variance of the block averages and M has been fixed in this work to M = 10.

The interfacial tension, γ, is obtained from the diagonal components of the pressure tensor using the mechanical route[49,50] as,

$$\gamma = \frac{L_z}{2}\left[\langle P_{zz}\rangle - \frac{\langle P_{xx}\rangle + \langle P_{yy}\rangle}{2}\right] \quad (4)$$

In eqn (4), the additional factor 1/2 comes from having two interfaces in the system, and L_z is the size of the simulation box in the z direction, defined along the longitudinal dimension across the interface.

4 Results

In this section, we present and discuss the LL phase behavior of aqueous solutions of methyl esters as obtained from MD simulations. Simulations are performed using the direct coexistence method in the anisotropic isothermal–isobaric or $NP_z\mathscr{A}T$ ensemble. We focus on the thermodynamic and structural properties, including density profiles, coexistence densities and compositions, and interfacial tension.

Fig. 1 shows the density profiles obtained by MD simulations of six methyl ester + water mixtures (from methyl acetate to methyl heptanoate) at atmospheric pressure and temperatures from 278 up to 358 K. For the sake of clarity, we only plot half of the profiles corresponding to one of the interfaces. The left side of the density profiles represents the organic-rich liquid phase and the right side the water-rich liquid phase. The inhomogeneous box is divided into 200 parallel slabs in the z-direction in order to study the density profiles. The molecular density profiles are obtained by assigning the position of each interacting site to the corresponding slab and constructing the molecular density from mass balance considerations.

An inspection of the density profiles of water across the interface indicates a monotonic increasing behavior when passing from the organic-rich liquid phase to the water-rich liquid phase. Particularly, water density profiles show the approximated traditional shape of the hyperbolic tangent function, without change in the shape of the profiles as the temperature and molecular weight of the organic compound are increased. In addition to that, the density of water does not vary with temperature at the organic-rich liquid phase. However, it slightly decreases as the temperature is increased at the water-rich liquid phase. The behaviour of water density in the organic-rich liquid phase, as well as that of the methyl esters density, clearly indicates a relatively low solubility of water in the organic phase.

The behaviour and structure of the density profiles of methyl esters observed in this work are similar to that exhibited by other mixtures, including aqueous mixtures of carbon dioxide[51] and methane.[30] They show an adsorption peak located at the organic-rich liquid phase next to the interface. This peak is usually related with the activity of the organic compound at the interface. Particularly interesting in this context is the LL interfacial behaviour of linear 1-alcohol + water homologous series mixtures. Methyl esters, although they are clearly different compounds, present some functional similarities. They have a polar chemical group at the end of the quasi-linear molecular structure and an alkyl tail that increases in length as the molecular weight of the molecule becomes larger, as happens in linear 1-alcohols. Algaba *et al.*[52] have recently shown by means of computer simulation that alcohol + water mixtures exhibit preferential adsorption of alcohols at the LL

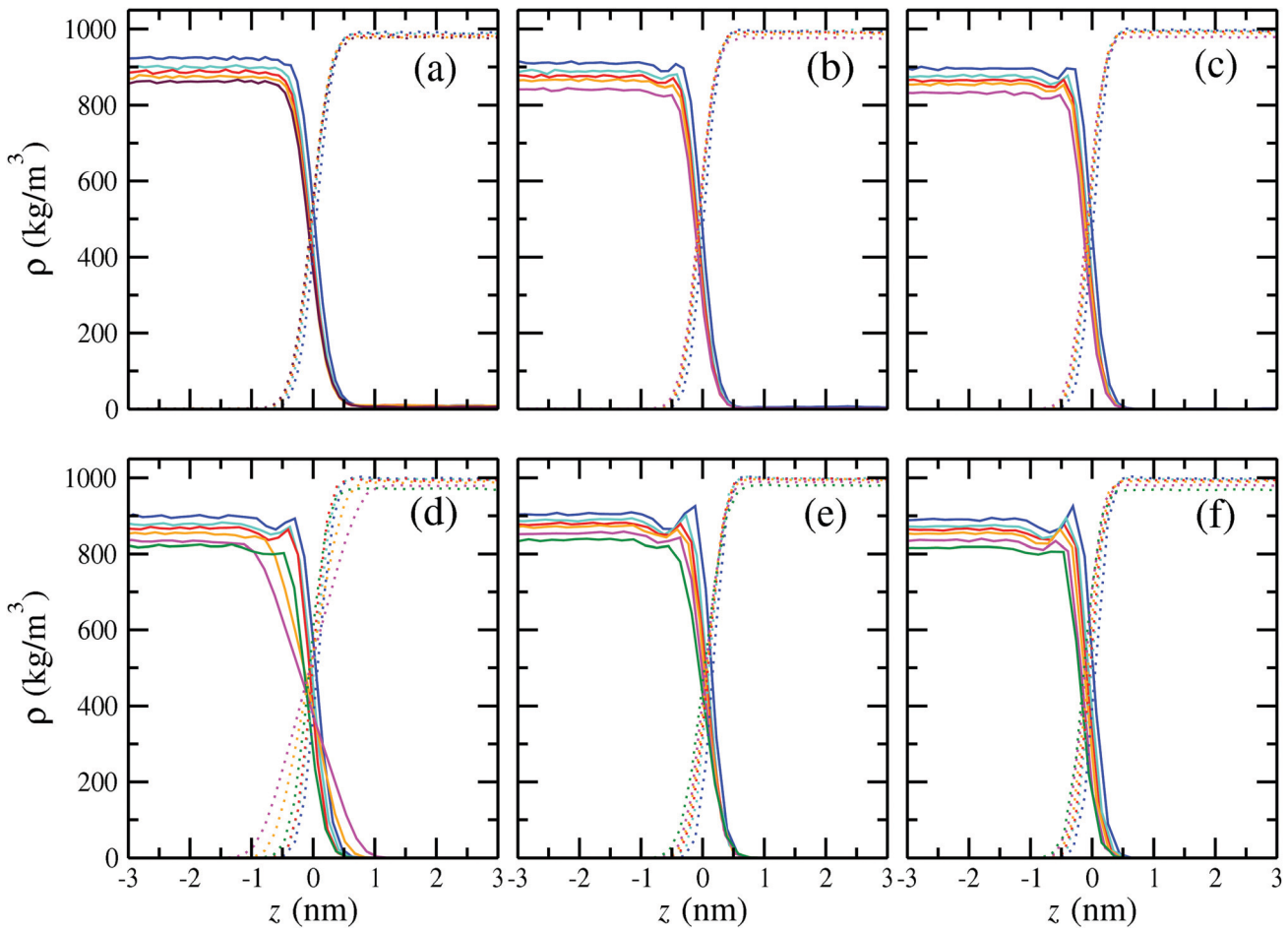

Fig. 1 Simulated equilibrium density profiles, $\rho(z)$, across the LL interface of methyl esters (continuous curves) and water (dotted curves) as obtained from MD NP_zAT simulations of (a) methyl acetate + water, (b) methyl propionate + water, (c) methyl butyrate + water, (d) methyl valerate + water, (e) methyl hexanoate + water and (f) methyl-heptanoate + water, at 1 bar and 278 (blue), 298 (turquoise), 308 (red), 318 (orange), 328 (violet), 338 (magenta), and 358 K (green).

interface. However, the structure of the LL interface of aqueous solutions of alcohols is different than that of the methyl ester + water mixtures. According to the results presented by Algaba *et al.*, density profiles of alcohol molecules exhibit a more pronounced oscillatory behaviour across the LL interface. The profiles exhibit depressions (desorptions) and complementary peaks (adsorptions) directly related with the behaviour of the corresponding density profiles of water, indicating a self-organized structure of alcohols and water molecules near the interface. Particularly, these mixtures form bilayers of alcohols molecules oriented perpendicularly to the interface, together with a small accumulation (adsorption) of water molecules in the organic-rich phase at the LL interface. This is especially true as the molecular weight of the alcohols increases. However, according to our results, methyl esters do not exhibit preferential orientation at the interface, even in the case of the methyl heptanoate + water mixture.

We have also calculated, but it is not shown here, the density profiles corresponding to the ester chemical group of the methyl ester molecules across the interface. These density profiles exhibit the same qualitative behaviour as the density profile of methyl ester molecules presented in Fig. 1. The absence of preferential orientation at the interface described in the previous paragraph is also corroborated looking at the interface with the "eyes" of MD. Fig. 2 shows snapshots extracted from MD trajectories of the simulation of methyl butyrate +, methyl valerate +, methyl hexanoate +, and methyl heptanoate + water mixtures. As can be seen in all cases, there is no preferential orientation of the methyl ester molecules at the interface. It is useful to compare the snapshots presented in

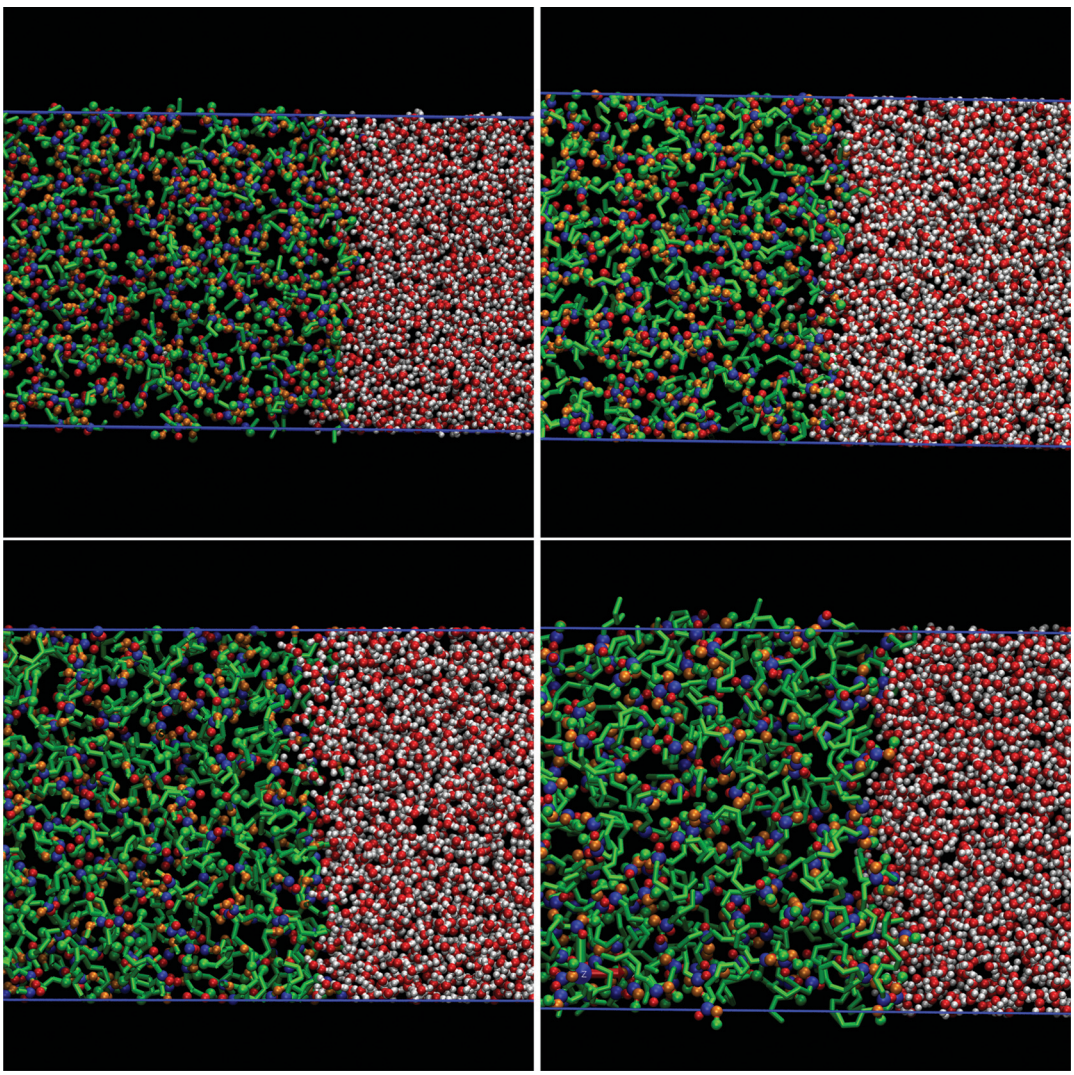

Fig. 2 Snapshots of the LL interface obtained from MD $NP_{z}\mathscr{A}T$ simulations of the methyl butyrate + (top left), methyl valerate + (top right), methyl hexanoate + (bottom left), and methyl-heptanoate + water (bottom right) mixtures at 1 bar and 278 K. The green licorice representation corresponds to alkyl groups of methyl esters (CH_3 and CH_2 groups), orange, blue, and red spheres in the organic-rich liquid phase (van der Waals representation) correspond to the ester oxygen, carbonyl carbon, and carbonyl oxygen atoms of methyl esters, respectively, and red and white spheres (in the water-rich liquid phase) correspond to oxygen and hydrogen atoms in the water molecules, respectively.

Fig. 2 with those corresponding to the first members of the alcohol + water homologous series, butan-1-ol +, pentan-1-ol +, hexane-1-ol +, and heptan-1-ol + water mixtures (see Fig. 2 of the work of Algaba *et al.*[52]).

We think the differences observed between the self-organization of alcohols and the non-preferential orientation of methyl ester across the interface are related to the different ability of alcohols and methyl esters to form hydrogen bonds with water and with the non-equivalent molecular architectures of both organic compounds. Linear 1-alcohols have a hydroxyl chemical group, –OH, that makes alcohols polar. This allows hydrogen bonds to be formed with another alcohol and to water molecules in aqueous solutions. Particularly, both oxygen and hydrogen atoms can be acceptor and donor atoms, respectively, for hydrogen bonding with water molecules. However, the configuration of oxygen atoms in the case of methyl esters is not as favorable as in the case of alcohols. Methyl esters do not have available hydrogen atoms to act as a donor to form hydrogen bonds with water. In addition to that, the oxygen atom double-bonded to the carbon atom (carbonyl group), and especially the ester group (the oxygen bonded to the carbon of the carbonyl and methyl groups) are not particularly suited for hydrogen bonding. In other words, although these oxygen atoms could form hydrogen bonds with water molecules, the number of such bonds is small compared with the number of alcohol–water hydrogen bonds. Note that oxygen in methyl esters is not located at the end of the molecule, as in the case of the hydroxyl group in linear 1-alcohols. This also produces negative steric hindrance effects on hydrogen bonding. Finally, it is important to note that the alkyl chains of linear 1-alcohols promote the formation of ordered and packed layers at the water interface in aqueous solutions.[52] In contrast, the presence of the carbonyl groups in methyl esters produces difficulties to induce this packing, which is also prevented by the absence of a significant number of methyl ester–water hydrogen bonds at the interface.

From the information of the density profiles of methyl esters and water it is also possible to determine other interesting properties, including solubilities and coexistence densities. The coexistence densities can be calculated from the density profiles in the regions at which liquids are homogeneous, *i.e.*, averaging the appropriate central homogeneous liquid slabs in each phase excluding the interfacial region. See the works of Algaba *et al.*,[53,54] Garrido *et al.*,[31] and Mejía *et al.*[55] for further details. Coexistence densities of both phases as obtained from MD simulations are summarized in Table 5.

Fig. 3 shows the temperature–density or $T\rho$ projections of the phase diagram of aqueous solutions of methyl esters at atmospheric pressure. Liquid densities in both phases decrease as the temperature is increased. This behaviour is observed for the six mixtures considered. However, this trend is clearly marked in the case of the organic-rich liquid phase (left-side phase boundary in the figure) as compared with the case of the aqueous phase. In that case, although liquid density also decreases, its value is nearly constant. It is also interesting to compare the evolution of the phase boundaries of the $T\rho$ projection of the phase diagram as the molecular weight of the methyl ester is increased from that of methyl-acetate up to methyl-heptanoate. As can be seen, the phase boundary corresponding to the water-rich liquid phase stays nearly unchanged in all the cases. In contrast, the density values corresponding to the organic-rich phase decrease as the molecular weights of the esters increase. Predictions obtained from MD simulation are able to predict the experimental behaviour of the coexistence liquid densities with temperature and molecular weight presented by del Pozo and collaborators.[8] Particularly, the liquid density of the water-rich phase is quantitatively described by the molecular models. However, predictions corresponding to the organic-rich liquid phase deserve a more detailed description. As can be seen, computer simulation results slightly underestimate the density for the mixtures with methyl acetate, methyl propionate, and methyl butyrate at all temperatures. In particular, differences between the simulation and

Table 5 Liquid density of the organic-rich phase, $\rho^{(O)}$, liquid density of the water-rich phase, $\rho^{(W)}$, molar fraction of methyl ester in the organic-rich phase, $x_1^{(O)}$, molar fraction of methyl ester in the water-rich phase, $x_1^{(W)}$, and LL interfacial tension, γ, at 1 bar and different temperatures as obtained from MD NPz$_A$T simulations

T (K)	$\rho^{(O)}$ (kg m^{-3})	$\rho^{(W)}$ (kg m^{-3})	$x_1^{(O)}$	$x_1^{(W)}$	γ (mN m^{-1})
Methyl acetate (1) + water (2)					
278	922 (2)	989(2)	0.99771 (8)	0.001494 (2)	24.2 (2)
298	898 (2)	996(2)	0.998 (3)	0.001913 (2)	24.3 (2)
308	886 (2)	993(2)	0.997 (4)	0.00404 (4)	24.2 (2)
318	874 (2)	989(2)	0.997 (4)	0.00626 (4)	24.0 (2)
328	861 (2)	984(2)	0.998 (3)	0.00661 (3)	24.0 (1)
Methyl propionate (1) + water (2)					
278	909 (2)	1000 (3)	0.99872 (7)	0.00172 (2)	27.9 (2)
298	887 (2)	996 (1)	1.000 (4)	0.00324 (3)	28.1 (1)
308	876 (2)	993 (2)	1.000 (3)	0.003050 (2)	28.3 (2)
318	864 (2)	989 (2)	1.000 (4)	0.002719 (3)	28.7 (2)
338	841 (2)	979 (2)	0.999 (1)	0.00603 (3)	27.9 (1)
Methyl butyrate (1) + water (2)					
278	895 (2)	999 (1)	0.9998 (2)	0.00051 (1)	30.5 (2)
298	875 (2)	996 (1)	0.9999 (2)	0.00301 (3)	31.0 (2)
308	864 (2)	993 (1)	1.0000 (9)	0.00279 (3)	30.8 (2)
318	853 (2)	989 (2)	1.0000 (7)	0.00183 (1)	31.3 (3)
338	831 (2)	979 (2)	1.000 (1)	0.00508 (2)	30.7 (3)
Methyl valerate (1) + water (2)					
278	891(3)	999 (3)	1.000 (6)	0.000323 (8)	32.3 (2)
298	871(3)	997 (2)	1.000 (8)	0.00155 (1)	32.9 (4)
308	861(3)	994 (2)	1.000 (1)	0.000778 (8)	32.1 (2)
318	852(2)	989 (2)	1.000 (1)	0.00143 (1)	32.6 (2)
338	830(2)	980 (1)	1.000 (1)	0.00313 (1)	32.6 (3)
358	807(6)	972 (1)	1.000 (2)	0.006009 (2)	31.8 (2)
Methyl hexanoate (1) + water (2)					
278	889(6)	999 (2)	0.999985 (2)	0.000066 (2)	33.2 (4)
298	868(8)	999 (2)	1.000 (2)	0.000044 (2)	34 (3)
308	859(8)	997 (2)	1.000 (2)	0.000053 (2)	34 (4)
318	850(1)	995 (1)	1.000 (3)	0.000037 (1)	34 (3)
338	830(1)	989 (1)	1.0000 (4)	0.0000147(6)	34.2 (3)
358	808(1)	981 (1)	1.000 (2)	0.00370 (2)	33.9 (2)
Methyl heptanoate (1) + water (2)					
278	889 (2)	999 (1)	0.99999958 (5)	0.001202 (2)	35.3 (3)
298	870 (2)	996 (1)	1.00000 (3)	0.000161 (5)	35.21(4)
308	860 (2)	994 (1)	0.9997 (7)	0.001128 (5)	35.3 (4)
318	851 (2)	990 (1)	1.00000 (2)	0.0015 (1)	35.9 (3)
338	833 (2)	981 (1)	1.0000 (4)	0.001794 (9)	35.6 (3)
358	813 (2)	969 (1)	1.0000 (1)	0.00592 (2)	35.1 (3)

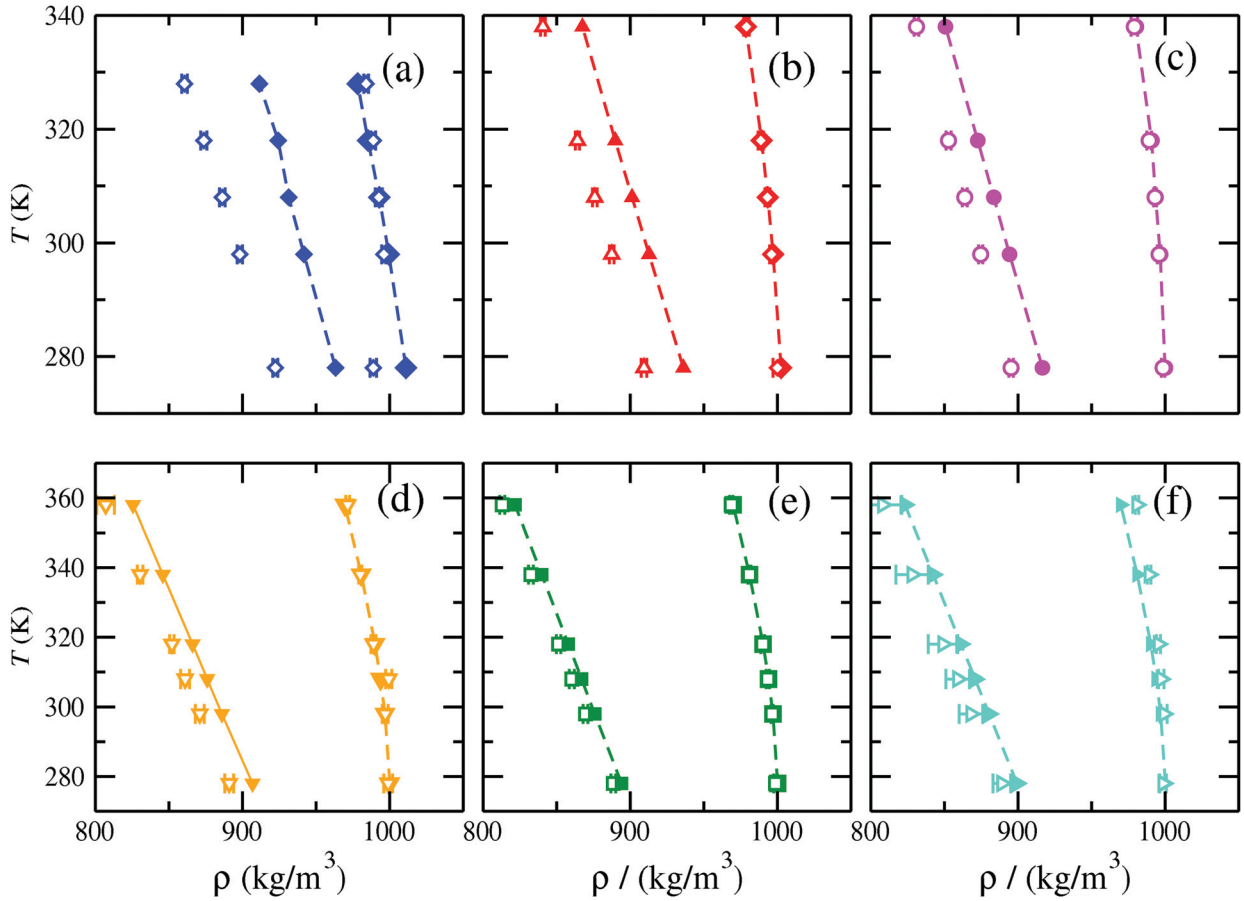

Fig. 3 $T\rho$ projection of the phase diagram of the (a) methyl-acetate + water (blue symbols), (b) methyl-propionate + water (red symbols), (c) methyl-butyrate + water (magenta symbols), (d) methyl-valerate + water (orange symbols), (e) methyl-hexanoate + water (green symbols) and (f) methyl-heptanoate + water (turquoise symbols) mixtures at 1 bar. Filled symbols and curves correspond to experimental data taken from the literature[8] and open symbols to the MD NP_zzAT simulation results obtained in this work.

experimental data are always below 5% (4.6% in the case of the mixture with methyl acetate). Nevertheless, the simulations are able to account for quantitatively the experimental organic-rich liquid densities in the whole range of temperatures (deviations between the experiments and simulation results are only equal to 0.6% in the case of methyl heptanoate). The behaviour observed for coexistence liquid densities of aqueous solutions of methyl esters is very similar to that found for alcohol + water binary mixtures. This phenomenology can be easily explained in terms of three key ingredients: (1) unlike organic–water interactions; (2) solubilities of methyl esters in water; and (3) exclude volume effects. We recommend to the reader the work of Algaba *et al.*[52] for further details.

As we have discussed previously, agreement between computer simulation predictions and experimental data taken from the literature for coexistence liquid densities is good except in the case of the mixtures containing the lighter methyl esters (methyl acetate, methyl propionate, and methyl butyrate). Molecular models used for water (TIP4P/2005)[22] and methyl esters (TraPPE)[15] are able to provide an accurate description of the vapour–liquid coexistence diagram of the real substances, including their interfacial properties, among many other thermodynamic and transport properties. According to our previous investigations,[52] the main reason for discrepancies should be found in the use of the Lorentz–Berthelot combining rules for the unlike organic–water intermolecular interactions. Particularly, the largest differences between simulations and experiments occur when the molecular weight of the methyl esters is lower. According to the results obtained in this work, in qualitative agreement with our previous work on alcohol + water mixtures, this happens since the solubility of water in methyl-acetate, methyl-propionate, and methyl-butyrate is not as low as for heavier methyl esters. Consequently, there is an important number of unlike organic–water intermolecular interactions in the system not accounted for appropriately by the Lorentz–Berthelot combining rules. As the molecular weight of the organic compound increases, solubility of water in the organic-rich liquid phases decreases and the effective number of unlike interactions lowers. This improves the agreement between simulations and experiments. This behaviour is completely similar to what happens with aqueous solutions of alcohols modelled with the TIP4P/2005 model for water and TraPPE force fields for alcohols. We recommend the work of Algaba and collaborators[52] for a complete discussion of this issue.

We now consider the effect of temperature and molecular weight, at atmospheric pressure, of the organic compound on

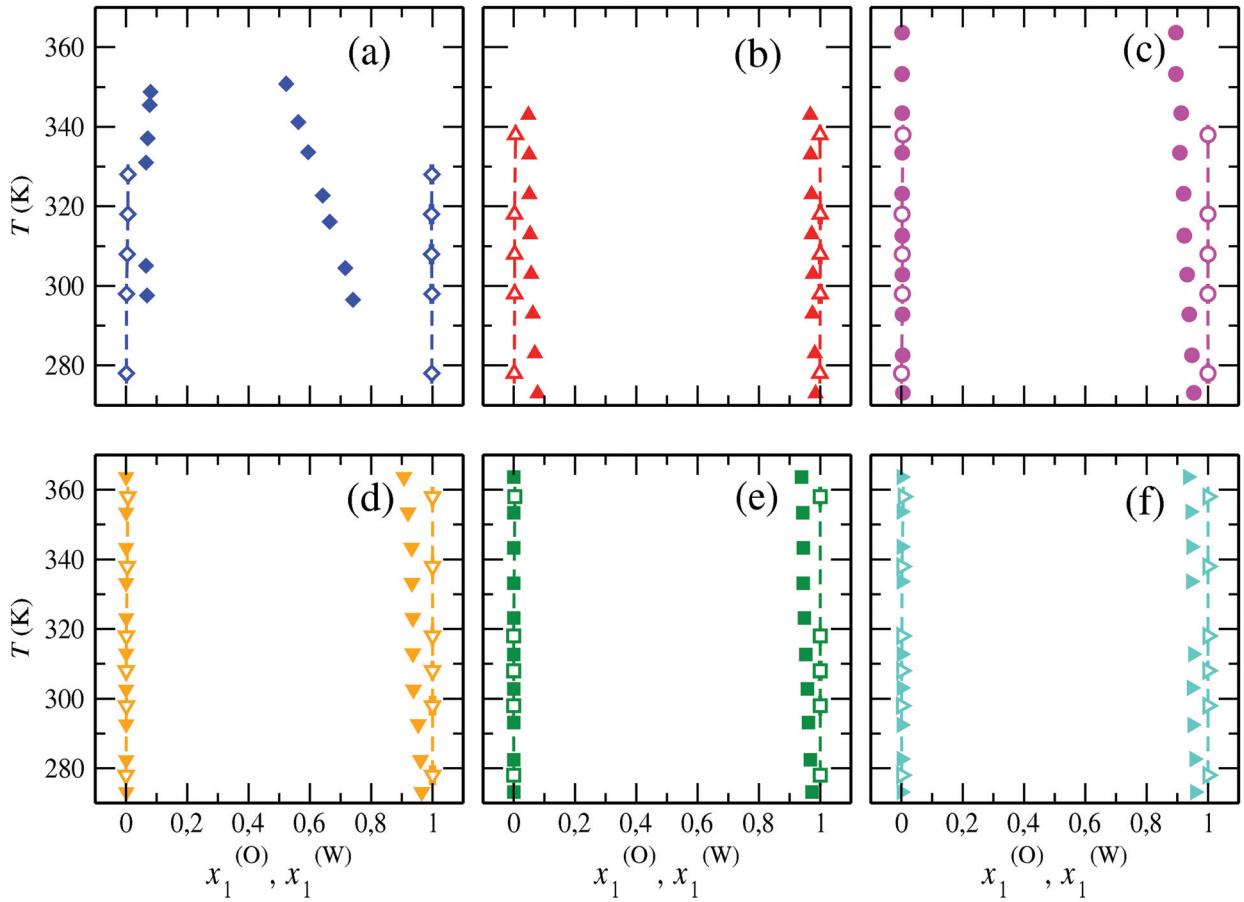

Fig. 4 T_x projection of the phase diagram of the (a) methyl-acetate + water (blue symbols), (b) methyl-propionate + water (red symbols), (c) methyl-butyrate + water (magenta symbols), (d) methyl-valerate + water (orange symbols), (e) methyl-hexanoate + water (green symbols) and (f) methyl-heptanoate + water (turquoise symbols) mixtures at 1 bar. Filled symbols correspond to experimental data taken from the literature,[33–35] open symbols to MD $NP_{zz}AT$ simulations obtained in this work and dashed curves to the fitting of the experimental values. $x_1^{(O)}$ and $x_1^{(W)}$ are the molar fractions of methyl esters in the organic-rich and in the water-rich liquid phases, respectively.

the temperature–composition or *Tx* projection of the phase diagram of aqueous solutions of methyl esters at atmospheric pressure. Fig. 4 shows the phase diagrams of the mixtures as obtained from MD simulations. As in the case of the $T\rho$ projections of the phase diagram, we have also included the corresponding experimental data taken from the literature.[33–35] This allows us to assess if the molecular models for water (TIP4/2005) and methyl esters (TraPPE) are able to predict accurately the LL composition of the mixtures. We have also included in Table 5 the molar fractions of the organic compounds in both liquid phases as obtained from MD simulations. As can be seen, the *Tx* projections of the mixtures are dominated by huge regions of LL immiscibility, for all the systems studied and at all the temperatures considered. According to our previous discussion, this behaviour is due to large unfavourable organic–water intermolecular interactions in the system. It is interesting to note that solubilities are practically constant as the temperature is increased in all cases. The only exception is the case of the methyl acetate + water mixture in which solubilities increase, especially the solubility of water in the organic-rich liquid phase, as temperature is increased.

Molecular models for water and methyl esters are able to provide a good description of the composition of the mixtures in all cases, except for the methyl acetate + water system. Agreement between experimental data taken from the literature and predictions obtained from MD simulations is reasonably accurate, although simulations predict wider LL immiscibility regions in all cases. In particular, results from MD simulations slightly overestimate the molar fractions of the methyl esters in the organic–rich liquid phase. In contrast, simulations are able to provide an accurate and quantitative agreement with experimental molar fractions of the methyl esters in the water–rich liquid phase. However, they slightly overestimate the molar fractions of the methyl propionate in the organic phase. In the case of the methyl acetate + water mixture, discrepancies between experiments and predictions from the MD simulations are larger, particularly in the case of the molar fraction of the methyl acetate in the organic–rich liquid phase. The reason of this lack of agreement is probably due to the presence of unlike interactions between methyl esters and water molecules that are not accounted for correctly using the standard Lorentz–Berthelot combining rules.

Finally, we analyze the ability of the TIP4P/2005 and TraPPE molecular models in predicting LL interfacial tensions of aqueous solutions of methyl esters. The results obtained from MD simulations are presented in Table 5 and Fig. 5. In addition to that, we have also included LL interfacial tensions measured in the laboratory[8] to check if the models are able to describe the characteristic behaviour of the LL interfacial tension, as a function of temperature, for the systems considered. As can be seen, computer simulations are able to describe the parabolic behavior exhibited by the LL interfacial tension with the temperature of all methyl ester + water binary mixtures. Additionally, predictions from MD simulations capture the existence of a relative maximum value for the interfacial tension in each system, larger values of interfacial tension as the carbon chain length of methyl esters is increased, and a reduction in the differences of interfacial tension, at constant temperature, as the molecular weight of methyl esters increases. Unfortunately, experimental values of interfacial tension are substantially overestimated by simulation predictions for all systems at all thermodynamic conditions. According to this, the accurate prediction of LL interfacial tensions for these types of systems continues to be a computational challenge. In fact, Algaba *et al.*[52] have demonstrated that is not possible to predict accurately the anomalous behavior of LL interfacial tensions for alcohols (from pentan-1-ol up to heptan-1-ol) + water mixtures. Interfacial tension is an extremely sensitive property to the molecular and simulation details, such as the cutoff radius, box size, and number of particles, among others. Additionally, it was observed that MD simulations underestimate the density of the organic phase of the mixture, which impacts the final value of the interfacial tension due to an underestimation of the organic density generated as an overprediction of the interfacial tension (*i.e.*, $\gamma \propto (\rho^{(w)} - \rho^{(0)})^4$)

Although the mixture model exhibits limitations for the quantitative prediction of this property, this is the first time the LL phase equilibria and interfacial tensions of methyl ester + water binary mixtures are determined from computer simulation. This work represents a first step to gain an understanding of the microscopic structure of LL interfaces from a molecular-based perspective.

5 Conclusions

We have determined the LL phase equilibria and interfacial properties of the methyl ester (from methyl acetate up to methyl heptanoate) + water binary mixtures at atmospheric pressure and temperatures from 278 to 358 K using MD molecular

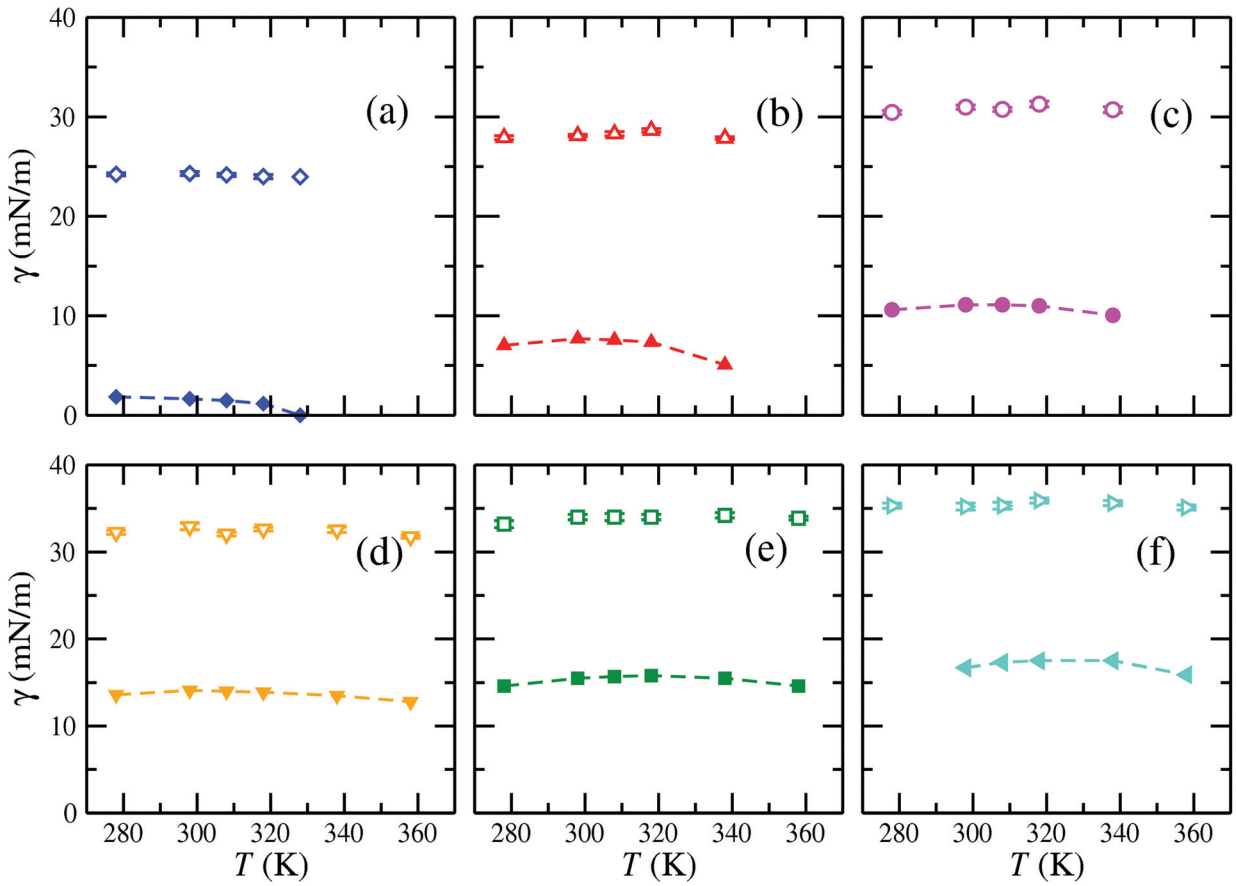

Fig. 5 LL interfacial tension as a function of temperature of the (a) methyl acetate + water (blue symbols), (b) methyl propionate + water (red symbols), (c) methyl butyrate + water (magenta symbols), (d) methyl valerate + water (orange symbols), (e) methyl hexanoate + water (green symbols) and (f) methyl heptanoate + water (turquoise symbols) mixtures at 1 bar. Filled symbols correspond to experimental data taken from the literature,[8] open symbols to MD NP_zAT simulations obtained in this work, and dashed curves to the fitting of the experimental interfacial tension values to parabolic curves.

simulations. In particular, we combined isothermal–isobaric or NP_zAT simulations, the direct coexistence simulation technique and the well-known molecular models for water (TIP4P/2005) and methyl esters (TraPPE-UA).

We firstly analyzed the density profiles of water and methyl ester molecules across the LL interface as a function of temperature for all methyl ester + water binary mixtures considered. The density profiles of water exhibit a monotonic behaviour when passing from one liquid phase to the other. In contrast, density profiles of methyl esters exhibit relative maxima, indicating an increasing preferential adsorption at the interface as the molecular weight of the organic compound increases. This phenomenon is less marked as the temperature is increased in all of the cases due to the thermal agitation. Contrary to what happens with other similar systems that exhibit LL immiscibility, as linear alcohol + water binary mixtures do not observe preferential orientation of methyl esters perpendicular to the interface. In fact, the molecules do not show the formation of monolayers or bilayers or organic molecules as in the case of alcohols in aqueous solutions. This is probably due to the inability of methyl esters to form hydrogen bonds with water molecules.

From the information of density profiles of water and methyl esters, we determine the temperature–density, $T\rho$, and temperature–composition, Tx, projections of the phase diagram at atmospheric pressure. MD simulations show, with the molecular parameters of pure components and without any further adjustment, that mixtures exhibit large regions of LL immiscibility in all cases. Particularly, molecular models are able to provide a very good description of both phase envelopes, except for the methyl acetate + water system. In this case, simulations predict a wider phase separation, in densities and compositions, compared with experimental data taken from the literature. In the rest of the mixtures, the simulations predict accurate values of coexistence densities and compositions for the mixtures in the whole range of temperatures considered.

Finally, we consider the LL interfacial tension of the mixtures at atmospheric pressure. In particular, we use the virial route to calculate the normal and tangential components of the pressure tensor. Molecular models are able to predict the characteristic parabolic shape of the interfacial tension as a function of temperature. They also capture the existence of a relative maximum value for each system at a temperature that increases as the molecular weight of the organic molecule is increased. Unfortunately, the experimental values of interfacial tension are substantially overestimated by our predictions in all cases. This is probably since unlike interactions between organic molecules and water are not accounted for properly. Although TIP4P/2005 and TraPPE models exhibit limitations for predicting in a quantitative manner the experimental data, they are able to capture an important number of issues characteristic of these complex binary mixtures.

Conflicts of interest

The authors declare that they have no known competing financial interests or personal relationships that could have appeared to influence the work reported in this paper.

Acknowledgements

This work was financed by the Spanish Ministerio de Economía, Industria y Competitividad (Grant No. FIS2017-89361-C3-1-P) and Junta de Andalucía (Grant No. P20-00363), both co-financed by EU FEDER funds, and Universidad de Huelva. We also acknowledge the Centro de Supercomputación de Galicia (CESGA, Santiago de Compostela, Spain) for providing access to computing facilities. AM acknowledges funding from Fondecyt (Chile) through Grant 1190107.

References

1 R. Luque, C. S. K. Lin, K. Wilson and J. Clark, *Handbook of Biofuels Production*, Woodhead Pub, 2nd edn, 2016.
2 P. P. Peralta-Yahya, F. Zhang, S. B. del Cardayre and J. D. Keasling, *Nature*, 2012, **488**, 320–328.
3 D. Bolonio, M.-J. García-Martínez, M. Ortega, M. Lapuerta, J. Rodríguez-Fernández and L. Canoira, *Renewable Energy*, 2019, **132**, 278–283.
4 R. M. Ceballos, *Bioethanol and Natural Resources: Substrates, Chemistry and Engineering Systems*, CRC Press, 2017.
5 N. D. D. Carareto, C. Y. C. S. Kimura, E. C. Oliveira, M. C. Costa and A. J. A. Meirelles, *Fuel*, 2012, **96**, 319–326.
6 T. J. Bruno, T. M. Loestead, J. R. Riggs, E. L. Jorgenson and M. L. Huber, *Energy Fuels*, 2011, **25**, 2493–2507.
7 A. T. Gros and R. O. Feuge, *J. Am. Oil Chem. Soc.*, 1952, **29**, 313–317.
8 I. del Pozo, M. Cartes, F. Llovell and A. Mejía, *J. Chem. Thermodyn.*, 2018, **121**, 121–128.
9 S. Enders and K. Quitzsch, *Langmuir*, 1998, **14**, 4606–4614.
10 H. Renon and J. M. Prausnitz, *AIChE J.*, 1968, **14**, 135–144.
11 A. Maczyński, B. Wiśniewska-Goclowska and A. Jezierski, *J. Phys. Chem. Ref. Data*, 2009, **38**, 1093–1127.
12 A. Mejía, Personal communication.
13 R. L. Scott and P. H. V. Konynenburg, *Discuss. Faraday Soc.*, 1970, **49**, 87–97.
14 P. H. V. Konynenburg and R. L. Scott, *Philos. Trans. R. Soc., A*, 1980, **A298**, 495–540.
15 E. Feria, J. Algaba, J. M. Míguez, A. Mejía, P. Gómez-Álvarez and F. J. Blas, *Phys. Chem. Chem. Phys.*, 2020, **22**, 4974–4983.
16 G. M. Martin and J. I. Siepmann, *J. Phys. Chem. B*, 2001, **102**, 2569–2577.
17 B. Chen, J. J. Potoff and J. I. Siepmann, *J. Phys. Chem. B*, 2001, **105**, 3093–3104.
18 G. Kamath, J. Robinson and J. J. Potoff, *Fluid Phase Equilib.*, 2006, **240**, 46–55.
19 J. J. Potoff and J. I. Siepmann, *AIChE J.*, 2001, **47**, 1676–1682.
20 G. Kamath, F. Cao and J. J. Potoff, *J. Phys. Chem. B*, 2004, **108**, 14130–14136.
21 J. Stubbs, J. J. Potoff and J. I. Siepmann, *J. Phys. Chem. B*, 2004, **108**, 17596–17605.
22 J. L. Abascal and C. Vega, *J. Chem. Phys.*, 2005, **123**, 1–12.
23 http://chem-siepmann.oit.umn.edu/siepmann/trappe/index.html, 2019.

24 H. J. C. Berendsen, J. R. Grigera and T. P. Straatsma, *J. Chem. Phys.*, 1987, **91**, 6269–6271.
25 W. L. Jorgensen, J. Chandrasekhar, J. Madura, R. W. Impey and M. Klein, *J. Chem. Phys.*, 1983, **79**, 926–935.
26 M. W. Mahoney and W. L. Jorgensen, *J. Chem. Phys.*, 2000, **112**, 8910–8922.
27 H. W. Horn, W. C. Swope, J. W. Pitera, J. D. Madura, T. J. Dick, G. L. Hura and T. Head-Gordon, *J. Chem. Phys.*, 2004, **120**, 9665–9678.
28 J. M. Míguez, D. González-Salgado, J. L. Legido and M. M. Piñeiro, *J. Chem. Phys.*, 2010, **132**, 1–5.
29 C. Vega and E. de Miguel, *J. Chem. Phys.*, 2007, **126**, 1–10.
30 C. Miqueu, J. M. Míguez, M. M. Piñeiro, T. Lafitte and B. Mendiboure, *J. Phys. Chem. B*, 2011, **115**, 9618–9625.
31 J. M. Garrido, H. Quinteros-Lama, J. M. Míguez, F. J. Blas and M. M. Piñeiro, *J. Phys. Chem. C*, 2019, **123**, 28123–28130.
32 J. M. Míguez, J. M. Garrido, F. J. Blas, H. Segura, A. Mejía and M. M. Piñeiro, *J. Phys. Chem. C*, 2014, **118**, 24504–24519.
33 J. Rayman, *PhD thesis*, University of Budapest, 1906.
34 A. Skrzecz, *Pol. J. Chem.*, 1980, **54**, 1101–1104.
35 R. Stephenson and J. Stuart, *J. Chem. Eng. Data*, 1986, **31**, 56–70.
36 D. van der Spoel, E. Lindahl, B. Hess, G. Groenhof, A. E. Mark and H. J. Berendsen, *J. Comput. Chem.*, 2005, **26**, 1701–1718.
37 M. A. Cuendet and W. F. V. Gunsteren, *J. Chem. Phys.*, 2007, **127**, 184102.
38 S. Nosé, *Mol. Phys.*, 1984, **52**, 255–268.
39 W. G. Hoover, *Phys. Rev. A: At., Mol., Opt. Phys.*, 1985, **31**, 1695–1697.
40 M. Parrinello and A. Rahman, *J. Appl. Phys.*, 1981, **52**, 7182–7190.
41 G. Galliero, M. M. Piñeiro, B. Mendiboure, C. Miqueu, T. Lafitte and D. Bessieres, *J. Chem. Phys.*, 2009, **130**, 104704.
42 G. Galliero, *J. Chem. Phys.*, 2010, **133**, 1–7.
43 J. M. Míguez, M. M. Piñeiro and F. J. Blas, *J. Chem. Phys.*, 2013, **138**, 1–11.
44 L.-J. Chen, *J. Chem. Phys.*, 1995, **103**, 10214–10216.
45 M. González-Melchor, P. Orea, J. López-Lemus, F. Bresme and J. Alejandre, *J. Chem. Phys.*, 2005, **122**, 094503.
46 J. Janeček, *J. Chem. Phys.*, 2009, **131**, 124513.
47 U. Essmann, L. Perera, M. L. Berkowitz, T. Darden, H. Lee and L. G. Pedersen, *J. Chem. Phys.*, 1995, **103**, 8577–8593.
48 H. J. C. Berendsen, J. P. M. Postma, W. F. V. Gunsteren, A. D. Nola and J. R. Haak, *J. Chem. Phys.*, 1984, **81**, 3684.
49 H. Hulshof, *Ann. Phys.*, 1901, **4**, 165–186.
50 E. A. Müller, A. Ervik and A. Mejía, *Living J. Comp. Mol. Sci.*, 2021, **2**, 21385.
51 T. Lafitte, B. Mendiboure, M. M. Piñeiro, D. Bessieres and C. Miqueu, *J. Phys. Chem. B*, 2010, **114**, 11110–11116.
52 J. Algaba, J. M. Míguez, P. Gómez-Álvarez, A. Mejía and F. J. Blas, *J. Phys. Chem. B*, 2020, **124**, 8388–8401.
53 J. Algaba, J. M. Garrido, J. M. Míguez, A. Mejía, A. I. M.-V. Bravo and F. J. Blas, *J. Phys. Chem. C*, 2018, **122**, 16142–16153.
54 J. Algaba, M. Cartes, A. Mejía, J. M. Míguez and F. J. Blas, *J. Phys. Chem. C*, 2019, **123**, 20960–20970.
55 A. Mejía, M. Cartes, G. Chaparro, E. Feria, F. J. Blas, J. M. Míguez, J. Algaba and E. A. Müller, *J. Mol. Liq.*, 2021, **431**, 116918.

